Structure development in semi-crystalline polymers under processing conditions : an experimental approach

Structure development in semi-crystalline polymers under processing conditions

An experimental approach

Structure development in semi-crystalline polymers under processing conditions:
An experimental approach

by Martin van Drongelen
Technische Universiteit Eindhoven, 2015

A catalogue record is available from the Eindhoven University of Technology Library
ISBN: 978-90-386-3867-6

This thesis was prepared with the LaTeX 2_ε documentation system
Printed by: Gildeprint
Cover design: STUT producties & Martin van Drongelen

This thesis is a result of the research programme of the Dutch Technology Foundation STW,
"Predicting catastrophic failure of semi-crystalline polymer products"

Structure development in semi-crystalline polymers under processing conditions

An experimental approach

PROEFSCHRIFT

ter verkrijging van de graad van doctor aan de Technische Universiteit Eindhoven, op gezag van de rector magnificus prof.dr.ir. F.P.T. Baaijens, voor een commissie aangewezen door het College voor Promoties, in het openbaar te verdedigen op 16 juni 2015 om 16:00 uur

door

Martin van Drongelen

geboren te Axel

Dit proefschrift is goedgekeurd door de promotoren en de samenstelling van de promotiecommissie is als volgt:

voorzitter:	prof.dr. L.P.H. de Goey
promotor:	prof.dr.ir. G.W.M. Peters
copromotor(en):	dr.ir. L.E. Govaert
leden:	prof.dr. C. Schick (Universität Rostock)
	prof.dr.ir. P.C.J. van Puyvelde (Katholieke Universiteit Leuven)
	prof.dr. A.P.H.J. Schenning
	prof.dr.ir. P.D. Anderson
adviseur(s):	dr. L. Balzano (DSM Ahead)

Contents

Summary

Polymer materials are well known for their ease of processability and relatively good properties at low costs. A large part of the polymers used are semi-crystalline, such as polyethylene (PE), polypropylene (PP) and polyamide (PA), consisting of amorphous (random) and crystalline (ordered) micro-sized regions. The number, size, type, and orientation of the latter strongly depend on the conditions during the product shaping step, going from the melt to the solid state, and, to a large part, control the mechanical and optical properties of the final product. Therefore, it is of great importance to quantify the intricate coupling between the processing conditions and resulting microstructure. Ultimately, a production process could be altered in such way that the desired set of final properties is obtained.
The work presented in this thesis aims at measuring, understanding, modelling and predicting the influence of realistic processing conditions on the crystallization behaviour of a variety of polyolefin resins and polyamide-6. For this purpose, a number of advanced experimental techniques were employed to study the effects of high cooling rates, pressure, and shear on the development of crystalline structures. In some cases, even unique combinations of these techniques were realized for this work.

Fast scanning calorimetry (FSC) is a recently developed technique typically used for calorimetric analysis of crystallization, melting and reorganization of polymers under high cooling and heating rates. A feasibility test is presented in which, for the first time, microfocus wide-angle X-ray diffraction (WAXD) has been employed for characterization of the crystalline phase structure of samples prepared in the FSC.

Linear low-density polyethylene (LLDPE) is often used for film blowing applications. Due to its molecular architecture, crystallization during cooling is a multi-process event, consisting of one primary process, i.e. growth of spherulites, followed by a two-stage secondary process. This process consists of lamellar insertion followed by bundle-like ordering of a fraction of the remaining amorphous part at low temperatures. A full characterization of the crystallization kinetics of a metallocene LLDPE is presented. Primary crystallization is described using kinetics for nucleation and growth of spherulites obtained with small-angle light scattering (SALS). The secondary process was described and coupled to primary crystallization using a convolution integral approach, of which the parameters were determined from DSC and FSC experiments using a wide range of cooling rates (0.07-2000 °C/s).

Dilatometry experiments reveal the influence of flow and pressure on both primary- and secondary crystallization. Surprisingly, primary crystallization is enhanced by flow, while secondary crystallization is suppressed. Finally, a molecular stretch based model is applied that successfully can capture flow-enhanced point-like nucleation and the formation of oriented structures, respectively.

Heterogeneous polypropylene impact copolymers consist of a crystalline matrix material with a dispersed amorphous phase. They are increasingly used in the automotive industry because of their specific property profile, which balances stiffness and impact properties. Process-structure-property relations are studied for three different compounds. Samples were processed at different cooling rates with various amount of flow in a well-controlled environment. It is shown that with flow, three regimes can be observed. As a function of flow strength, first no orientation is observed, followed by flow-induced crystallization and orientation of the matrix material and, finally, flow-induced crystallization and orientation of matrix and filler material. Each regime is clearly represented in morphology, crystallization kinetics and mechanical properties.

Blown film extrusion is combined with in-situ WAXD at a synchrotron radiation beam-line. Both the evolution of crystallinity and crystal orientation are studied for three different low-density polyethylene (LDPE) grades, for a combination of high and low levels of take-up and blow-up ratios and as function of the distance and time from the die. For a material with a moderate molecular weight in combination with relatively low content of (ultra-) high molecular weight chains, relatively high rates of crystallization are observed, while a high molecular weight material, as expected, leads to the highest overall orientation level. Due to the complexity of the film blowing process, no clear relation between material properties and orientation of the crystallographic axes could be found. Independent of both the material and processing conditions studied, the frost-line is observed at about 20% crystallinity. At the frost-line also the final average orientation of the crystallographic c-axis is reached. It is shown that this technique is a valuable method to study structure evolution in the complex process of film blowing. This method provides data which can be used to validate results from numerical models and improve and/or extend these models.

Nascent polyamide-6 (PA-6) shows a peculiar and irreversible effect; the quiescent crystallization kinetics upon cooling are accelerated upon deformation in the melt, even after full relaxation of the melt. This phenomenon, known as the 'memory effect' of polyamide materials, is explored in a step-by-step manner using WAXD. For this purpose, unique samples were used, which were created by compression moulding the granular material just below the average melting temperature. The experimental data shows that only the imposed strain level influences the irreversible change in the quiescent crystallization kinetics. During heating and cooling of the undeformed melt, an unknown crystallization behavior is observed. Finally, possible causes for the memory-effect are discussed and related to hypotheses from the literature.

Chapter 1

Introduction

Polymeric materials exhibit a sophisticated process-properties relationship that links the final properties of a product to the history of the material during processing. A full understanding of this mechanism is a prerequisite to tailor the ultimate properties of plastic products. This thesis studies part of this, and focuses on the influence of processing on structure development and implementing the results in predictive models.

1.1 Background

Taking a glance around at the readers current location, chances are close to certainty that many objects in his or her environment are made of polymers. Polymer materials have integrated in everyday life products because of their relatively good properties, ease of processability and low costs, and have been around us already for quite some time. In fact, they have been in nature from the beginning. Natural polymers such as cellulose (found in wood, cotton), starch (found in potatoes, corn) or even DNA, are omnipresent.

The birth of the plastic industry can be traced back to the first man-made (semi-synthetic) polymer, *Parkesine*, which was invented around 1856 and mostly used in movie and photography industries [1]. Unfortunately, the material was highly flammable, difficult to produce and very expensive. In time, applicable (fully synthetic) polymers were invented such as bakelite (1900's), polyamide (1920's), and polyethylene (1930's), although they were still used in relatively small amounts. Matters changed when the world went to war in the 1940's, when access to specific natural resources became limited. Consequently, these materials were replaced by plastics (polymers with additives) and both the development and production of synthetic polymers took flight. Since then, the volume of plastics produced exceeded that of steel from the 1980's onwards, and was estimated at 299 millions tonnes in 2013 [2]. Unfortunately, no direct correlation exists between the huge amounts of plastic that is produced by mankind, and the efficiency at which it is being used.

In the case of semi-crystalline polymers, i.e. those that are composed of the relatively 'flexible' macromolecular family, the mechanical performance of thermoplastic products is mostly dictated by the structure developed during the crystallization process, which takes place throughout solidification from the melt. Crystallization of synthetic polymers has been extensively studied in recent decades, e.g. [3–7], providing a basic understanding of the rules and kinetics under ideal circumstances.
When the material is cooled from the melt without any disturbance, i.e. in quiescent conditions, nucleation sites appear below the melting temperature. From these nuclei, crystal lamellae grow radially outward by chain folding of the molecules, and self-assemble in to curious spherical entities called spherulites of roughly 10-1000 μm in diameter, see Figure 1.1a. However, if the polymer is subjected to flow, such as during processing, the crystallization behaviour is rather different. For mild flow conditions, the number of nuclei increases and, for strong enough flow, oriented 'shish-kebab' crystallites are formed consisting of a fibrillar core (shish) overgrown by a stack of lamellae (kebabs), Figure 1.1b.

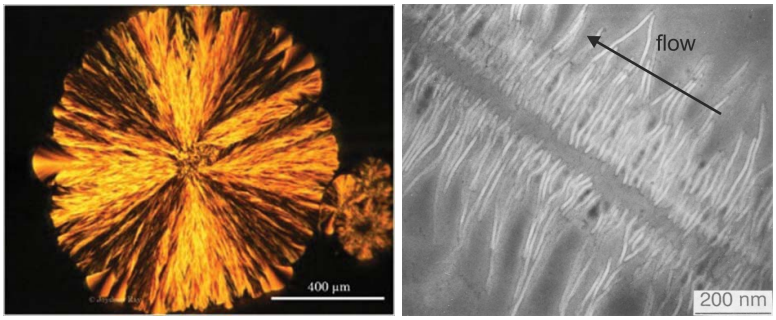

(a) (b)

Figure 1.1: (a) Not only polymers can grow spherulites, as can be seen from the large spherulite composed of fat crystals in chocolate, taken from [8]. (b) An example of oriented shish-kebab in polyethylene, taken from [9].

The majority of polymer components is produced using established techniques such as injection moulding, extrusion or film blowing. All of these involve a first step at which molten material is forced through (geometrically complex) dies and, finally, a cooling step to fix the shape desired. To achieve maximum productivity (and minimum costs) processes are conducted at high speeds and involve steep thermal gradients, high pressures and immense flow rates. For semi-crystalline polymers, these conditions have a dramatic influence on the crystal size, number, shape and orientation. Due to (local) molecular deformation and chain orientation along the flow direction, complex skin-core morphologies are formed in which highly oriented and isotropic structures form simultaneously, Figure 1.2. The properties of the final product, e.g. long-term properties, impact behaviour or transparency, are strongly dependent on these differences of the crystalline microstructure and, therefore, understanding and controlling this structure is of utmost importance.

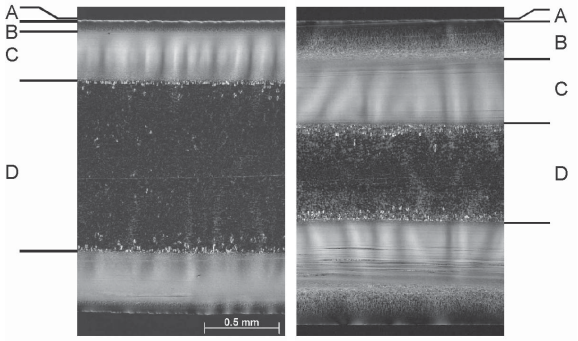

(a) (b)

Figure 1.2: Optical micrographs of cross-sections of polypropylene samples, injection moulded at (a) 40 mm/s for 2 s and (b) 5 mm/s for 16 s. Distinguished layers are: (A) skin layer, (B) transition layer, (C) shear layer, and (D) isotropic core. Pictures taken from [10].

1.2 Characterization tools

Specific features of the crystal micro-structure such as crystallinity level, phase, lamellar thickness, and orientation, should be taken into account. During the years, many characterization techniques were developed, each able to obtain morphological details at a certain length scale and resolution or to quantify specific physical properties. Techniques used include differential scanning calorimetry (DSC), dilatometry and various rheometry setups. Here, the occurrence of crystallization can be distinguished directly from characteristics in the heat flow (DSC), specific volume change (dilatometry) or torque signal (rheometry), respectively. Other devices, such as commercial hot stages or shear cells need to be combined with an extra measuring technique to follow any structure development in the material, for which polarized optical microscopy (POM), small-angle light scattering (SALS), or X-ray scattering are mostly recommended.

Despite the major scientific significance of the aforementioned, most are limited to experimental protocols far from those relevant for industry. Ongoing development of available tools and/or new devices has provided new opportunities on understanding unsolved aspects within polymer crystallization. Advanced calorimetric techniques (FSC) [11], extended dilatometry (Pirouette) [12], and an upgraded experimental infrastructure at synchrotron facilities to allow for simultaneous X-ray acquisition at high frequencies [13], to name a few.

1.3 Scope and Outline

This thesis aims at measuring, understanding and predicting the effect of processing conditions, relevant for industrial applications, on the crystallization process of different polyolefin resins and polyamide-6. For this purpose, use was made of state-of-the-art experimental techniques, or even unique combinations of these techniques realized especially for the work reported here.

Chapter 2 reports on the crystalline microstructure of samples solidified at high undercooling on a fast scanning calorimeter (FSC) sensor, which was validated, for the first time, using microfocus wide-angle X-ray diffraction (WAXD). Next, in **Chapter 3**, a full characterization of the crystallization kinetics of a metallocene linear low-density polyethylene (LLDPE) grade is presented. Both the influence of high cooling rates (using a combination of FSC/DSC and SALS) and high shear rates (using extended dilatometry) were captured. In **Chapter 4**, process-structure-property relations are studied for three different compounds of a heterogeneous high-impact PP copolymer. Samples were processed at different cooling rates with various amount of flow in a well-controlled environment. In **Chapter 5**, structure development, i.e. crystallinity and orientation, is studied during film blowing for three different low-density polyethylene (LDPE) grades, at a combination of high and low levels of take-up and blow-up ratios, as function of the distance from the die. For this, blown film extrusion is combined with in-situ WAXD at a synchrotron radiation beam-line. **Chapter 6** reports on the deformation induced shift of the crystallization rate of nascent PA-6. This phenomenon, known as the 'memory effect' of polyamide materials, is explored in a step-by-step manner using calorimetry and WAXD. Finally, the main conclusions of the work are reiterated in **Chapter 7** and recommendations for future work are given.

Chapter 2

Microfocus wide-angle X-ray scattering of polymers crystallized in a fast scanning chip calorimeter

Reproduced from: Martin van Drongelen, Tamara Meijer-Vissers, Dario Cavallo, Giuseppe Portale, Geert Vanden Poel and René Androsch, *Thermochimica Acta*, 563:33-37, 2013

Abstract

Microfocus wide-angle X-ray diffraction (WAXD) has been applied to analyze the polymorphism of isotactic polypropylene and polyamide-6 prepared in a fast scanning chip calorimeter (FSC). Samples with a typical mass of few hundred nanograms, and lateral dimension and thickness of about 100 μm and 20 μm, respectively, were exposed to a defined thermal history in the FSC and subsequently analyzed regarding the X-ray structure at ambient temperature using an intense synchrotron microfocused X-ray beam.
The relaxed melt of isotactic polypropylene was cooled at rates of 40 °C/s and 200 °C/s which allowed formation of α-crystals or mesophase, respectively. Polyamide-6 was isothermally crystallized at 95 °C and 180 °C which led to formation of β-mesophase and α-crystals, respectively. This study demonstrated, for the first time, that FSC polymer crystallization experiments could be completed and expanded by subsequent in-situ structure analysis by X-ray scattering.

2.1 Introduction

A number of fast scanning calorimetry techniques has been developed in the recent years for analysis of crystallization, melting and reorganization of polymers. The first breaktrough was the HPer DSC, which was based on existing differential scanning calorimetry (DSC), but instead could reach cooling or heating rates up to 750 °C/min [14]. Later, non-commercial equipment was developed to reach scanning rates up to 2000 °C/min [15]. Fast scanning chip calorimetry (FSC) has been introduced about a decade ago by Schick and co-workers [16, 17], and is nowadays considered as a well-established experimental tool for polymer characterization. It allows quantitative calorimetric analysis of phase transitions at rates of cooling and heating up to 10^6 °C/s [18], depending on the specific sensor and setup used, and the time-resolution in isothermal experiments is of the order of magnitude of milliseconds. In 2010, the first commercial available FSC device was brought to the market [19–22]. The use of FSC allows bypassing crystallization at low supercooling and enables analysis of structure formation at high supercooling. Increasing supercooling of the melt leads to an increase of the nucleation density or even change of the nucleation mechanism [23–25], ultimately affecting the morphology and superstructure of the ordered domains/crystals which develop, and the final materials properties [26–28]. In addition, and more important in the context of the present work, variation of the supercooling of the melt may lead to formation of different polymorphs, as is out-lined below on the examples of isotactic polypropylene (iPP) [29], and polyamide-6 (PA-6) [30].

Information about the crystal structure and the polymorphism of crystallizable polymers requires the use of wide-angle X-ray diffraction (WAXD). As far as we are aware, no successful attempts have been made to analyze the X-ray structure of polymer samples prepared in an FSC. It is the intention of the present study to demonstrate the advantageous combination of FSC which enables exact control of the nucleation and crystallization pathways and detection of enthalpies and temperatures of transitions, and WAXD for subsequent analysis of the resulting phase structure. Earlier WAXD analyses of the supercooling triggered polymorphism of polymers were performed on samples prepared in special rapid-cooling devices [31–36], with disadvantages of non-linear cooling, limited maximum cooling rate, decreasing cooling rate on approaching the target temperature, or, more important, impossibility of simultaneous measurement of enthalpies of transitions. With the introduction of FSC, these disadvantages on sample preparation are removed; however, since FSC requires the use of specimens of extremely low mass and size, WAXD analysis is not straightforward and requires sophisticated instrumentation, as described and tested in this work.

Furthermore, due to the high surface-to-volume ratio of FSC samples, crystallization may be affected by nucleation of the ordering process at the free surfaces of the sample, or at the sample-membrane interface, but not in the bulk. Comparison of X-ray data obtained on FSC samples and on macroscopic samples of lower surface-to-volume ratio

may provide information whether the large specific surface area of FSC samples influences the crystallization process. In the present X-ray study of the supercooling-controlled polymorphism of polymers, samples of iPP and PA-6 prepared in an FSC were employed. These polymers were investigated in detail in the past regarding the effect of cooling rate/supercooling on the kinetics of structure formation and on the polymorphism. Films with a thickness of about 100 μm were cooled at different rates in home-made rapid-cooling devices, with the evolution of the WAXD structure followed in real time during cooling using synchrotron radiation [34–36], or ex-situ after completion of the cooling experiment [27,31–33]. In case of iPP it was found that cooling at rates less than about 100 °C/s permits formation of monoclinic α-crystals while faster cooling to ambient temperature leads to mesophase formation. Similarly, cooling PA-6 at a rate lower than about 10 °C/s allowed development of α-crystals, while faster cooling to room temperature caused formation of β-mesophase or even full vitrification of the melt. The X-ray studies have been completed by in-depth FSC analysis of the kinetics of crystallization and mesophase formation [37–39], and analysis of the morphology and superstructure of crystals and mesophase [27, 40, 41]. This notwithstanding, it needs to be emphasized that interpretation of a stand-alone FSC heat-flow rate signal requires complementary knowledge of the phase structure. Most straightforward is the direct WAXD analysis of the FSC sample, after the imposition of a certain thermal history.

2.2 Materials and Methods

2.2.1 Materials

We used an isotactic polypropylene PP 531P homopolymer from Sabic (the Netherlands), with a mass-average molar mass and polydispersity of 631 kg/mol and 5.3, respectively, for microfocus WAXD analysis of the structure after cooling at rates of 40 °C/s and 200 °C/s. From prior analyses it is expected that cooling at 40 °C/s leads to α-phase crystallization while cooling at 200 °C/s causes mesophase formation [31, 35, 37]. Furthermore, we employed a polyamide-6 Akulon material from DSM (the Netherlands) with a mass-average molar mass of 33 kg/mol and a polydispersity of 2. The PA-6 sample was isothermally melt-crystallized at temperatures of 180 °C and 95 °C, with the intention to allow formation of α-crystals and β-mesophase, as reported in the literature [42].

2.2.2 Methods

Microfocus WAXD

Microfocus wide-angle X-ray diffraction experiments at ambient temperature on samples placed on an FSC sensor have been performed at the BM26B (DUBBLE) beamline at ESRF in Grenoble (France) [13]. The synchrotron beam was focused at the sample position by a post-focusing Kirkpatrick-Baez system consisting of two orthogonal coated silicon substrates bent into elliptical shapes. The horizontal and vertical beam dimensions at the sample were adjusted to 20 μm and 15 μm, respectively, in order to achieve maximum signal to noise ratio. The wavelength of the X-rays was 1.033 Å, and the sample to detector distance was 252 mm. We used a 2D Frelon CCD detector with an active area composed by 1024 x 1024 pixels and a pixel size of 94 μm x 94 μm. The accumulation time was 60 s for all samples. The X-ray images were corrected for dark current and background scattering. Calibration of the angular range has been achieved by using standard alpha Al_2O_3 and HDPE samples. The background was provided by an image taken in the center of the empty/unloaded reference calorimeter of the FSC sensor used. The FSC sensors were carefully aligned perpendicularly with respect to the micro X-ray beam using high precision motorized stages. After pre-alignment of the FSC sensors using a high magnification optical camera, the small samples were aligned with respect to the X-ray beam using a high resolution horizontal and vertical grid scan while monitoring the scattered intensity at the detector.

Fast scanning chip calorimetry

FSC measurements were performed using a twin-type power-compensation Mettler-Toledo fast scanning chip calorimeter Flash DSC 1 equipped with a Huber TC100 intracooler. It consists of two separated silicon nitride/oxide membranes with an area of 1.7 mm x 1.7 mm and a thickness of 2.1 μm each, serving as sample and reference calorimeters. The membranes are surrounded by a silicon frame of 300 μm thickness and a ceramic support. The circular measurement area with a diameter of 500 μm in the center of each membrane is coated with 0.5 μm aluminum and contains heaters and temperature sensors. Figure 2.1 shows the samples of PA-6 (left) and iPP (right) investigated in the present work, as placed on the heatable area of the sample calorimeter. The thickness of the samples is about 20 μm and the lateral dimension is 100-200 μm. Subsequent the crystallization experiment in the Flash DSC 1, the sensor was removed from the main instrument and placed into an x-y sample stage such that the incident X-ray beam is oriented perpendicular to the membrane surface, passing through the sample. Further details about the particular FSC used, including schematics of the sensor, performance, calibration, and sample preparation are provided elsewhere [19–22]. In the present study, the FSC sensor was conditioned and temperature-corrected according to the specification of the instrument provider.

Worthwhile noting, though systematic investigations have not been performed yet, that repeated exposure of the FSC sensor to intense X-ray radiation led to a loss of its functionality.

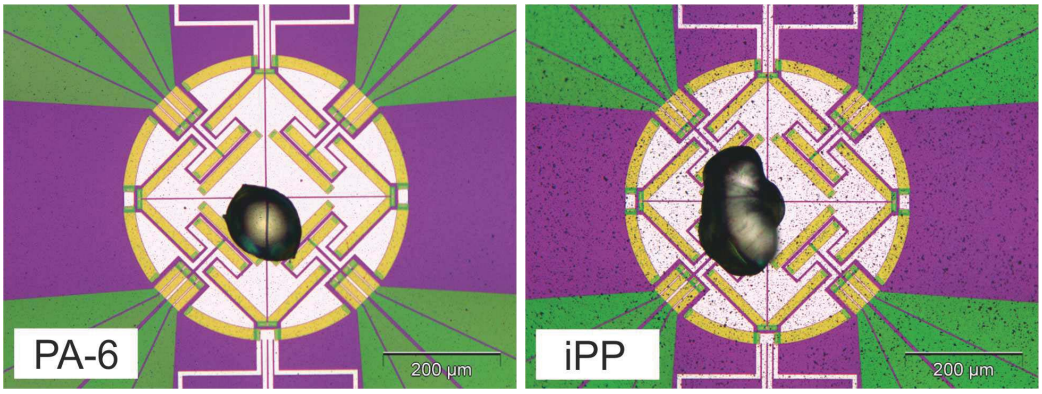

(a) (b)

Figure 2.1: Optical microscopy pictures of samples of PA-6 (a) and iPP (b) placed on the heatable area of the sample calorimeter of the UFS 1 sensor of the power-compensation Mettler-Toledo Flash DSC 1. These samples were exposed to a specific crystallization-history and subsequently analyzed by microfocus WAXD. The diameter of the circular area of the calorimeter is 500 µm.

2.3 Results

Figure 2.2 shows apparent heat capacity data of iPP as a function of temperature, calculated from heat-flow-rate data recorded on cooling the relaxed melt at different rate between 20 °C/s (topcurve) and 500 °C/s (bottom curve). The data of Fig. 2 show two separate ordering processes at different temperatures. The high-temperature peak (C) is due to crystallization/formation of monoclinic crystals (α-crystal phase) and the low-temperature peak (M) is due to mesophase formation. Cooling the quiescent melt at rates lower than 50 °C/s leads to formation of the α-phase only, while solidification at rates between 60 °C/s and 200 °C/s additionally allows mesophase formation at lower temperature. If the cooling rate exceeds 200 °C/s then formation of monoclinic α-crystals cannot be observed anymore, and presence of the low-temperature peak suggests exclusive formation of the mesophase. Cooling faster than 300-500 °C/s leads to complete vitrification of the super-cooled melt at the glass transition temperature. It is important to note that the assignment of the various exothermic peaks to formation of different polymorphs is based on WAXD analyses of samples prepared separately. Only in this work, we analyzed for the first time the X-ray structure of samples prepared in a FSC directly. The sample shown at the right-hand side of Fig. 1 was cooled at rates of 40 °C/s or 200 °C/s to ambient temperature, and then the FSC sensor including the sample was positioned into the synchrotron X-ray beam.

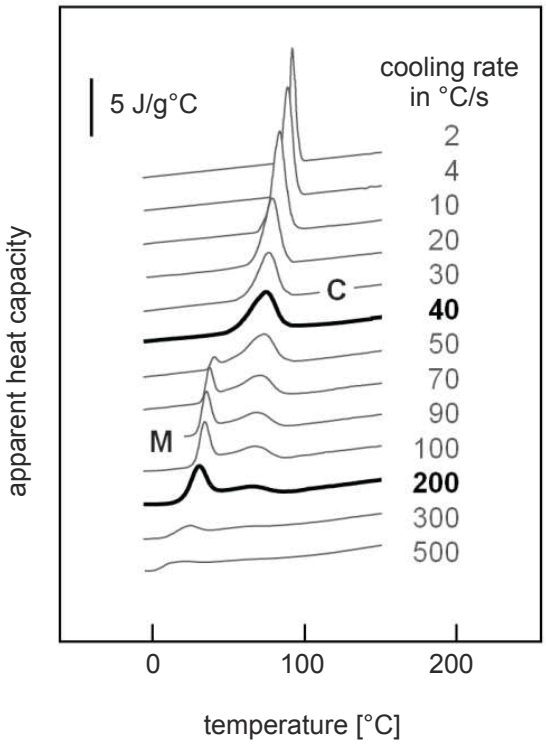

Figure 2.2: Apparent specific heat capacity of iPP as a function of temperature, recorded on cooling the relaxed melt at different rate. The cooling rate is indicated at the right-hand side of each curve. Microfocus WAXD analysis has been performed on samples cooled at 40 and 200 °C/s, with the corresponding cooling curves drawn in bold. Reprinted/adapted from [43].

Figure 2.3 shows rectangular sections of the 2D microfocus WAXD patterns of iPP cooled at 40 °C/s (top) and 200 °C/s (bottom) in the FSC, superimposed by the azimuthally integrated scattering intensity. The X-ray pattern of the sample cooled at a rate of 40 °C/s shows the (110), (040), (130), and (111+13m1+041) scattering peaks, corresponding to interplanar spacings of 6.3, 5.3, 4.8, and 4.1 Å of the monoclinic α-phase, respectively [44]. The WAXD pattern of iPP cooled at a rate of 200 °C/s, in contrast, does not show sharp diffraction peaks rather than two halos corresponding to distances of about 5.9 Å and 4.1 Å, respectively. These are characteristic of the mesophase and represent the distance between neighbored chains and the intramolecular helix repeat, respectively [45].

A further case study is the microfocus WAXD analysis of the polymorphism of PA-6. The isotropic melt of PA-6 was cooled in the FSC to different temperatures and then isothermally crystallized while recording the heat-flow rate to gain information about the kinetics of the phase transition. In Figure 2.4 half-times of the crystallization as a function of the crystallization temperature between 60 °C and 190 °C are shown. With increasing supercooling of the melt the half-time of crystallization decreases due to increasing thermodynamic driving force of the phase transition, passes a minimum and increases at high supercooling due to increasing viscosity of the melt/decreasing segmental mobility [23].

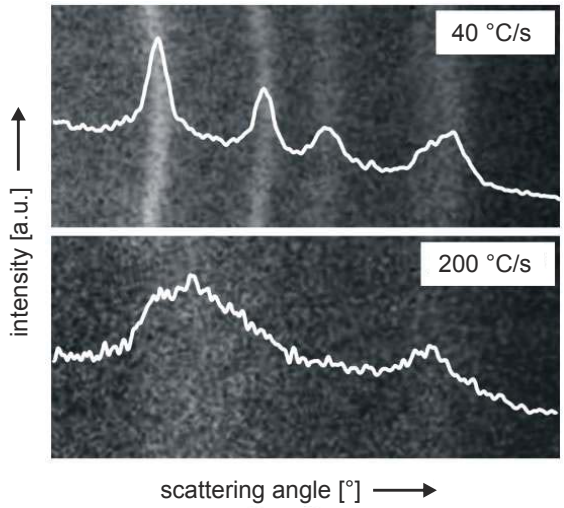

Figure 2.3: Rectangular sections of 2D microfocus WAXD patterns obtained on a sample of iPP cooled at 40 °C/s (top) and 200 °C/s (bottom) in the Flash DSC 1, superimposed by the azimuthally integrated scattering intensity.

Note that the half-time of crystallization is reciprocal to the crystallization rate. As such, the maximum crystallization rate of the particular PA-6 studied is observed at about 140 °C, which is in accord with recently performed FSC studies of the kinetics of crystallization of PA-6 [39, 46]. Albeit not in foreground in the present work, we observed a discontinuity of the dependence of the half-time of crystallization on temperature at around 100 °C, which likely is caused by the transition of mostly α-growth to dominating growth of the β-mesophase.

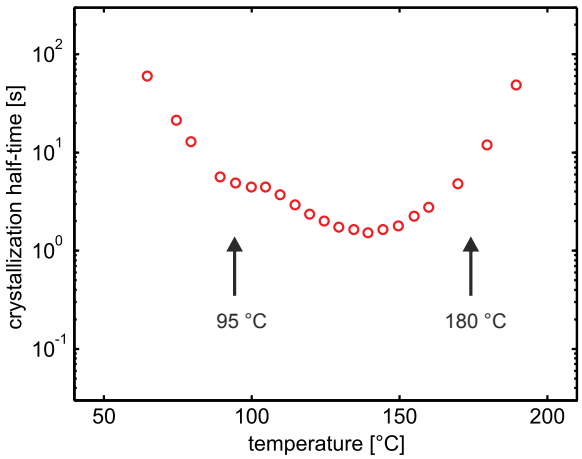

Figure 2.4: Half-time of isothermal crystallization of PA-6 as a function of temperature. Microfocus WAXD patterns have been collected on samples isothermally crystallized at 180 °C and 95 °C.

From the literature it is known that melt-crystallization of PA-6 at temperatures higher than 130-140 °C leads to formation of monoclinic α-crystals, while solidification of the supercooled melt at lower temperatures is connected with formation of a pseudo-hexagonal

β-mesophase [42, 47]. In order to demonstrate the capability of microfocus WAXD analysis of the phase structure of samples of extremely low mass of a few hundred nanograms only, we crystallized PA-6 at temperatures of 180 °C and 95 °C in the FSC and subsequently monitored the WAXD structure. Figure 2.5 shows the WAXD patterns of samples of PA-6 isothermally crystallized at 180 °C (top) or 95 °C (bottom) in the Flash DSC 1. The X-ray pattern of the sample crystallized at 180 °C shows peaks due scattering from the (200) and (002)/(202) lattice planes of the monoclinic α-phase of PA-6 with interplanar distances of about 4.2 Å and 3.6 Å, respectively [48, 49]. In short, the α-structure contains fully extended repeating units and is characterized by sheet-like hydrogen bonding [50]. It is considered as thermodynamically most stable crystal form which predominantly forms on melt-crystallization at temperatures higher than about 140 °C. In contrast, it has been found that a lower crystallization temperature, the monoclinic α-form is replaced by a pseudo-hexagonal mesomorphic β-structure. The β-form has been described as an aggregate of parallel and straight but conformationally disordered chain segments with cylindrical symmetry [47]. Hydrogen bonding within these small domains is almost complete, however, is not restricted to a specific crystallographic direction as in the α-form. Correspondingly, the X-ray pattern of the β-mesophase of PA-6 contains a strong peak, related to the lateral packing of chains with cylindrical symmetry. The WAXD pattern obtained on PA-6 isothermally ordered at 95 °C, displayed in Fig. 2.5, shows a single peak at a scattering angle of 14.9°, superimposed to the amorphous halo. The Bragg distance of the observed peak is about 4.0 Å which corresponds the average interchain distance in the β-mesophase of PA-6. As such, the microfocus WAXD patterns of samples of PA-6 crystallized at 180 °C

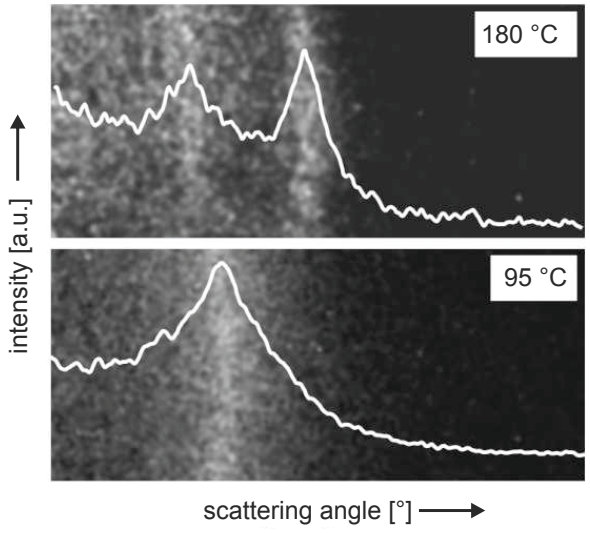

Figure 2.5: Rectangular sections of 2D microfocus WAXD patterns obtained on samples of PA-6 isothermally crystallized at 180 °C (top) or 95 °C (bottom) in the Flash DSC1, superimposed by the azimuthally integrated scattering intensity.

and 95 °C in the FSC are in agreement with the knowledge about the polymorphism of PA-6 available by prior X-ray studies using macroscopic samples.

2.4 Summary

In this work, for the first time microfocus wide-angle X-ray diffraction (WAXD) using synchrotron radiation has been employed for characterization of the phase structure of crystallisable polymers prepared in a fast scanning chip calorimeter (FSC). FSC permits calorimetric analysis of crystallization in a wide range of cooling rates and melt-supercooling, far beyond the limits of classical standard differential scanning calorimetry (DSC). In order to investigate polymer crystallization by FSC at extreme conditions, that is, fast cooling and high supercooling, the sample mass needs to be of the order of magnitude of few hundred nanograms only. Such small samples cannot be analyzed subsequent the FSC crystallization experiment regarding their phase structure using standard WAXD instrumentation. Analysis of the X-ray structure, however, is indispensably required for correct interpretation of changes of latent heat detected by FSC since different polymorphs may form as a function of supercooling. Since FSC offers the opportunity to realize sophisticated pathways of nucleation and crystallization, in order to gain further knowledge about polymer crystallization, WAXD analysis of FSC samples is an urgent task. We used intense synchrotron radiation, a microfocus X-raybeam with vertical and horizontal dimensions of 15 μm and 20 μm, respectively, and a 2D detector in order to compensate the low scattering volume of the FSC samples analyzed. For this first analysis, which must be considered as a screening/feasibility test, beforehand well-characterized samples were employed. Isotactic polypropylene (iPP) and polyamide-6 (PA-6), both are known to form crystals and mesophase at low and high supercooling of the melt, respectively. The formation of the different polymorphs by variation the cooling rate in case of iPP, or by isothermal crystallization temperature in case of PA-6, was successfully evidenced using the microfocus WAXD setup available at the BM26B beamline at the ESRF. We expect that the successful microfocus WAXD experiment on miniature FSC samples offers new chances/opportunities for analysis of crystallization of polymers. FSC allows precise investigation of temperatures and enthalpies of phase transitions as a function of the route of nucleation and crystallization, and subsequently performed WAXD analysis permits unambiguous assignment of thermal transitions to formation of specific phases.

Chapter 3

Characterization of the primary and secondary crystallization kinetics of a linear low-density polyethylene in quiescent- and flow conditions

Reproduced from: Martin van Drongelen, Peter Roozemond, Enrico Troisi, Antonios Doufas and Gerrit Peters, *submitted*

Abstract

The primary and secondary crystallization kinetics of a homogeneous linear low-density polyethylene were characterized as function of cooling rate, pressure and flow strength. Our approach to describe primary crystallization is based on temperature dependent nucleation and growth of spherulites governed by an Avrami-type equation for space filling. The growth rate and nucleation density were measured well below the melting temperature using small-angle light scattering in a fast cooling device. Heat balance calculations were employed to obtain and correct for the actual sample temperature during solidification. The description of the two-step secondary crystallization processes, i.e. insertion of lamellar stacks and the bundle-like ordering process, is coupled to primary crystallization using a convolution integral, for which the parameters were determined from (fast-) differential scanning calorimetry. To characterize the influence of flow, extended-dilatometry was used to investigate the effect of different thermomechanical histories on crystallization. The amount of molecular stretch was calculated for these flow conditions with the XPP model. Consequently, parameters could be determined for an existing model that couples molecular stretch to both nucleation rate and fibrillar growth rate. Excellent agreement is shown between calculated and experimentally obtained crystallization kinetics in conditions representative for those found in real-life processing, i.e. cooling rates up to 2000 °C/s (no flow), shear rates up to 180 1/s and a maximum pressure of 500 bar. This opens, for the first time, the possibility to calculate in detail the evolution of and the final crystallinity structure in products such as blown film or extruded tape.

3.1 Introduction

The use of ethylene and α-olefin copolymers has become widespread via the industrial implementation of metallocene type catalysts and the materials broad application in packaging industry. Also known as linear low-density polyethylene (LLDPE), the material is a substantially linear polymer with a large number of short branches, providing distinct rheological and mechanical properties, such as a relatively low shear sensitivity and a high tensile- and impact strength [51]. In order to understand the crystalline morphology of the final product as function of the shaping process, many researchers report on the crystallizability and processing-structure relation for various LLDPE resins, and focus specifically on the significant influence of the molecular branching- type, content, and distribution [52–56]. As the shaping process of polymeric products involves steep thermal gradients, high flow rates and pressure variations, studying the processing-structure relation in industrially relevant conditions requires well defined experiments in which these variables can be controlled. As a result of the rapid crystallization process of the ethylene based polymer, the temperature window for isothermal studies is often limited to low levels of undercooling. An additional complexity with branched (semi-crystalline) polymers is found in the high levels of secondary crystallization, sometimes up to 50% of the final crystallinity, due to a continuous insertion or thickening of lamellar features inside the spherultic geometries [57]. Many different experimental techniques were used to study crystallization from the LLDPE melt, often providing a measurement signal in which the different processes cannot be separated (easily). Therefore, most researchers prefer combined techniques of, for example, small angle light scattering (SALS), differential scanning calorimetry (DSC), and/or simultaneous small- and wide-angle X-ray scattering/diffraction (SAXS/WAXD) to obtain detailed time resolved structural information [55, 58–60]. Reports on the effects of flow on crystallization of LLDPE are limited and mostly performed using shear cell devices [56, 61], whereas the combined effect of pressure and flow has been studied mainly to obtain melt properties using rheometry [62, 63].

In some studies, the experimentally obtained non-isothermal (quiescent) crystallization kinetics are used as validation or input for predictive structure calculations, often using kinetic models [64–66] or physical models describing primary crystallization [67–69]. In the case of LLDPE however, the most promising approach is found in extended Avrami models to account for secondary crystallization effects [70–72]. The latter suits the implementation of nucleation and growth functions to describe primary crystallization. Hence, such a model requires accurate determination of both, the spherulitic growth rate and nucleation density in a wide range of temperatures in order to correctly describe space filling of spherulites in time. In this work, we adopted an Avrami-type model for space filling based on nucleation and growth, combined with a convolution integral to accurately describe the evolution of primary and a two step secondary crystallization during quiescent non-isothermal solidification in a large range of cooling rates. To obtain parameter values, we use a combination of SALS,

DSC and fast scanning chip colorimetry (FSC) techniques. Secondly, flow induced (primary) crystallization is described for different thermomechanical histories at multiple pressures with an approach based on rheology and dilatometry, similar to earlier work performed in our group [73]. Finally, dilatometry was used to characterize the effect of flow and pressure on secondary crystallization by converting the dilation measurement in a signal similar to those measured with DSC.

3.2 Material and Methods

3.2.1 Material

The material investigated is a metallocene LLDPE (ExxonMobil). It has an average butyl branch content of 1.2 mol%, a weight average molecular weight, M_w, of 94 kg/mol and a number average molecular weight, M_n of 24 kg/mol. The interchain branching distribution is relatively narrow, as indicated by temperature rising elution fractionation (TREF) data presented in Figure 3.1 and molar mass fractionation of the same material reported elsewhere [74].

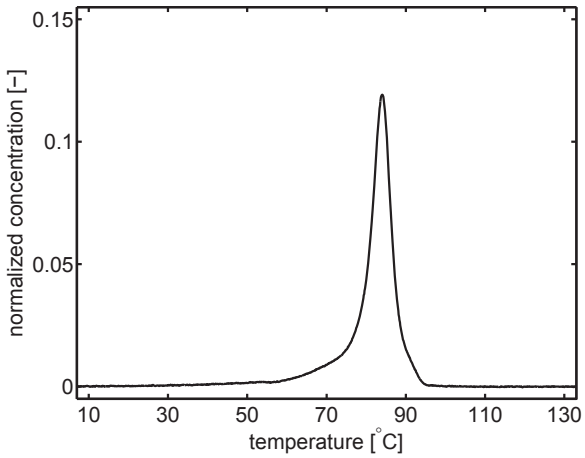

Figure 3.1: Normalized concentration vs. temperature during TREF of the LLDPE investigated. The elution temperature directly relates to co-monomer content.

3.2.2 Methods

Thermal analyses

Differential scanning calorimetry (DSC) was employed to investigate non-isothermal crystallization at relatively low cooling rates. Use was made of a Mettler-Toledo 823e/700 module in combination with a Cryostat intracooler. A sample of about 5 mg was placed

in a 40 μm standard aluminium crucible. The sample was heated at 20 °C/min from 25 °C to 180 °C, held at that temperature for 5 minutes to erase any thermal history and subsequently cooled at rates, $\dot{T}$, of 4-20 °C/min to 0 °C. The equipment was calibrated for static temperature, thermal lag, and heat of fusion using indium and zinc. Nitrogen was used as a purging gas.
For relatively high cooling rates, non-isothermal crystallization was studied using a fast scanning chip calorimeter (FSC) Flash DSC 1 of Mettler-Toledo in combination with a Huber intracooler TC100 and UFS-1 sensors [19–21]. Samples were prepared by microtoming and microscope-aided cutting. The specimen was heated at 100 °C/s to 150 °C and kept at that temperature for 1 second, which is sufficient to remove all thermal history due to the limited sample dimensions. Subsequently, the sample was cooled to -50 °C in a range of 50-2000 °C/s. Scan rates below 50°C/s were not investigated, the signal to noise ratio became unsatisfactory due to the low sample mass. Above 2000 °C/s, the cooling rate selected could not be maintained until the end of the crystallization process. Nitrogen was used as a purging gas, no corrections for thermal lag effects were included since the sample dimensions were considered minimal. The FSC sensor was conditioned and temperature-corrected according to the specification of the instrument provider.

Small angle light scattering

Small angle light scattering (SALS) combined with a temperature jump-stage experiments were performed to measure the temperature dependent spherulitic growth rate and nucleation density up to high levels of undercooling. Samples of approximately 5.5 mm in diameter, 30 μm in thickness and a mass of 0.5 mg were prepared by melt-compression moulding a small amount of granular material sandwiched between two cover glasses of 9 mm in diameter and a thickness of 150 μm each. The specimens were placed in a custom-modified JHT-350 temperature-jump stage [75] (Linkam, Japan), which consists of two separately controlled heating stages and allows for the sample to be rapidly transferred from the *hot* stage, set to 150 °C, towards the *cold* stage, set at the desired temperature for crystallization, by means of an aluminium slide. The sample was transferred to and kept at the hot stage for 1 minute to erase all structural history. Due to the large capacity of the heating stages and the small sample size, cooling rates were reported in the order of 300 °C/s [75]. Custom modifications by our group consist of a remotely controlled and air pressure driven actuator, connected to the aluminium slide, to quickly transport the sample back and forth between the stages and at reproducible speeds, see Fig. 3.2. Experiments were performed in duplo at each set temperature. The temperature of both stages was corrected using a calibrated K-type micro-thermocouple connected to a temperature readout device (USB-9162, National Instruments).

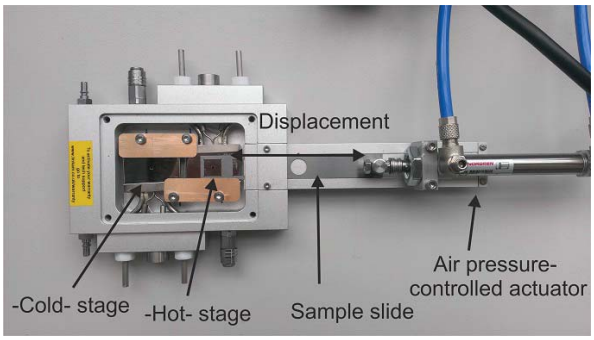

Figure 3.2: The custom modified JHT-350 temperature-jump stage (without top cover).

The light-source consisted of a He-Ne laser ($\lambda = 6328$ Å, JDS Uniphase, USA) at constant intensity which was directed perpendicularly through the sample, which itself is located in between two crossed polarizers (H_v polarization mode). The resulting pattern was projected onto a semi-transparent screen and recorded with a high-speed Orca Flash 4.0 SCMOS type camera (Hamamatsu, Japan) equipped with a 25 mm Schneider-Kreuznach Xenon lens. No corrections for transmission, refraction and reflection were made [76], since absolute intensities were not needed for our analyses. Sample to projector screen distance was 122 mm, the scattering angle was calibrated with a fine grid and pixel size was 88.75 μm x 88.75 μm. Images were recorded continuously in time at rates in the range of 50-200 Hz, controlled by Hokawo software (Hamamatsu, Japan) and corrected for background noise and melt contribution. Integration of the patterns was performed by using Fit2D software (ESRF, France) to obtain scattering intensity, I_0, versus the scattering angle, q. For data reduction purposes, only one lobe of the characteristic four-clove pattern was selected for recording. A Lorentzian curve was fit to each pattern to smoothen the data and the position of the peak of this curve was determined. Experiments were performed in the set temprature range of 78-104 °C. Above 104 °C, the maximum scattering angle merges with the beamstop and the peak position could no longer be traced as function of temperature. Below 78 °C, the first scattering frames recorded already showed signs of ongoing crystallization.

Dilatometry

Dilatometry experiments were performed with the Pirouette pVT$\dot{\text{T}}-\dot{\gamma}$ apparatus (IME technologies, the Netherlands) [12, 77]. It allows investigation of the evolution of specific volume of polymers as a function of temperature, pressure, cooling rate and shear rate by measuring the volume change of a sample. The apparatus requires ring-shaped samples with a mass of ∼75 mg, an outer diameter of 20 mm, thickness of 0.5 mm and height of approximately 2.5 mm, which were pre-produced from granular material using a Babyplast injection molding machine (Rambaldi, Italy) equipped with a custom build mould. Experiments were performed in isobaric cooling mode at pressures of 100 and 500 bar. The sample was heated to 180 °C and kept at that temperature for 5 minutes to erase all thermal

history. Finally, the piston and die were cooled by a constant flux of air which resulted in an initial cooling rate of 1.0 °C/s (measured between 180 and 130 °C). Experiments with flow were carried out over a wide range of shear rates, $\dot{\gamma}$ (from 3 to 180 1/s) and a constant shear time of one second at the chosen shear temperatures.

X-ray diffraction

The molecular orientation of processed samples from dilatometry was investigated using 2D Wide-angle X-ray diffraction (WAXD). Measurements were performed at the Dutch-Belgian (DUBBLE) beamline BM26 of the European Synchrotron Radiation Facility in Grenoble, France [13]. The source-ray photon wavelength was set to 1.033 Å, with an X-ray beam of 300 μm in diameter. Patterns were acquired with an exposure time of 10 seconds. All patterns were collected by means of a Frelon CCD detector (Photonic Science, UK) with 2048 x 2048 pixels of 48.83 x 48.83 μm at approximately 160 mm from the sample surface. Data was integrated, corrected for static noise, and background subtracted using the Fit2D software package (ESRF, France).

Rheological characterization

Small amplitude oscillatory shear (SAOS) measurements were performed with an MCR 502 Rheometer (Anton Paar, Austria), equipped with a plate-plate geometry (diameter 25 mm). The characteristic rheological properties, i.e. storage and loss moduli, G' and G'' and loss angle, δ were obtained over a wide range of temperatures (from 115°C to 180°C) and angular frequencies, ω (from 0.1 1/s to 300 1/s). To determine properties in the linear viscoelastic regime, the strain, γ, applied was chosen after strain sweeps and set to 5% for all measurements. Time-temperature superposition has been applied to obtain a mastercurve at a reference temperature of 160 °C.
The polymer was also characterized in simple extension using a SER2-P SER Universal Testing Platform [78] fixture hosted on the MCR 502. Uniaxial extension experiments were performed at 160 °C, using various strain rates up to the maximum achievable Hencky strain, ϵ_H, of four. All the experiments were performed under constant nitrogen flow to avoid sample degradation.

3.3 Results and Discussion

First, quiescent crystallization of the m-LLDPE grade is discussed, followed by characterization of the solidification kinetics using thermal and scattering methods. Next, the crystallization model is discussed for both the primary and secondary processes. Finally, the effect of flow and pressure is characterized using rheology and dilatometry, and optimal values for scaling parameters describing flow-induced crystallization (FIC) were obtained for a model that is based on molecular stretch.

3.3.1 Thermal characterization

The type of polymerization process provides that m-LLDPE is a substantially linear polymer with a controllable amount of short branches. The intermolecular distribution of these side chain branches is called homogeneous when the distribution of branches between the molecules is narrow, while the sequence length distribution between branches can still be broad. The longer ethylene sequences, having a higher melting point, crystallize faster [79–81] and fold into stacked lamellae that span the spherulite from the free melt, defined as primary crystallization [57]. Quenching the melt at increasing rates smears out this process over a larger temperature range and/or postpones crystallization to lower temperatures due to insufficient time for nucleation and growth [31, 82]. Crystallinity may further increase due to secondary crystallization of the shorter sequence length chain sections, even before spherulitic impingement [83]. They form lamellar stacks in the amorphous regions between the primary lamellae inside the spherulite [83, 84].

The influence of comonomer content is reflected by a second peak in the crystallization process commonly observed at low temperatures in DSC [58,59]. During the lamellar folding process, the length of the side chain determines whether or not it is excluded from the crystal lattice [52, 55, 85]. As the already formed lamellae restrict the topological movement of the remaining sequences, these are unable to attain the chain folding process. Hence, at high levels of undercooling, a second stage of secondary crystallization yields a granular morphology consisting of small bundled structures or loosely packed ethylene sequences [55, 58, 59, 86]. A simplified, schematic, and time discretized overview of the primary and two stage secondary process is given in Figure 3.3.

For each DSC and FSC experiment, the total baseline subtracted heat capacity, or the excess heat capacity, is composed of the contributions of the crystallization processes observed, i.e. one primary and two secondary crystallization events. Peak deconvolution of the signal is used to determine each process as function of temperature, see Figure 3.4. In our approach, the primary process is marked by the symmetric fraction of the sharp peak at high temperatures, and is described by a Gaussian function.

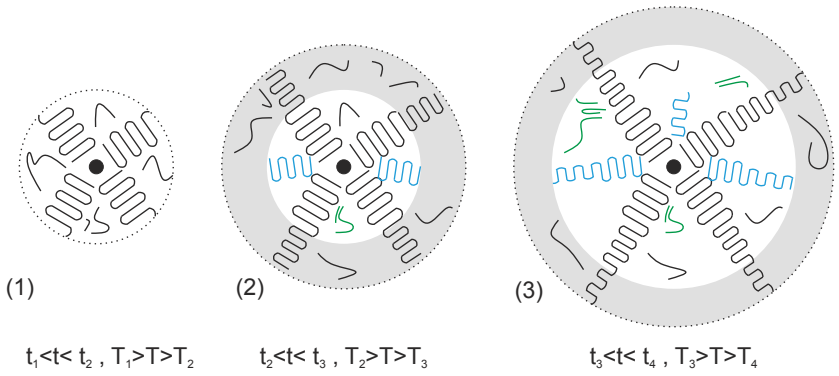

Figure 3.3: Schematic time discretized overview of primary and secondary crystallization process during cooling. (1) A nucleated spherulite grows in time as function of temperature, fast growing primary lamellae are formed from the most linear molecular sequences. (2) Shorter sequence lengths induce secondary lamellar growth in the remaining amorphous regions. Lamellae gradually become thinner with undercooling according to classical theories [87]. (3) Finally, at high undercooling, free chain sections locally order into small bundled structures.

A pronounced exotherm with a peak at ∼60°C due to bundle like features was best described using a much broader Lorenzian function. The lamellar insertion process that rapidly follows primary crystallization at slightly higher undercooling and the corresponding heat release provides the peak with high level of asymmetry. Depending on the comonomer content, a separate crystallization peak or a distinct shoulder is observable. It is assumed that the heat capacity not included in both peak functions can be fully attributed to the insertion of lamellae, see again Figure 3.4, which can be described with an n-number of Gaussian functions versus temperature, representing multiple lamellar insertion processes with decreasing lamellar thickness [87]. The deconvolution of the DSC-signal in these three contributions is, to our knowledge, not done before.

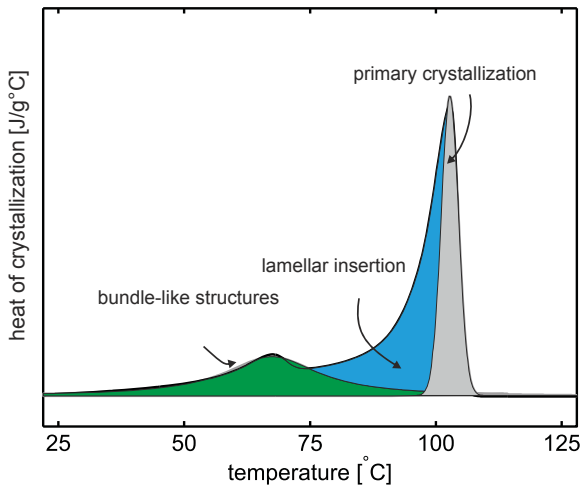

Figure 3.4: Schematic of the peak deconvolution process of the measured excess heat capacity.

Good fits of the peak functions to the data were always obtained, as is shown in Figure 3.5, where both DSC and FSC measurements are displayed, i.e. for low and high cooling rates, including the determined peak functions.

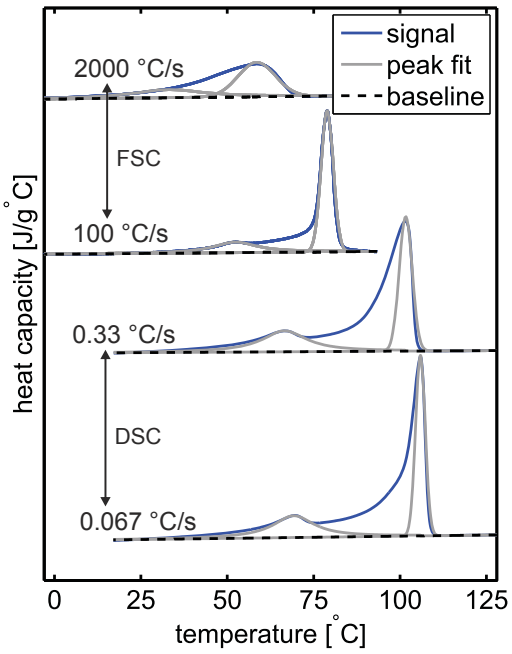

Figure 3.5: Summary of the peak fitting process of the excess heat capacity during cooling in the scan rates investigated for DSC and FSC.

Regarding conventional DSC experiments, crystallinity was calculated from the integrated peak, which was normalized for sample mass and cooling rate. The (linear) extrapolated heat capacity of the melt was used as a baseline [88]. The transitional entropy for polyethylene, $\Delta H(T)$ was taken from literature [89] and assumed to be a function of temperature only. We do not distinguish between the folding energy of lamellae and bundle-like features. For the FSC sample, the same protocol was applied, with the sample mass determined iteratively at ~400 ng by matching the amount of primary crystallinity calculated at the slowest cooling rate with FSC to the value obtained at the highest rate with DSC. It was assumed that in this range of cooling rates, primary crystallization was not suppressed, i.e. complete space filling is obtained.

When crystallinity is plotted versus temperature, for example for 200 °C/s in Figure 3.6a, it becomes clear that the primary process fully covers the first, steep increase at high temperatures. This rapid process covers a maximum of 15.2 % of total crystalline volume, which corresponds to values also found by Goderis et al. [60]. At this stage, the crystallinity distribution inside the spherulites is presumed inhomogeneous (see Figure 3.3). Upon further cooling, crystallinity will develop more slowly via lamellar insertion, the rather sharp transition point at approximately 50 °C corresponds to bundle-like structure formation.

Both techniques used cover together a wide range of cooling rates, albeit with a large gap in between roughly 10^0 and 10^1 °C/s, see Figure 3.6b. At low rates a more or less constant crystallinity distribution was observed for primary- and for both stages of secondary crystallization and for all conditions. In the case of the FSC scan rates, a gradual decrease of the total crystallinity was obtained mainly caused by a reduced level of lamellar insertion, a process which is slow compared to primary growth. Hence, when the time available for crystallization decreases the average crystallinity in each spherulite will reduce. The drop in the total crystallinity is outside the reach of both our DSC and FSC setup (between 10^0 and 10^1 °C/s). Only at very high cooling rates a minor decrease of the primary crystallinity is noted. For many semi-crystalline polymers is it possible to obtain a fully amorphous material by rapid cooling the sample from the melt at a critical cooling rate, $\dot{T}_{crit}$. Currently, to the best knowledge of the authors, this is not yet reported for m-LLDPE. From the data plotted here, $\dot{T}_{crit}$ is estimated to be in the order of 10^6 °C/s.

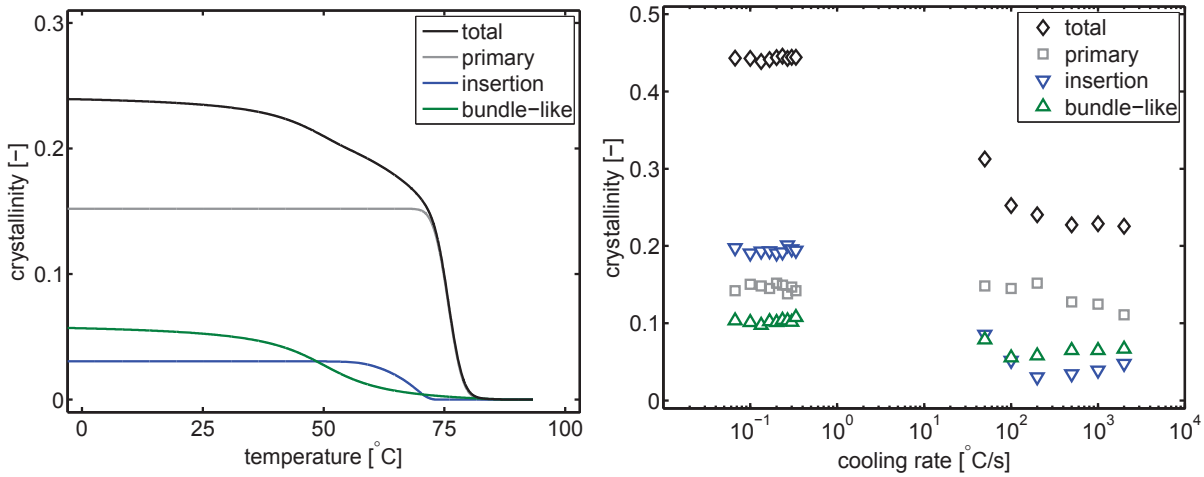

(a) (b)

Figure 3.6: Deconvoluted crystallinity versus temperature at 200 °C/s (a) and final crystallinity fractions for all cooling rates investigated (b)

The maximum crystallinity for each fraction, χ_i, was determined from the same figure, see Table 3.1, and used in our modelling section later on.

Table 3.1: Maximum crystallinity content for the primary-, lamellar insertion-, bundle-like fractions, and total crystallinity, respectively.

	$\chi^{\mathrm{p}}_{\infty}$	$\chi^{\mathrm{l}}_{\infty}$	$\chi^{\mathrm{b}}_{\infty}$	$\chi^{\mathrm{t}}_{\infty}$
[-]	0.152	0.2015	0.103	0.457

3.3.2 Small-angle light scattering

Light scattering of semi-crystalline polymers has been studied for an extensive amount of time and is commonly used to extract morphological details from polymers [84, 90–92]. The method was first applied by Debye and Bueche [93], and later on more detailed and complex theories were developed for polarized light scattering of common polymer morphologies such as single spherulites [76, 94, 95] and solid films with space-filling architectures [96]. Scattering in H_v mode is dependent on the size and anisotropy of the spherulitic entities. As a result, spherulitic growth can be detected by the changing scattering pattern and quantified from the integrated 2D scattering patterns. When it is assumed that only perfect spherulitic structures are formed, the average radius of the spherulites, R_{av}, can be determined by tracing the scattering vector with maximum intensity, q_{max}, in time using [97]:

$$R_{av} = \frac{4.09\lambda_0}{4\pi n_m sin(\theta_{max}/2)} \approx \frac{4.09}{q_{max}}. \tag{3.1}$$

wherein λ_0 is the wavelength of light in vacuum, θ the radial scattering angle and n_m the refractive index of the medium. In order to successfully investigate rapidly crystallizing polymers under (approximately) isothermal conditions, the challenge is to reach the desired temperature before any significant amount of crystallization takes place. In this work, the temperature jump-stage allows us to study crystallization of m-LLDPE up to high levels of undercooling, although no real-time measure for the actual sample temperature can be provided, such as in the setup of Ding and Sprueill [98, 99]. Reaching real isothermal conditions becomes critical for relatively high undercoolings and corrections might be required. We will discuss this issue in detail in the next section. The obtained time evolution of radii is displayed for three different temperatures only in order not to crowd Figure 3.7. These data were selected to provide an overview of the measurements in the temperature range investigated. Data is shifted in time with t_0, which represents the experimental time at which a clear peak in the scattering pattern was obtained.

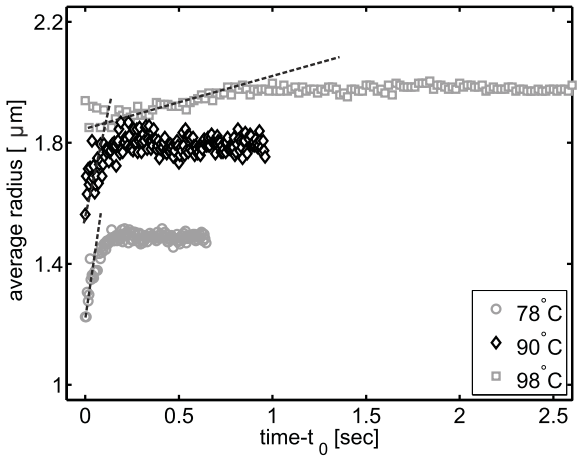

Figure 3.7: Average spherulitic radius versus time for three different temperatures measured using SALS. Dashed lines indicate the linear growth rate.

When a sufficient amount of scattering is recorded as a result of space filling spherulites, q_{max} can be determined accurately. Consequently, only the final part of linear growth and subsequent impingement is detected. Nevertheless, a first order function can be fit to the data to obtain the temperature dependent spherulitic growth rate, $G(T)$. The average growth rate is plotted for all experiments in Figure 3.8a and shows the characteristic bell shaped curve as commonly observed for various semi-crystalline polymers [100]. An apparent maximum growth rate is measured at ∼78 °C of approximately 3 μm/s. Although the temperature at the maximum growth rate is in agreement with earlier findings [99], the growth rate is much lower compared to values for ethylene copolymers reported in literature [101].

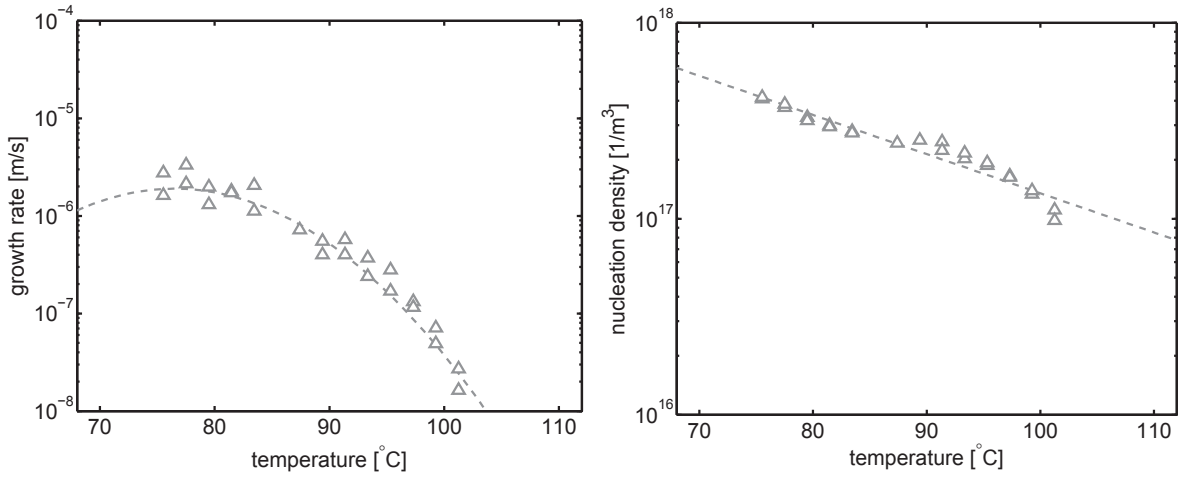

(a) (b)

Figure 3.8: Sperulitic growth rate (a) and nucleation density (b) versus temperature measuring using SALS. Dashed lines indicate the least squares approximation of Eqs. 3.4 and 3.5, respectively.

The temperature dependent heterogeneous nucleation density, $N(T)$, plotted in Figure 3.8b, was estimated from the final radius measured using [67, 68]:

$$\xi = 1 - exp(-\frac{4}{3}\pi R^3 N) \tag{3.2}$$

which can be rewritten

$$N = \frac{-ln(\frac{1}{2})}{\frac{2}{3}\pi R^3} \tag{3.3}$$

and shows the usual logarithmic decrease of the number of spherulites with temperature [6].

Temperature dependent functions for $G(T)$ and $N(T)$ can be obtained via least-square approximation of the measurements using:

$$G(T) = G_{max} exp\left(-c_g \left(T(t) - T_{Gref}\right)^2\right), \tag{3.4}$$

$$N(T) = N_{ref} exp\left(-c_n \left(T(t) - T_{Nref}\right)\right). \tag{3.5}$$

where G_{max} and N_{ref} are values at the reference temperatures T_{Gref} and T_{Nref}, respectively, while both c_g and c_n are constants. Good fits are obtained and included in Figure 3.8.

Next to the average size and number of the spherulites, SALS can also provide details about the type of crystal growth measured, therefore, the relative invariant, Q, the total integrated scatter intensity of the H_v patterns, is employed:

$$Q = \int_0^\infty I(q) q^2 dq. \tag{3.6}$$

Subsequently, Q is normalized with respect to the first frame (fully amorphous sample, 0) and final frame (fully crystalline sample, 1). The invariant is proportional to the mean square anisotropy within the spherulites, and increases linearly with space filling [84] in Figure 3.9a. The increase of Q after spherulitic impingement is an indication of an increased crystallinity or ordering degree within the spherulites as a result of secondary crystallization. Avrami analyses in Figure 3.9b confirms that, after start up phenomena, crystallization occurs via spherulitic growth (slope close to 3) and a considerable amount of secondary crystallization (slope close to 1) via one dimensional growth such as lamellar insertion.

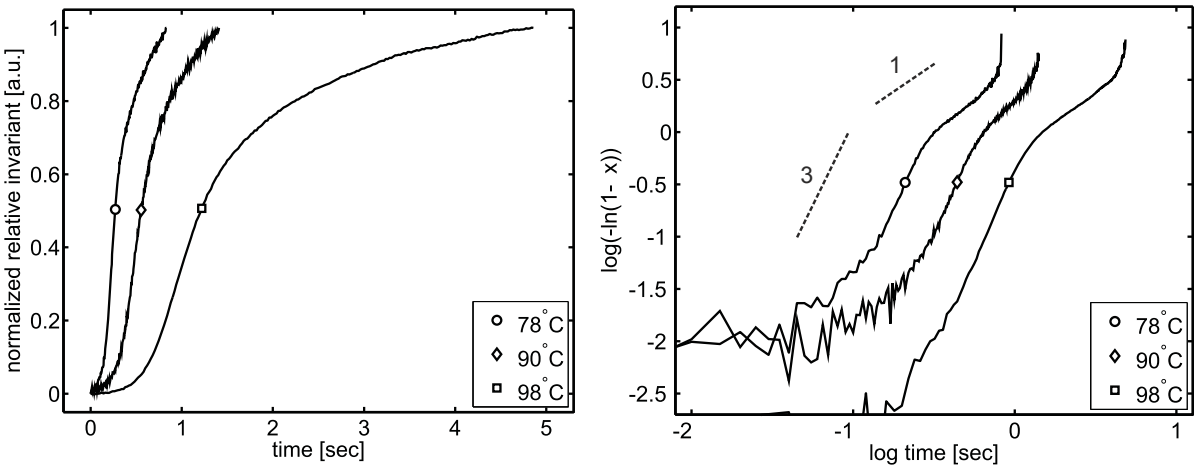

(a) (b)

Figure 3.9: Normalized relative invariant versus time at three different temperatures (a) and corresponding Avrami plot (b).

3.3.3 Primary crystallization model

The non-isothermal primary crystallization kinetics are calculated using the Schneider rate equations [102], a generalized form of the well-known Avrami analysis [67,68] that accounts for the effects of changing temperature during crystallization. This approach has been validated in a number of publications, cf. refs. [82, 103]. The evolution of space filling is obtained by solving a set of coupled differential equations to calculate the evolution of radius density, area density, and undisturbed volume fraction for spherulites from number density and crystal growth rate. These equations read

$$\dot{\phi}_3 = 8\pi\dot{N} \qquad (\phi_3 = 8\pi N), \tag{3.7}$$

$$\dot{\phi}_2 = G\phi_3 \qquad (\phi_2 = R_{\text{tot}}), \tag{3.8}$$

$$\dot{\phi}_1 = G\phi_2 \qquad (\phi_1 = S_{\text{tot}}), \tag{3.9}$$

$$\dot{\phi}_0 = G\phi_1 \qquad (\phi_0 = V_{\text{tot}}). \tag{3.10}$$

Here G denotes the spherulitic crystal growth rate and N the nucleation density, given as a function of temperature in Eq. 3.4 and 3.5, respectively. Finally, space filling is calculated from the undisturbed volume fraction, ϕ_0, using [67,68]

$$\dot{\xi}_p(t) = \left(1 - \xi_p(t)\right)\dot{\phi}_0(t). \tag{3.11}$$

wherein

$$\xi_p(t) = \frac{\chi_p(t)}{\chi_\infty^p}. \tag{3.12}$$

Figure 3.10 shows the primary crystallinity obtained from calorimetry and the crystallinity calculated from the FSC and DSC temperature profiles and the $G(T)$ and $N(T)$ from SALS measurements by the methodology described above. Upon immediate notice, it becomes clear that only the experiments from DSC are described accordingly. Here, independent of the cooling rates used, crystallization always takes place at approximately 100 °C, thus, only the SALS data obtained at low levels of undercooling describe the data well. For the high cooling rates, the calculated crystallization rate is too low and, consequently, the final primary crystallinity level is as well. In the next section, we analyse the SALS results in more detail to evaluate the measurement data at higher undercooling.

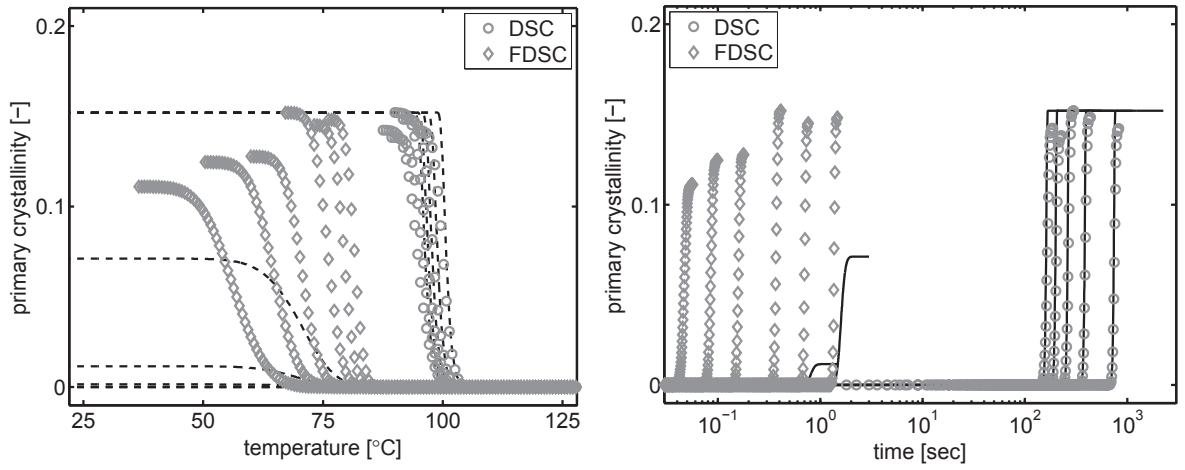

Figure 3.10: Primary crystallinity from calorimetry experiments versus temperature (a) and time (b). Dashed lines are the computed values with crystallization kinetics from SALS.

Temperature correction calculations

The design of the jump stage is such that the cooling rate of the support can be considered infinite. The polymer sample however will not reach the set temperature instantaneously. For low set temperatures this will lead to a discrepancy between the set temperature and the temperature at which crystallization takes place. To account for this, the transient temperature in the sample needs to be determined. Calculations were performed by solving the heat balance (using a built-in ordinary differential equation solver in MATLAB) on a 1D finite difference grid representing the experimental setup in Figure 3.11.

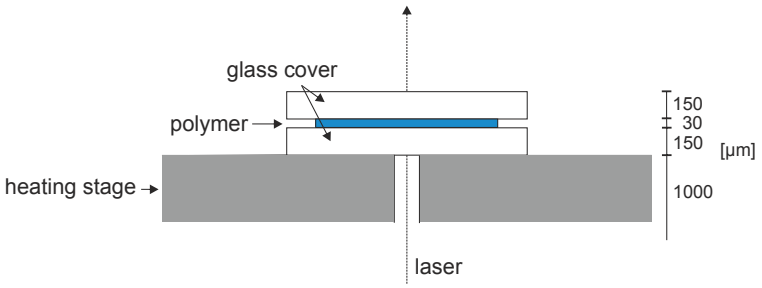

Figure 3.11: Cross section and dimensions of the sample and the temperature jump stage located in the SALS setup.

The heat balance is given by

$$\rho^k c_p^k \frac{\partial T}{\partial t} = \lambda^k \frac{\partial^2 T}{\partial x^2} + \rho^k \chi_\infty \Delta H \dot{\xi}, \tag{3.13}$$

with T the temperature and t time. Further, ρ denotes density, c_p is the heat capacity, and λ is the thermal conductivity. Superscript k denotes the material; either silver (heating element), glass (sample cover), or polymer. Values are given in Table 3.2. The last term in the right

hand side represents the heat release due to crystallization of the polymer, with $\Delta H(T)$ the heat of fusion [88], χ_∞ the final crystallinity of the material and $\dot{\xi}$ the crystallization rate as given by the Schneider rate equations, including the obtained functions for nucleation density and growth rate. We assume that the maximum reachable crystallinity in this temperature range consists of crystals grown during the primary and lamellar insertion process, from Table 3.1 we obtain $\chi^p_\infty + \chi^l_\infty = 0.35$.

Table 3.2: Parameters for energy balance [104].

	silver	glass	polyethylene
ρ [10^3 kg/m^3]	10.5	2.5	0.76
c_p [J/kg K]	233	0.5	3000
λ [W/mK]	429	1.05	0.23

The crystallization temperature is defined as the temperature at which space filling in the center of the polymer sample reaches 70%, which is similar to the crystallinity level at which the linear growth rate was determined in SALS analyses. In Figure 3.12 we present the results of this exercise. Figure 3.12a shows the calculated crystallization temperature versus the set temperature for the originally measured data. The dashed line shows the case where these would be equal. The corresponding temperature transients in the center of the polymer sample are presented in Figure 3.12b. Clearly, the crystallization temperature start to deviate from the set temperature from 92 °C downwards.

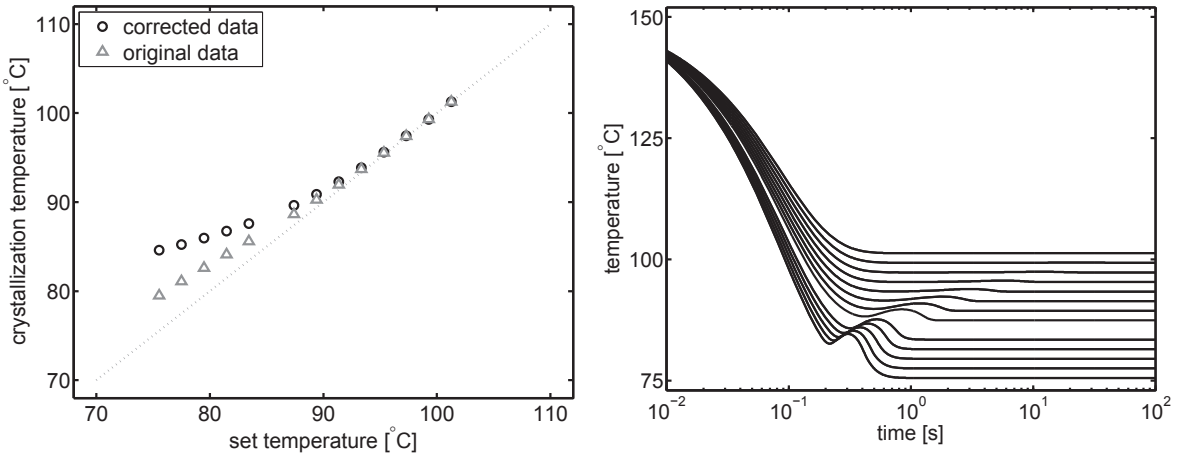

(a) (b)

Figure 3.12: Results of the heat balance calculations. (a) The calculated crystallization temperature versus the set stage temperature for measured data and corrected data (next section) and (b) the heat traces in the center of the polymer sample.

If the calculated temperature shift, $\delta T(T)$, is implemented as a correction to the SALS results, only part of the data will shift to higher temperatures, while both the growth rate and nucleation density values are maintained. Consequently, the functions determined in Eqs. 3.4-3.5 have to be re-evaluated.

Since δT is a function of the crystallization rate, thus of the measurement points themselves, see Eq. 3.13, a different approach is needed to calculate the correct material functions for N and G. From Figure 3.12a, it becomes clear δT is not significant for measurements above 90 °C (<1 °C). Thus, these points can be used in the corrected least-squares approximation of the nucleation density, $N^*(T)$. This number of data points is insufficient to determine a corrected bell-shaped growth rate function, $G^*(T)$. Instead, G^* was obtained by least-square optimization of the calculated primary crystallization fraction from calorimetry, wherein N^* is included for calculations. As expected, an excellent description of the primary crystallinity content is obtained in a range exceeding five decades in time, see Figure 3.13b. Parameter values obtained are displayed in Table 3.3 for both the original and corrected functions.

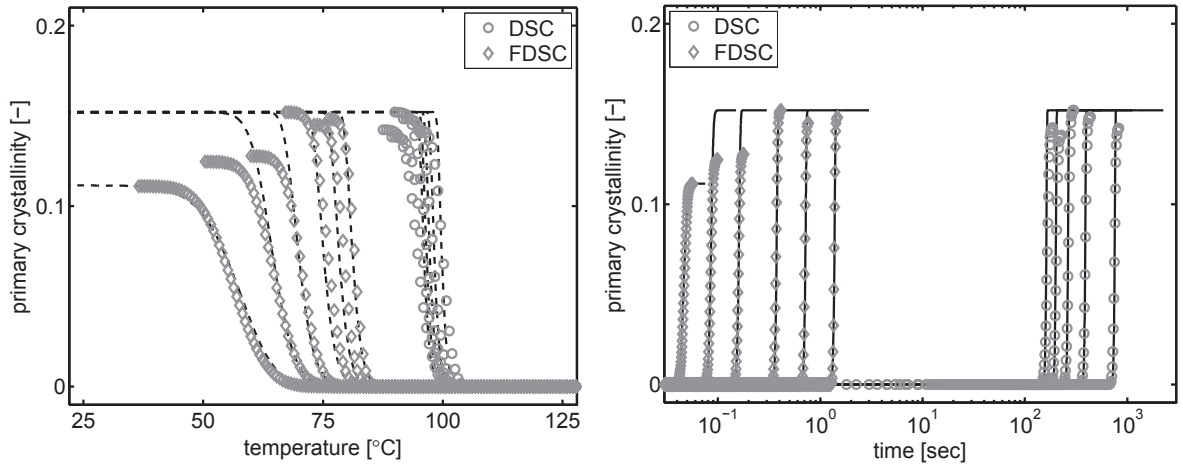

Figure 3.13: Primary crystallinity from calorimetry experiments versus temperature (a) and time (b). Dashed lines are the computed values with the temperature corrected function for nucleation and growth.

When the obtained growth rate function is verified, it becomes apparent that at lower temperatures, e.g. below 90 °C, G^* strongly deviates from G and a much higher maximum growth rate value is obtained, which ensures a significant crystallization rate even at low temperatures. The values of G_{max} and T_{Gref} show good agreement with literature [99, 101]. When G^* and N^* are implemented in Equation 3.13 and δT is again calculated, both shifted measurement data for N and G correspond with both G^* and N^*, see Figure 3.14. Data above 90 °C still shows a neglectable δT and overlaps the set temperature during the SALS measurements, see also Figure 3.12a. This confirms the accuracy of our calibration and analyses methods to calculate the growth rate and nucleation density, but simultaneously shows the SALS setup cannot be used for this material below 90 °C without additional heat balance calculations. The sample dimensions required do not allow for a micro-thermocouple to be included, for example, in between the two glass sample covers.

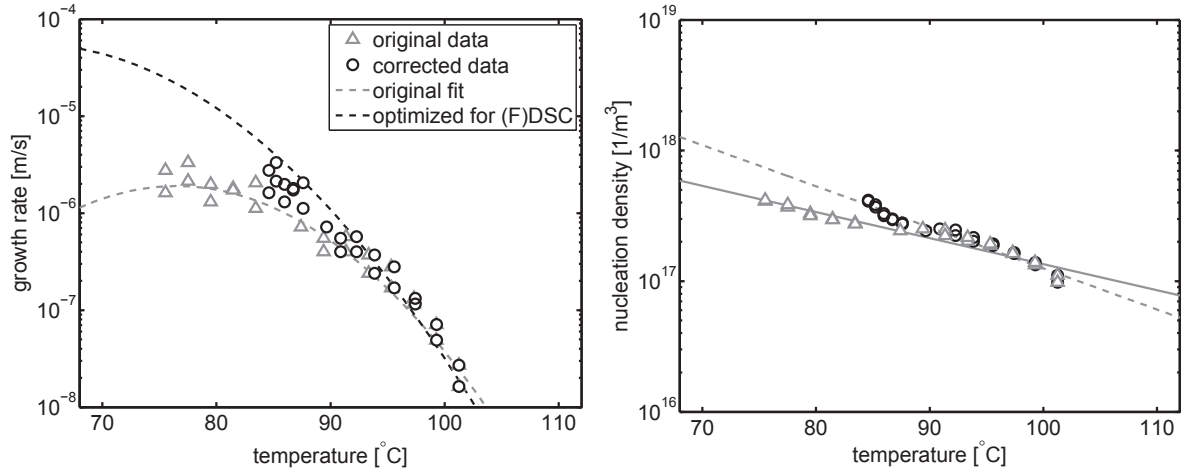

(a) (b)

Figure 3.14: Original and temperature corrected growth rate (a) and nucleation density (b) versus temperature.

Table 3.3: Parameters for nucleation and growth functions. Values for functions marked with '*' are obtained after temperature correction.

	$G(T)$	$G^*(T)$
G_{max} [m/s]	$1.897\ 10^{-6}$	$5.548\ 10^{-5}$
c_g [1/K^2]	$7.1\ 10^{-3}$	$5.6\ 10^{-3}$
T_{Gref} [K]	349.5	336.5
	$N(T)$	$N^*(T)$
N_{max} [1/m^3]	$1.349\ 10^{17}$	$1.257\ 10^{17}$
c_n [1/K]	$4.60\ 10^{-2}$	$7.24\ 10^{-2}$
T_{Nref} [K]	383	383

3.3.4 Secondary crystallization model

The total crystallinity fraction, including the increase of crystallinity due to secondary crystallization, can be expressed in terms of a convolution integral [70, 72]:

$$\chi(t) = \int_{\tau=0}^{t} \dot{\xi}(t-\tau)\chi_\infty(t)\,d\tau, \tag{3.14}$$

where χ_∞ is the maximum value of crystallinity allowed by the external conditions experienced by the sample [105]. If each spherulite has an initial (primary) crystallinity equal to χ_∞^{p}, the evolution of the maximum crystallinity during solidification yields:

$$\chi_\infty(t) = \int_{\tau}^{t} \dot{\chi}_\infty(T(t))\,dt + \chi_\infty^{p}. \tag{3.15}$$

Here, the increase of the maximum crystallinity, $\dot{\chi}_\infty$, can be expressed as a strong function of the environmental conditions, e.g. temperature, and the current amount of remaining

amorphous material using, similar to Equation 3.11:

$$\dot{\chi}_\infty((T(t)) = \sum(1-\xi^i_\infty)^{n_i}K_i(T), \tag{3.16}$$

wherein n_i is an *Avrami-like diffusion constant* that provides a strong dependence on the current amount of amorphous material,

$$\xi^i_\infty = \frac{\chi_i(t)}{\chi^i_\infty} \tag{3.17}$$

where i denotes the multiple secondary crystallization processes and

$$K_i(T) = a_i exp\left(-b_i\frac{\left(T-T_{ref,i}\right)^2}{T^2}\right), \tag{3.18}$$

is introduced as a temperature dependent rate function with constants a_i, b_i and $T_{ref,i}$. Their context is briefly discussed. The reference temperature, $T_{ref,i}$, corresponds to the temperature of maximum rate, a_i, of secondary structure formation. The value for b_i governs the width of the function, i.e. determines the temperature range in which secondary morphologies are able to form. Subscripts l and b are used for lamellar insertion and formation of bundle-like structures, respectively. The maximum crystallinity values for each process, χ^{i}_∞, in Eq. 3.17 are obtained from calorimetric analysis and were provided earlier in Table 3.1.

By employing the convolution integral approach, nucleated spherulites that have grown for a longer period in time, i.e, those that are formed at higher temperatures, will contain a higher amount of secondary crystallinity. The contributions of both the lamellar insertion and bundle-like ordering process were determined versus time and temperature from calorimetry. With the primary process described accurately, parameters for the rate functions can be determined. Typical initial values for this process could be estimated from the calorimetry results. Results of applying this model are shown in Figure 3.15 and parameter values are summarized in Table 3.4. The model is able to describe the multiple crystallization processes well, especially for conventional DSC data. Here, the onset of the lamellar insertion process starts already during the fast primary space filling process. Also the inflection point that marks the bundle-like ordering is captured well. Regarding the FSC experiments, good agreement is obtained in most cases. The final crystallinity level decreases with cooling rate although the final values and secondary processes are not always described accurately.

Parameters for the rate functions are shown in Table 3.4, both rate functions are displayed in Fig. 3.16. The reference temperature, $T_{ref,i}$, is lower for the bundle-like process, coherent with calorimetry measurements, clearly this process is dominant at low temperatures ($< 60°C$). The maximum rate, a_i, is found to be orders of magnitude higher for the bundle-like process; the scaling parameter, n_b in Eq. 3.16, provides the secondary crystallization rate with a strong dependency on the remaining crystallizable amount of amorphous material, consequently, a_b is relatively large.

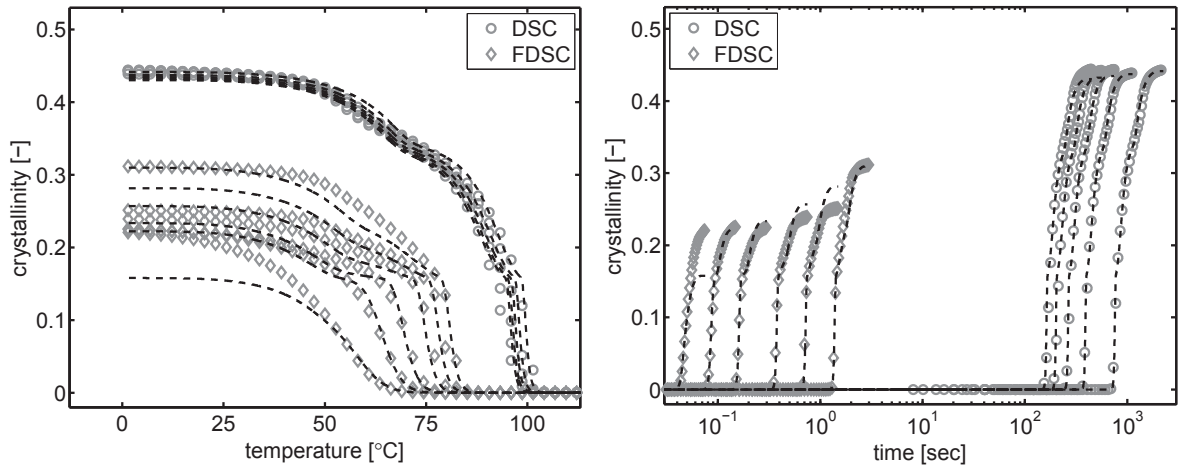

(a) (b)

Figure 3.15: Total crystallinity from calorimetry experiments versus temperature (a) and time (b). Dashed lines are the computed values with the model for primary and secondary crystallization.

Table 3.4: Constants for each secondary crystallization process in Eqs. 3.16 and 3.18.

	K_l	K_b
a_i [1/s]	0.485	$1.034\ 10^3$
b_i [-]	963.78	817.02
$T_{ref,i}$ [K]	339.6	297.6
n_i [-]	3.32	8.45

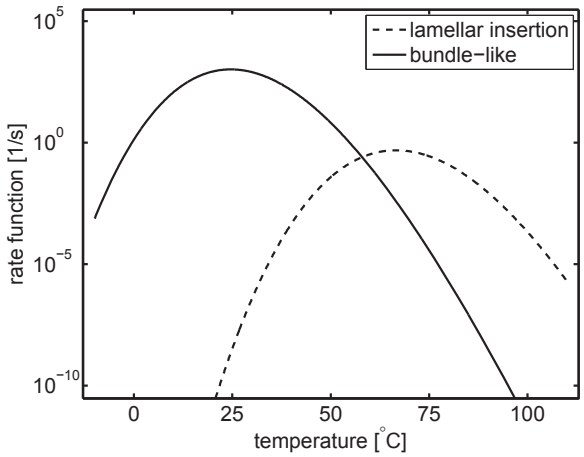

Figure 3.16: Rate function, K_i, of both secondary crystallization processes versus temperature.

3.3.5 Extended dilatometry

Using the Pirouette, the influence of the thermomechanical history during cooling was investigated by applying flow as a step function of one second in a range of shear rates, similar to cf. refs. [73, 106]. The shear temperature, $T_{\dot{\gamma}}$, was chosen such that the undercooling, $\Delta T(p)$, was 0 and 5 °C by taking into account the pressure corrected melting temperature, $T_m(p)$. This level of undercooling was chosen such that we get clear but not too strong effects of the flow applied. $T_{\dot{\gamma}}$ is defined as:

$$T_{\dot{\gamma}} = T_m(p_0) + \kappa\,(p - p_0) - \Delta T, \tag{3.19}$$

where κ is the pressure shift factor taken at 27.5 °C/kbar as generally accepted for polyolefins [107], p_0 the atmospheric pressure in bar and ΔT the level of undercooling.
The melting temperature at atmospheric conditions was determined from standard DSC at 114.3 °C, see Appendix A. The investigated shear temperatures are summarized for each pressure in Table 3.5.

Table 3.5: Shear temperature during dilatometry experiments at both pressures investigated.

	ΔT = 0	ΔT = 5
100 [bar]	117 °C	112 °C
500 [bar]	128 °C	123 °C

To easily compare the influence of different thermomechanical histories on the crystallization process, rather than to focus on the absolute value of the specific volume, the raw data is converted in a normalized specific volume, ν^*, using:

$$\nu^* = \frac{\nu - \nu_s}{\nu_m - \nu_s}, \tag{3.20}$$

where ν is the measured specific volume, ν_s the specific volume in the solid state at 40 °C and ν_m the specific volume in the melt at 170 °C.

Results are plotted in Figure 4.1. The dilatometry curves consists of three different regions, the melt, crystallization and solid regime, from high to low temperatures, respectively. The 'dip' in the experimental data is caused by the shear pulse and cannot be avoided. In the case of 100 bar and ΔT = 0 (Fig. 4.1a), hardly any influence of flow is noticeable; the volume contraction associated to crystallization always begins at the same temperature and proceeds in the same temperature range. The major decrease of the specific volume originates from the primary crystallization process at ∼100 °C, in addition, a weak effect of second stage secondary crystallization is noted at ∼70 °C. Experiments at an equivalent pressure level with a reduced shear temperature, ΔT = 5 (Fig. 4.1b), show a clear influence of flow; the crystallization temperature increases a maximum of approximately 10 °C. For strong enough flow, the material partially crystallizes during the shear pulse. As a result of the applied shear, the molecules become arranged in flow direction, decreasing the melt entropy, thus increasing the driving force for crystallization. Molecular orientation stimulates the

formation of flow induced nuclei, which, depending on the conditions, can tremendously increase the rate of crystallization [6]. More pronounced effects of flow are found when the level of undercooling is kept constant and, at the same time, the pressure is increased (Fig. 4.1c,d). At elevated pressure, the nucleation barrier is reduced since the molecules are packed more closely together, inducing an enhanced crystallization rate with flow [73, 100]. Weak signs of a secondary crystallization process are found at 80 °C (a temperature shift of ∼10 °C with respect to the measurements at 100 bar due to the pressure difference). Figure 4.1d, containing the conditions at slightly higher undercooling, shows a vast influence of flow; crystallization sets in during or immediately after the shear pulse.

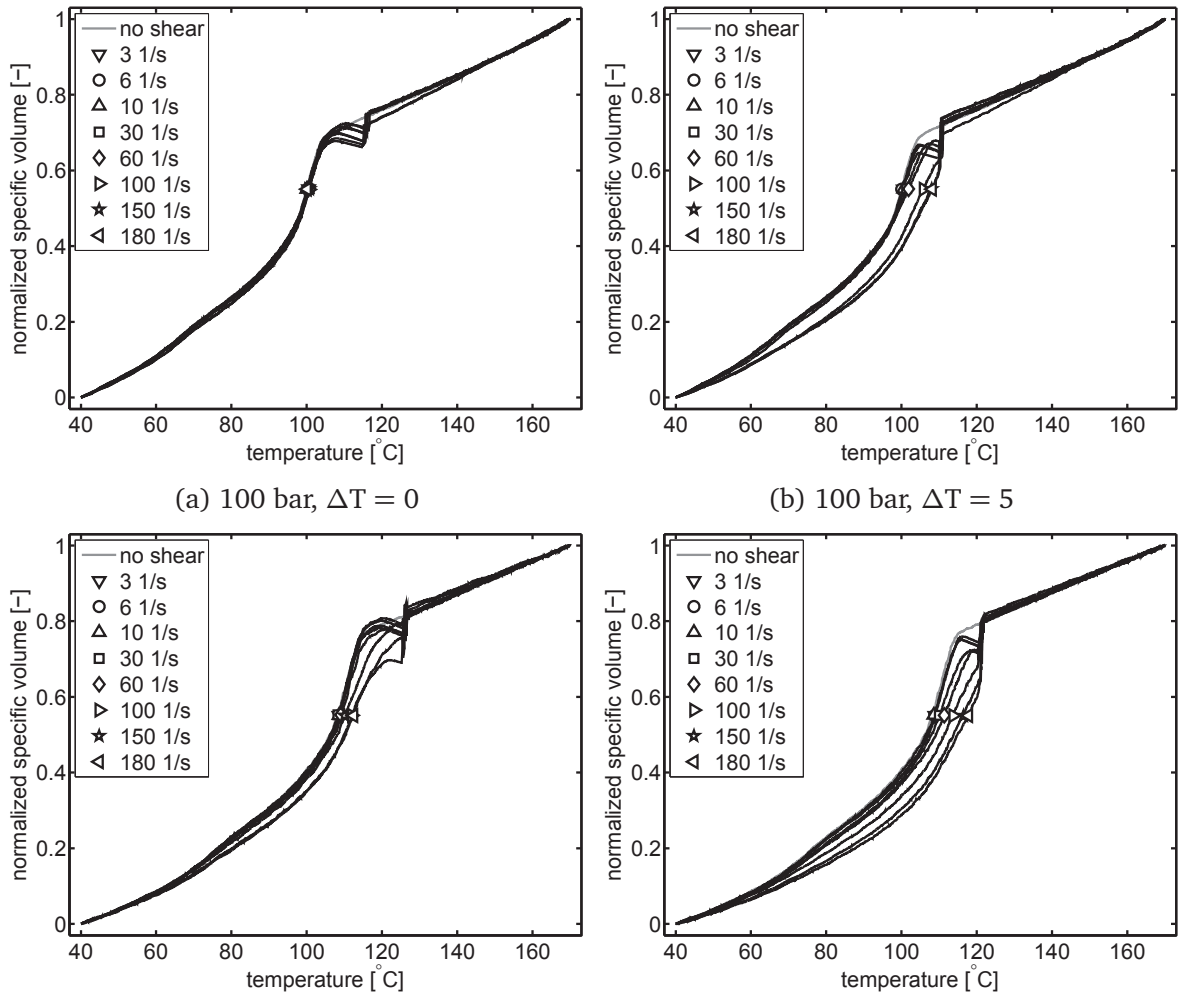

(a) 100 bar, $\Delta T = 0$

(b) 100 bar, $\Delta T = 5$

(c) 500 bar, $\Delta T = 0$

(d) 500 bar, $\Delta T = 5$

Figure 3.17: Normalized specific volume versus temperature for dilatometry experiments with flow at different shear temperatures at 100 bar (a,b) and 500 bar (c,d).

To distil the effect of shear on the different crystallization processes, i.e. primary and secondary crystallization, the first derivative of the normalized specific volume, $(\delta \nu^*/\delta \mathrm{T})$, is plotted versus temperature, which amplifies any change in curvature. A signal closely representing the calorimetry measurements (see Fig 3.5), but now with the influence of pressure and flow, is obtained in Figure 3.18. *Notice that, by presenting the PVT-results in this way, we have a DSC-equivalent signal that includes the influence of high pressure (upto 1200 bar) and, and this is unique, the influence of high shear rates (upto 180 1/s)*. Indeed, the signal originating from latent heat release and the rate of density change both scale with the crystallization rate. Under isobaric conditions, the specific volume drop during cooling is nearly linear at high temperature because the thermal expansion coefficient of the melt is only weakly a function of temperature. Similar to results from calorimetry, we can recognize the peak as a result of primary crystallization, which becomes asymmetric at lower temperatures because of the lamellar insertion process. Finally, at even lower temperatures, bundle-like crystallization is observed with a smaller, but clearly distinguishable peak. For the experiments with shear, a large spike in the derivative was obtained originating from the shear pulse. In order to present a clear figure, $(\delta \nu^*/\delta \mathrm{T})$ is plotted only from the moment directly after the shear pulse. For mild shear conditions, the derivative starts below the linear melt level because of the 'recovery' time needed after shear. In the case crystallization occurs during the one second shear pulse, the first part of the derivative is found above the linear melt level and during the primary crystallization peak. Regarding Figures 3.18b,c,d, the experimental conditions with a clear effect of flow, primary crystallization shifts towards higher temperatures. Here, flow increases the amount of point-like nuclei or induces the formation of oriented structures (shish), thus, the primary space filling process is enhanced. Compared to Figure 4.1, the effect of flow on the bundle-like crystallization process is now much more clear, evidently, the magnitude reduces with shear rate. With an increasing level of molecular orientation, the segmental motion of the side chains becomes constrained, moreover, the molecules are stretched in flow direction, providing that the side chains gradually become distanced from each other and can no longer form local crystalline aggregates.

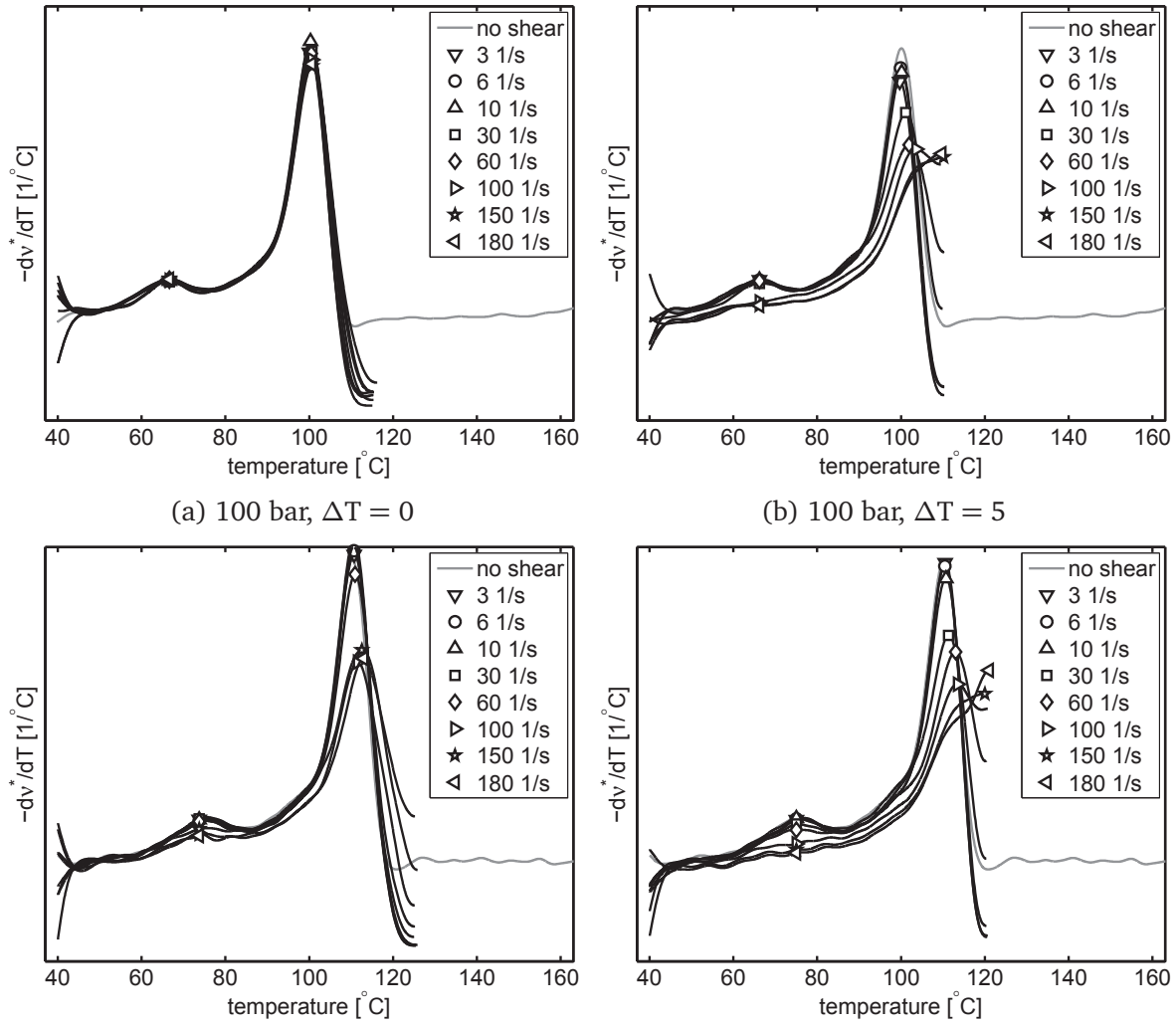

(a) 100 bar, $\Delta T = 0$

(b) 100 bar, $\Delta T = 5$

(c) 500 bar, $\Delta T = 0$

(d) 500 bar, $\Delta T = 5$

Figure 3.18: Derivative of the specific volume versus temperature from dilatometry experiments with flow at different shear temperatures at 100 bar (a,b) and 500 bar (c,d).

Flow strength: the Weissenberg number

The influence of the different processing histories applied is usually captured by converting the experienced thermomechanical history into a single parameter. A dimensionless shear rate number, i.e. the Weissenberg number, Wi, is commonly used to express the strength of flow applied and, simultaneously, proved to be useful for a rheological classification of the resulting type of crystalline morphology [106, 108, 109]. For low Wi-numbers, no clear effect on the crystallization kinetics is expected. For strong enough flow, part of the molecular chains (those with the higher molecular weight) become sufficiently stretched and oriented creating extra nuclei (flow enhanced nucleation), while the growth rate and growth-mechanism remain unaffected. At even higher Wi numbers, high amounts of shear induced nuclei are generated and oriented crystalline structures are formed and even the growth rate might be influenced [110]. Transitions between the different flow-induced crystallization regimes are defined by critical values of the Wi-number [108, 109]. As the influence of flow is thought to work via molecular stretch [108, 111], the Weissenberg number is defined as:

$$Wi = a_T a_P \tau_R \dot{\gamma}, \tag{3.21}$$

where $\dot{\gamma}$ is the applied shear rate and τ_R the characteristic rheological stretch relaxation time of the high molecular weight tail. The stretch relaxation time is obtained from fitting the model parameters for the XPP model [112], describing non-linear viscoelastic flow behavior, to viscosity data in uniaxial extension (see Appendix B), resulting in $\tau_R = 16.2$ s at a reference temperature of 160 °C and pressure of 1 bar. The temperature shift factor, a_T, is described with an Arrhenius type equation:

$$a_T = exp\left(-c_1\left(\frac{T_{ref} - T}{T_{ref}\,T}\right)\right), \tag{3.22}$$

with T the absolute temperature, T_{ref} a reference temperature of 160 °C and c_1 a constant. Values were obtained by time-temperature superposition of linear rheological data, also included in Appendix B. The pressure shift factor a_P is defined as [113]:

$$a_P = exp\left(\kappa\left(p - p_{ref}\right)\right), \tag{3.23}$$

where κ is $14{\cdot}10^{-9}$ Pa^{-1} for a relatively similar LLPDE grade [62] and p_{ref} a reference pressure of 1 bar. Note that, in this study, the relaxation times calculated by the XPP model were adopted, resulting in rather high Wi numbers.

Similar to Van der Beek et al. [106] a dimensionless crystallization temperature θ is used to express the change in crystallization kinetics measured:

$$\theta = \frac{T_c^{\dot{\gamma}}}{T_c^{Q}}, \tag{3.24}$$

where $T_c^{\dot{\gamma}}$ and and T_c^{Q} are the peak temperature of primary crystallization with shear and during quiescent crystallization, respectively (see Figure 3.18). In Figure 3.19, θ is plotted versus Wi. From this figure, we can distinguish between no influence of flow, mild influence and strong influence. In van Erp et al. [114], similar experimental results for an iPP grade are presented. They also observed the three different influences of the flow strength, but this resulted in three clearly separated regimes, i.e. for a given Wi-number there was (within experimental error) one dimensionless crystallization temperature only. Here, no such clear trend is observed; for the same Wi-number different transition temperatures are found depending on the thermomechanical history. It can be appreciated from the 2D WAXD figures included in Figure 3.19, obtained for the four samples processed at highest shear rate of 180 1/s, that a notable difference exists in final molecular orientation. For the sample processed at 100 bar and $\Delta T = 0$, a slightly polarized pattern is obtained, indicating the growth of flow-enhanced and/or oriented spherulites. For the other shear conditions, clearly a heavily oriented sample morphology was obtained after the imposed thermomechanical history. This apparent problem will be clarified in the next section where we present a model that captures these flow induced crystallization phenomena.

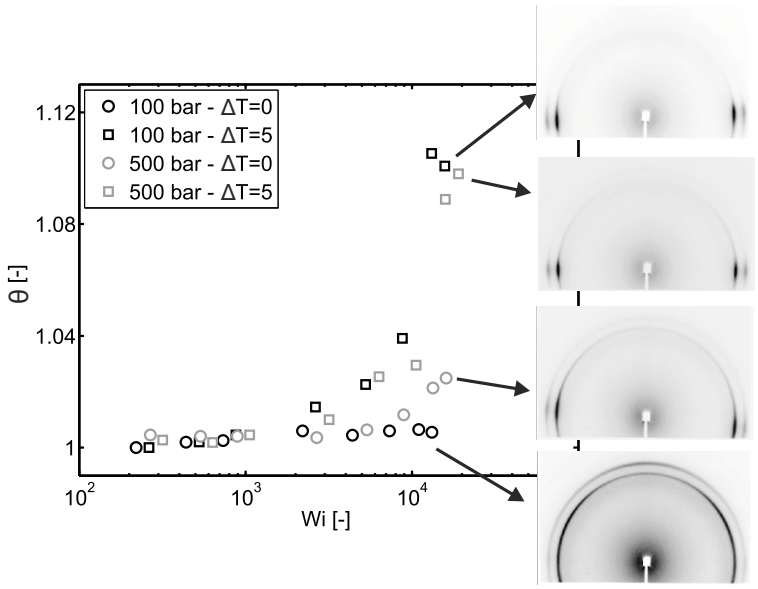

Figure 3.19: Dimensionless crystallization temperature versus Weissenberg number; experimental results, and 2D WAXD pattern of the samples at the highest shear rates investigated (shear direction is vertical).

3.3.6 Flow-induced primary crystallization model

A brief description is given of the FIC model developed in the Peters group [73,111,115,116], the reader is referred to literature for an in-depth evaluation. The model couples nucleation rate and formation of oriented structures to a qualitative predictive rheological model. It is stressed that the modelling section is assumed to apply to flow-induced *primary* crystallization only. Scaling parameters are determined to describe the obtained flow-enhanced crystallization kinetics as measured in the previous section (see Figure 3.19).
With flow, the total number of nuclei is considered the sum of quiescent nuclei, N_Q (Eq. 3.5), and nuclei originating from flow-induced crystallization, N_f:

$$N_{tot} = N_Q + N_f, \tag{3.25}$$

which is implemented in Eq. 7. The flow enhanced nucleation rate is modeled using a fourth-order dependence on the backbone stretch of the molecules in the high molecular weight (HMW) tail of the material, similar to [111]. It is envisioned that the stretch of the longest chains increases the number of aligned chain segments whose conformation is closer to the crystalline state

$$\dot{N}_f = g_n(\Lambda^4_{HMW} - 1) \tag{3.26}$$

wherein $g_n = g_n(T,p)$ is a temperature and pressure dependent scaling parameter.
The constitutive behaviour on a molecular level is calculated using the XPP model [112]. The relaxation times of the chains, τ_i, are corrected for shear- temperature and pressure. In addition, the flow-induced nuclei are assumed to act as physical crosslinks in the melt, increasing the relaxation times of the high molecular weight chains which is implemented with a linear dependency [116]:

$$\tau_i = a_T a_P \tau_{i0}(1 + \alpha N_f) \tag{3.27}$$

in which a_T and a_P are the temperature and pressure shift factors, respectively. The value of α is assumed at 10^{-18} for the m-LLDPE used.

The growth of oriented structures (shish) is assumed to be a non-selective process, in which all chains in the melt, regardless of their molecular weight, can participate. The average (AVG) conformation of the chains, in terms of orientation and stretch, is assumed to control the growth rate of the shish. The shish growth rate is given by:

$$\dot{L} = g_l(\Lambda^4_{AVG} - 1) \tag{3.28}$$

in which $g_l = g_l(T,p)$ is a scaling parameter dependent on both temperature and pressure.

A threshold flow condition needs to be surpassed before the length growth mechanism is activated and, consequently, oriented structures will form. Different criteria are suggested in literature; a critical shear rate, a critical amount of work, and a critical value for the stretch related to the high molecular weight tail (HMW-tail) of the molecular weight distribution. Here, similar to ref. [73], the time integral over the HMW-tail stretch history is used, a so-called effective stretch time:

$$t_{eff} = \int_0^t \Lambda_{HMW}\, dt \tag{3.29}$$

This rather simple criterium proved to work quite well for iPP [73] and, therefore, we will test if this is also the case for the m-LLDPE grade at hand. Notice that this criterium is similar (not the same) to a critical work criterium. Work reflects the average history of the deformation of all molecules, our criterium concerns the deformation history of the HMW-tail molecules only. The fibrillar growth mechanism is activated only if a critical value of the stretch history is surpassed.

The undisturbed volume can be calculated in time from the calculated nucleation density and shish length. In the isotropic case, i.e. below the critical stretch level, Eqs. 7-10 are combined with Eq. 3.25. For the case of an oriented system, a similar set of rate equations, first proposed by Eder [6], is employed:

$$\dot{\psi}_3 = 8\pi\dot{N}_f \qquad (\psi_3 = 8\pi N_f), \tag{3.30}$$

$$\dot{\psi}_2 = 4\pi N_f \dot{L} \qquad (\psi_2 = 4\pi L_{tot}), \tag{3.31}$$

$$\dot{\psi}_1 = G\psi_2 \qquad (\psi_1 = S_{tot}), \tag{3.32}$$

$$\dot{\psi}_0 = G\psi_1 \qquad (\psi_0 = V_{tot}) \tag{3.33}$$

with the nucleation rate $\dot{N}$, shish growth rate $\dot{L}$ and the spherulitic growth rate G. The morphology is described per unit volume by the total volume of shish-kebabs V_{tot}, their total surface S_{tot}, the sum of their lengths L_{tot} and the number of flow-induced nuclei N_f. Finally, the undisturbed spherulitical and oriented crystalline volume, ϕ_0 and ψ_0, respectively, are included in the Avrami model for space filling:

$$\dot{\xi}_p(t) = \left(1 - \xi_p(t)\right)\left(\dot{\phi}_0(t) + \dot{\psi}_0(t)\right) \tag{3.34}$$

For each dilatometry experiment, the crystallization kinetics were calculated from the time, temperature, pressure and flow history recorded and the framework presented above. The experimental data is used to determine values for the scaling parameters included in Eqs. 3.26, 3.28 and the critical effective stretch time, t_{crit}, from Eq. 3.29. The calculated effective stretch time is plotted versus the experimental dimensionless transition temperature in Fig. 3.20. The steep increase in θ is used to define t_{crit}, thus, from this value onwards, crystallization occurs via growth of shish-kebab structures. Data below t_{crit} covers either no influence of flow, or the enhanced point-like nucleation regime, and is used to determine values for scaling parameter g_n. Subsequently, data with an effective stretch time equal to or above the t_{crit} (and, simultaneously $\theta > 1.0075$, the flow regimes are really in two different quadrants, as it should be, see also [73]), is described using g_l. A small number of experiments, during which crystallization was already observed during the shear pulse (150 and 180 1/s at ΔT = 5 for 100 bar and 500 bar, respectively) are not included. These experimental conditions will be discussed separately.

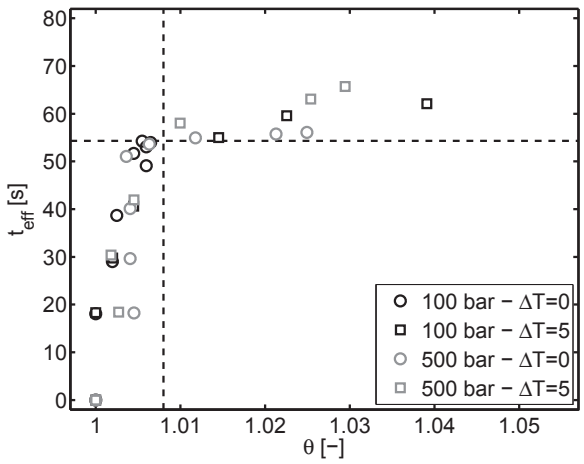

Figure 3.20: Integral over the stretch history versus the experimental dimensionless crystallization temperature.

Both the experimental and computed transition temperature are presented in Figure 3.21. The different transition temperatures at equal Wi-numbers are well captured by the model, which confirms the competence of the chosen critical stretch criterium, governing the onset of flow-induced structures. Unexpectedly, the experiments at 100 bar and $\Delta T = 5$ show a slightly higher transition temperature compared to the 500 bar and $\Delta T = 5$ experiments, while the Wi-number is slightly higher in the case of 500 bar experiments. This could have also been observed from the experimental data alone, Fig. 3.19, but is more clear with the model predictions included. At first thought, the increased pressure level and shear pulse at equal undercooling should provide the polymer melt with a more severe thermomechanical history. From both the measurements and model calculations, it can be deduced that the effect of undercooling on the relaxation times (via a_T) exceeds the effect of pressure (via a_p).

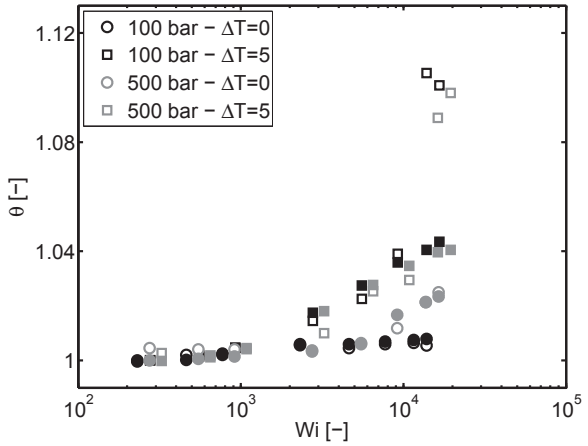

Figure 3.21: Dimensionless crystallization temperature versus Weissenberg number. Open symbols represent the experiments, closed symbols results from the model, respectively.

Table 3.6: Optimized values for flow-induced (scaling) parameters

	$g_n\ [m^{-3} \cdot s^{-1}]$	$g_l\ [m \cdot s^{-1}\ ]$
100 bar, $\Delta T = 0$	$2.1 \cdot 10^{13}$	n/a
100 bar, $\Delta T = 5$	$6.0 \cdot 10^{13}$	$9.1 \cdot 10^{-6}$
500 bar, $\Delta T = 0$	$1.6 \cdot 10^{13}$	$7.6 \cdot 10^{-6}$
500 bar, $\Delta T = 5$	$6.3 \cdot 10^{13}$	$8.1 \cdot 10^{-6}$
t_{crit}	54.3 $[s]$	
α	$1 \cdot 10^{-18}\ [m^3]$	

The optimal scaling parameters and critical stretch time are displayed in Table 3.6. For a sufficient number of experiments, i.e. temperatures, pressures and shear rates, one could chose simple expressions that then capture the parameter spaces of $g_n(T,p)$ and $g_l(T,p)$, see [73]. However, due to the limited number of pressure/temperature combinations (4), we provided parameter values only.

Finally, the PVT experiments that showed pronounced crystallization during the shear pulse, and were excluded from our previous analyses, are briefly considered. The parameter values as given in Table 3.6 were used to predict the transition temperatures for the experiments at 100 and 500 bar and $\Delta T = 5$, i.e. the four measurements with the highest transition temperature. It can be appreciated from Fig. 3.21, that the obtained model values for the transition temperature are much lower compared to our obtained experimental values. If we consider the occurrence of crystal growth during shear as a tremendous increase of the number of physical crosslinks, the measured transition temperatures can be approached by altering the α parameter, i.e. the dependency of the relaxation time on the number of flow-induced nuclei (Eq. 3.27). If α is chosen at $1 \cdot 10^{-11}$, relaxation times of the stretched molecules are increased, introducing extremely short crystallization times and/or crystallization during the shear pulse is approached, see Fig. 3.22.

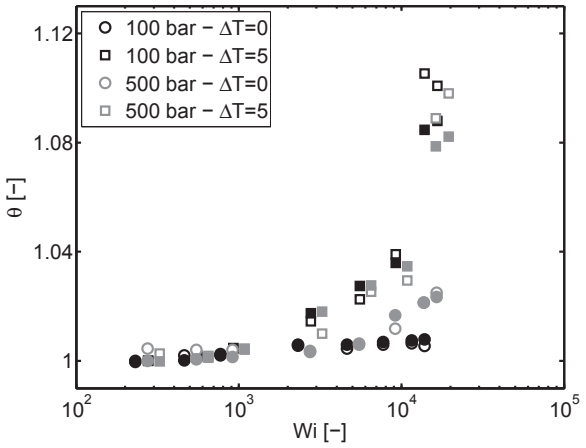

Figure 3.22: Dimensionless crystallization temperature versus Weissenberg number. Open symbols represent the experiments, closed symbols results from the model, respectively. A strong coupling between relaxation time and number of nuclei is included for the experiments where crystallization occurred during the shear pulse.

3.4 Conclusion

In this work, an extensive characterization of the crystallization kinetics of a m-LLDPE grade is shown as function of cooling rate, flow strength and pressure. A peak deconvolution process is applied to distinguish between the different crystallization processes observed in (fast-) differential scanning calorimetry, i.e. primary and two secondary crystallization processes. It was observed that with cooling rate, mainly the lamellar insertion process is suppressed, lowering the final crystallinity of the sample. The most important material functions to describe quiescent crystallization, the temperature dependent nucleation density and spherulitic growth rate, were obtained from SALS measurements accompanied with heat-balance calculations.
The proposed model to describe non-isothermal crystallization includes a convolution integral approach to describe secondary crystallization, for which the parameters were determined from the experiments. The model shows an accurate description of the crystallinity evolution in the range of cooling rates investigated (0.07 - 2000 °C/s).

Dilatometry is used to investigate the influence of flow strength and pressure and primary and secondary crystallization. It was shown that flow promotes primary crystallization, while the low-temperature bundle-like process is strongly reduced at the highest flow conditions. A simplified version a molecular-based nucleation model is used to describe the primary crystallization kinetics as function of flow and thermal history. Application of this model allowed for optimization of the scaling parameters g_n and g_l to describe the rate of flow enhanced nucleation and shish growth, respectively. When the strength of flow is expressed as the dimensionless Weissenberg number, different transition temperatures are found depending on the thermomechanical history. These results show that, in the case of m-LLDPE, the Wi-number does not provide an unambiguous rheological classification of the type of crystallization process. Even though, the model is able to capture the measured crystallization kinetics, reasserting the applicability of the critical stretch criterium selected.

Appendix A

The melting point at atmospheric pressure was determined at 114.3 °C from the peak in enthalpic heat from DSC at a heating rate of 10 °C/min. Data is plotted in Figure 3.23.

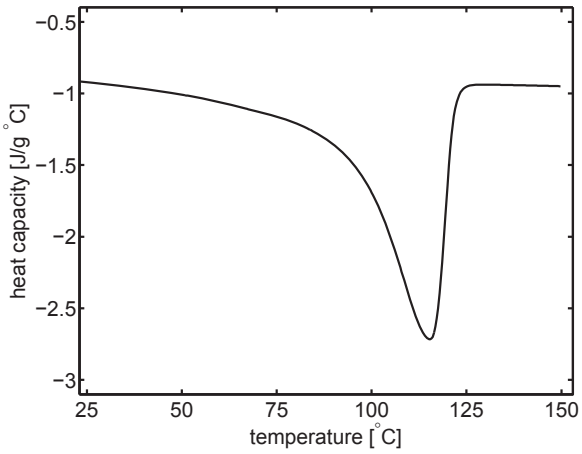

Figure 3.23: Heat capacity versus temperature during heating.

Appendix B

The rheological properties at a temperature of 160 °C are shown in Figure 3.24. An Arrhenius temperature dependence is found for the horizontal shift factors (a_T) and vertical shift factors (b_T) which are listed in Table 3.7, the latter, as expected did not show strong temperature dependence. The calculated value for the activation energy, E_a, is 47.686 kJ/mol.

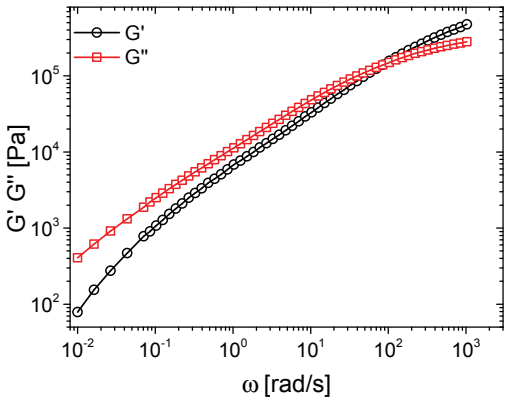

Figure 3.24: Storage (circles) and loss (squares) moduli at T_{ref}=160 °C. Full lines represent the fitting obtained with a Maxwell spectrum.

The relaxation time spectrum of the polymer in the melt state (at 160°C) can be calculated from the rheological properties measured. For that purpose, a discrete Maxwell relaxation time spectrum is used [117]. The set of relaxation moduli, g_i, and times, τ_i, are given in Table 3.7 which fit well the measured G' and G'' (solid lines in Figure 3.24).

Transient uniaxial elongational viscosities, η_u^+, at strain rates ranging from 0.1 to 25 1/s at 160 °C are given in Figure 3.25. The dashed line represents the linear visco-elastic (LVE) behaviour of transient elongational viscosity evaluated according to the Trouton-ratio, $\eta_u^+(t) = 3\eta_0^s(t)$ where $\eta_0^s(t)$ is the linear time-dependent shear viscosity evaluated from the relaxation spectrum at 160 °C. As typical for branched polymers deviation from linearity is observed: after a certain strain a positive stress deviation from the LVE envelope is noted (defined as strain hardening). The non-linearity was predicted using the XPP model [112]. Parameters q and the stretch time λ_s for the XPP model determined using the transient uniaxial viscosity are shown in Table 3.8.

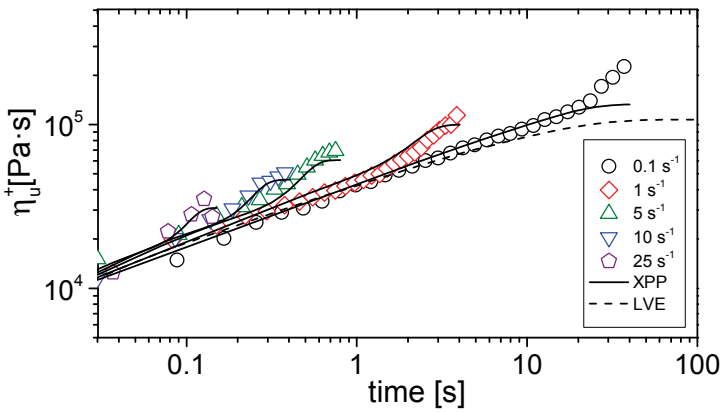

Figure 3.25: Transient extensional viscosity for the m-LLDPE studied over a range of strain rates measured at melt temperatures of 160 °C.The dotted lines represents the linear viscoelastic behavior and the full lines the XPP model fit.

Table 3.7: Rheological parameters for the material studied: Maxwell relaxation spectrum at 160 °C, g_i and τ_i. Time-Temperature horizontal and vertical shift factors, a_T and b_T.

modes	g_i [Pa]	τ_i [s]
1	$5.07\ 10^5$	0.000774
2	$2.06\ 10^5$	0.00581
3	$7.59\ 10^4$	0.0356
4	$1.86\ 10^4$	0.227
5	$5.57\ 10^3$	1.53
6	$1.48\ 10^3$	8.95
7	274	55.4
T [°C]	a_T	b_T
115	4.23	0.765
120	3.59	0.806
140	1.77	0.909
160	1	1
180	0.522	1.12
200	0.306	1.23

Table 3.8: Non linear XPP parameters for the material studied at 160 °C: stretch times, λ_i, and number of arms, q.

modes	λ_i [s]	q_i [s]
1	$1\ 10^{-6}$	1
2	$1\ 10^{-6}$	1.98
3	$1\ 10^{-6}$	3.02
4	0.021	3.02
5	0.0441	3.06
6	2.29	3.06
7	16.2	3.63

Chapter 4

Flow-induced solidification of high-impact polypropylene copolymer compositions: Morphological and mechanical effects

Reproduced from: Martin van Drongelen, Markus Gahleitner, Anne Spoelstra, Leon Govaert and Gerrit Peters, *Journal of Applied Polymer Science*, 132:42040, 2015

Abstract

Polypropylene-based impact copolymers are a complex composition of matrix material, a dispersed phase and many optional modifiers. The final heterophasic morphology of such systems is influenced significantly by the processing step, adding an additional level of complexity to understanding the structure-property relation. This topic has hardly been studied so far. The effect of thermal history and shear flow on the solidification process of three different compositions of a polypropylene-based impact copolymer, i.e. one base material and two compounds with either high density polyethylene or ethylene-co-octene added, is investigated. Samples are examined using differential scanning calorimetry, extended dilatometry, transmissions electron microscopy and, finally, tensile testing. With flow, the materials show pronounced flow-enhanced crystallization of the matrix material and deformed filler content. Compared to the base polymer, the stress-strain response of the compounded samples shows a lower yield stress and more pronounced influence of shear, reflected in the increasing strain hardening modulus.

4.1 Introduction

Advanced polypropylene (PP) materials are extensively being used for automotive parts like bumpers, body panels, dashboards and door claddings for many years. However, with increasing requirements in areas like advanced packaging and non-pressure pipes these grades find more and more applications. Mostly, heterophasic blends with crystalline PP as the continuous phase and an amorphous ethylene-propylene copolymer (EPR) as disperse phase, produced in multi-stage polymerization processes, are used [118–120]. The polypropylene matrix delivers the stiffness of the material whereas the rubbery inclusions act as impact modifiers. Thus, a material with balanced stiffness-impact behavior and even good optical performance can be obtained. When designing the property balance of such systems, multiple variations of the components are possible which normally require significant resources in either bench-scale or pilot-scale synthesis. An alternative for exploring a wide composition range with limited efforts is the production of model compounds, in which the phase structure of reactor-based systems needs to be matched as close as possible, including the frequent presence of a crystalline polyethylene (PE) component [121–125]. The latter can be used either for generating model systems for reactor-based products [122] or for property modification of these high-impact copolymers. Requirements for which the presence of crystalline PE in significant amounts has been found advantageous are limitation of stress whitening [126, 127] and scratch resistance [128], both being highly relevant e.g. for automotive interior applications. In any case, the morphology of such high-impact systems will be influenced significantly by the product shaping process, adding a further level of complexity to the crystal structure in PP.

While many papers deal with the effect of polymer composition on the equilibrium morphology of high-impact copolymers (i.e. as solidified from a quiescent melt) [120, 129, 130], the consequences for the morphology and the related mechanical performance in injection-moulded parts have been hardly studied. The limited number of publications dealing with morphological structures in injection-moulded or otherwise processed parts from PP/EPR model or reactor-based systems are mostly restricted to one composition [131, 132] or one set of processing conditions [133, 134]. In contrast to this limitation, significant progress has been made in recent years in understanding the effect of composition variations [77, 135], nucleation [136], and processing parameters [137, 138], on the crystal structure and the resulting mechanical performance of single-phase PP homopolymers or random copolymers. An extended dilatometer, an experimental setup to study pressure-volume-temperature (PVT) behavior with variable cooling rate and a well defined shear history, used in some of these cases [77,137], has been applied in the present study for studying three high-impact PP copolymer compositions under processing-relevant conditions. The objective of the investigation was to extend the understanding of the interaction between crystallization, phase structure formation and the mechanical properties of such systems as a function of cooling rate and flow conditions. We systematically investigated three different compositions

of a polypropylene-based impact copolymer, i.e. one base material and two compounds with either high density polyethylene or ethylene-co-octene added. Samples were examined using differential scanning calorimetry, extended dilatometry, transmissions electron microscopy and, finally, tensile testing. Flow conditions up to 180 1/s were examined, which is not of the magnitude of maximum shear rates (1000 1/s) but comparable to average shear rates as found in injection moulding. Moreover, this range of shear rates was found to cover the full range of solidification regimes.

4.2 Materials and Methods

4.2.1 Materials

A commercial EP copolymer of Borealis from a multi-stage polymerization process based on a 4th generation Ziegler-Natta catalyst was used as base material. The grade has a melt flow rate (MFR, ISO 1133, 230 °C / 2.16 kg) of 10 g/10min, an EPR content expressed as the xylene cold solubles content of 12.5 wt% and a total ethylene content of 8.3 wt%. Two commercial PE grades were used for modification of this base grade.

- High density polyethylene (HDPE) PE BS4641 of Borealis with an MFR (190 °C/2.16 kg) of 0.7 g/10min and a density of 964 kg/m^3, and
- Ethylene-*co*-octene plastomer (EOC) Engage EG8100 of Dow Chemical with an MFR (190 °C/2.16 kg) of 1.0 g/10min and a density of 870 kg/m^3.

This combination was selected because the melt viscosity of the modifiers is very similar to the EPR phase in the base polymer (as also expressed by the intrinsic viscosity). 17 wt% of each modifier was blended in a twin-screw extruder (ThermoPrism TSE24) at 200-240 °C, running the base polymer through the extruder as well to ensure an identical thermal history. Thus, a total of three materials were investigated, a base material, abbreviated as EP/EPR, and two model compounds with HDPE and EOC content, abbreviated as EP/EPR/HDPE and EP/EPR/EOC, respectively.

4.2.2 Methods

Thermal analyses

Differential scanning calorimetry (DSC) analysis was employed to characterize the melting and crystallization behavior of the different materials using a Mettler-Toledo 823e/700 module. The sample was heated with 10 °C/min from 25 °C to 210 °C, held at that temperature for 5 minutes and subsequently cooled at the same rate to 25 °C and,

after 1 minute to ensure stable starting conditions, and again heated to 210 °C. For each experiment, the recorded heat flow was normalized by sample mass.

Dilatometry

To examine the influence of various processing conditions on the solidification process of the different materials, dilatometry experiments were performed with the Pirouette pVT$\dot{T}-\dot{\gamma}$ apparatus (IME technologies, the Netherlands) [77, 137]. It allows investigation of the evolution of specific volume of polymers as a function of temperature, pressure, cooling rate and shear rate by measuring the volume change of a sample. A schematic overview of the most important components is shown in Figure 4.1.

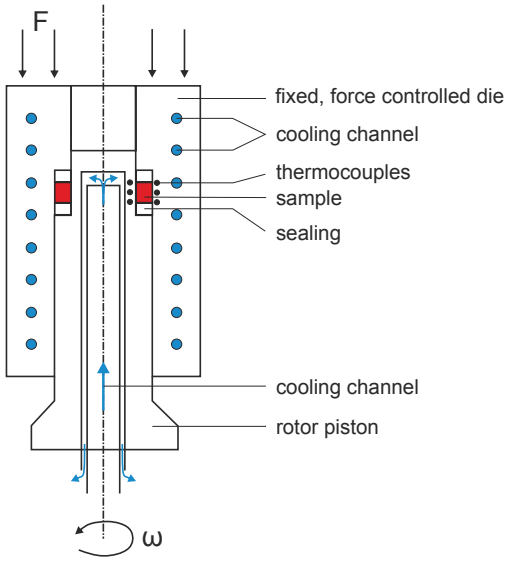

Figure 4.1: Working principle of the Pirouette.

The apparatus requires ring-shaped samples with a mass of ∼75 mg, an outer diameter of 20 mm, thickness of 0.5 mm and height of approximately 2.5 mm, which were pre-produced from granular material using a Babyplast injection molding machine (Rambaldi, Italy) equipped with a custom build mould. All experiments were performed in isobaric cooling mode at a pressure of 100 bar. The sample was heated to 220 °C and kept at that temperature for 10 minutes to erase all thermal history. Finally, the piston and die were cooled by either natural convection or a constant flux of air or water, which resulted in initial cooling rates of about 0.1, 1.0 and 90 °C/s, respectively. Cooling rates were determined as the temperature gradient between 195 and 130 °C. Experiments with flow were carried out during air cooling for different shear rates (3, 10, 30, 60, 100 and 180 1/s), at a constant shear time of 1 s at set shear temperature of 138 °C. Directly after the experimental run, samples were removed from the apparatus and stored in a freezer at -18 °C for later structural analysis.

Transmission electron microscopy

Samples for transmission electron microscopy (TEM) were trimmed from processed dilatometry samples parallel to the shear direction at low temperature (-120 °C) using a Diatome trimming tool. Subsequently, samples were stained for 24 hours with a RuO_4 solution prepared according to Montezinos et al. [139]. Ultrathin sections (70 nm) were obtained at -100 °C using a Leica S/FCS microtome equipped with a Diatome 35° knife. The sections were put on a 200 mesh copper grid with a carbon support layer and examined in a Tecnai 20 transmission electron microscope, operated at 200 kV.

Mechanical characterization

Mechanical properties were investigated by uniaxial tensile experiments in general accordance with ISO 527 using a Zwick Z010 universal tensile tester, equipped with a 100 N load cell and at a strain rate of 10^{-3} 1/s. Two dogbone shaped, 0.5 mm thick samples were cut from each PVT-sample in order to execute all experiments in duplo, other dimensions of the specimen are given in Figure 4.2. Before starting the actual experiment, a pre-load of 0.2

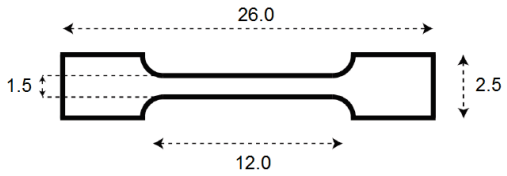

Figure 4.2: Dimensions of tensile bars in mm.

MPa was applied at 1 mm/min. All experiments were performed at room temperature (23 °C) and two weeks after sample removal from the freezer to prevent any influence of physical ageing. From the tensile test, both yield stress, σ_y, and strain hardening modulus, G, were determined as macroscopic phenomena from which to characterize the influence of flow on the final mechanical properties of the sample. Here, σ_y is determined from the tensile curves using the secant method as described by Ward [140], and G from the slope of the true stress versus neo-Hookean strain measure at relatively large deformation. In the case of (pre-yield) brittle failure, the strain hardening modulus could not be determined. Impact and flexural (3-point bending) testing was performed using 80x10x4 mm test bars, injection moulded in line with EN ISO 1873-2 (melt temperature 200 °C, mould temperature 40 °C). A 3-point flexural test according to ISO 178 (+23 °C) and Charpy notched impact test according to ISO 179 1eA (+23 °C and -20 °C) was performed in line with general industrial practice. Also, the melt flow rate (MFR) was measured according to ISO 1133 (230 °C, 2.16 kg load).

4.3 Results

The effect of processing conditions on the final morphology and mechanical properties of the three materials was investigated. First, the melting and crystallization behavior was characterized using DSC and using extended-dilatometry at different cooling rates. The influence of flow was investigated by imposing a one second shear pulse at a constant temperature and different shear rates during intermediate cooling. The final morphology was visualized using TEM for samples processed at three selected shear rates. Finally, mechanical properties were examined as a function of shear using tensile tests.

4.3.1 Melting and crystallization behaviour

The effect of material composition on melting/crystallization behavior of the materials was evaluated. The data recorded during the second heating and first cooling run are shown in Figure 4.3. For all materials, a clear melting peak of the EP matrix is recognized at 165 °C. In addition, a small endotherm is seen at 120 °C, which can be attributed to the small amount of PE present in the material. For the EP/EPR/HDPE, this peak partially overlaps with melting of the HDPE content, with the peak maximum observed at 131 °C; it can be clearly observed as a shoulder on the HDPE melting peak. Regarding the compound with added EOC, a broad melting peak is found around 60 °C, which is typical for ethylene copolymers with higher amounts of longer α-olefins as comonomer [53]. On cooling, data shown in Fig. 4.3b, all materials show one clear crystallization peak, which indicates that, for the current thermal conditions, crystallization of the matrix components occurs at similar temperatures (124, 119 and 120 °C). Small exotherms are observed at approximately 100 and 45 °C due to crystallization of the polyethylene fraction and the EOC modifier, respectively. No crystallization peak of the HDPE modifier can be distinguished separately from the matrix peak since the crystallization temperatures of these components overlap [141].

The effect of thermal history was further investigated in terms of (specific) volume rather than in terms of heat flow. These are the base results to compare with when studying the influence of flow. Moreover, by comparing to DSC results we show that the dilatometer results are consistent.
Dilatometry experiments were performed at three different cooling rates, all at an isobaric pressure of 100 bar. By measuring the expansion or shrinkage of the sample, the specific volume, v, can be plotted as function of temperature, see Figure 4.4. Three different regions can be identified during cooling; the melt, crystallization and solid regime, from high to low temperature, respectively. The presence of the ethylene-based content in the base material is recognized throughout the entire dataset by the lower specific volume of both compounds. The crystallization temperature, T_c, is determined halfway between the melt and solid stage regime and presented for all materials and conditions in Table 4.1. The dilatometer results

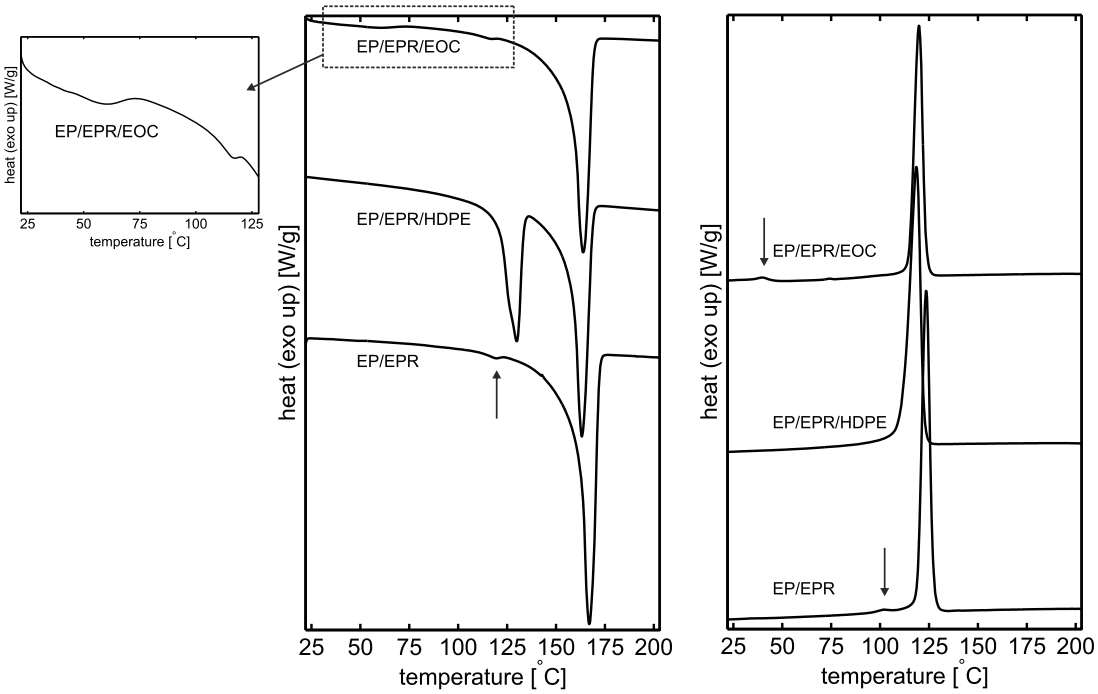

Figure 4.3: DSC traces of second heating with zoomed in detail of the low temperature region for EP/EPR/EOC (left) and first cooling (right) for all materials investigated. Cooling rate investigated is 10 °C/min (0.17 °C/sec)

for the lowest cooling rate (0.1 °C/s) are consistent with those found with DSC (0.17 °C). With cooling rate, the crystallization regime spreads out over a larger temperature window, and, consequently, T_c decreases. Due to the higher cooling rate, the process of nucleation and crystal growth is shifted towards a lower temperature, a common observation in non-isothermal crystallization studies [142]. For the two lowest cooling rates, the components of the different materials show, in agreement with the results from DSC, only one pronounced crystallization region. Here, crystallization of the PE content is not or only very weakly observed in terms of dilation. At the highest (initial) cooling rate of 90 °C/s, minor signs of a second crystallization process can be observed around 80 °C, which can be attributed to the polyethylene content of the EP/EPR and EP/EPR/HDPE material, Figure 4.4a and b, respectively. Crystallization of PE in the EP/EPR/EOC compound could not be detected for this cooling rate.

Table 4.1: Crystallization temperatures from dilatometry and DSC at different (initial) cooling rates.

	EP/EPR	EP/EPR/HDPE	EP/EPR/EOC
0.1 [°C/s]	123.8	121.7	125.0
1.0 [°C/s]	116.5	117.0	118.2
90.0 [°C/s]	97.5	101.2	101.5
0.17 [°C/s] (DSC)	123.5	118.5	119.9

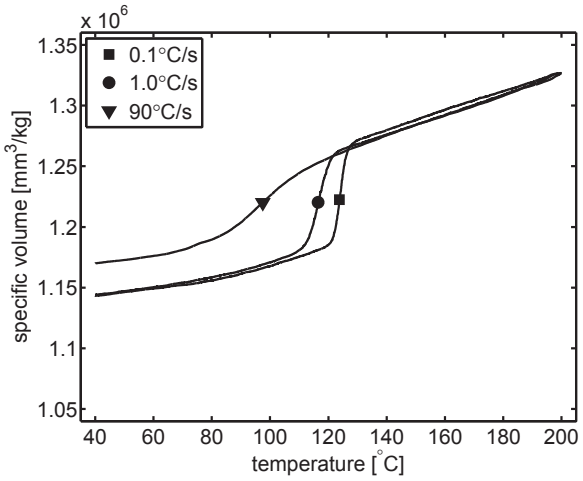

(a)

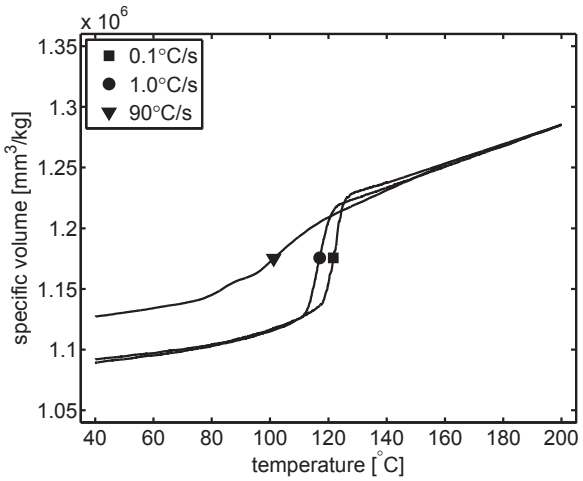

(b)

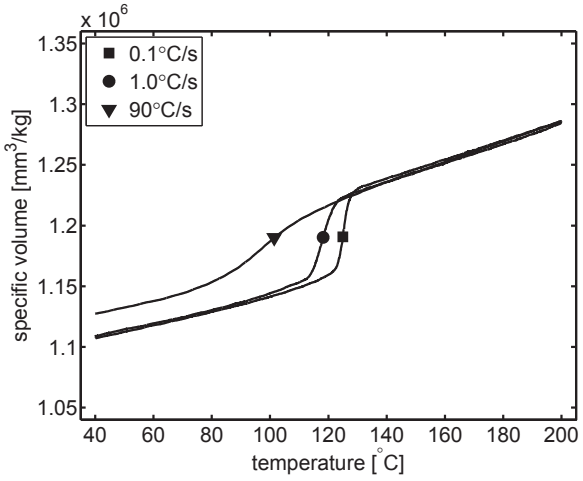

(c)

Figure 4.4: Effect of cooling rate on the specific volume evolution of the (a) EP/EPR copolymer, (b) EP/EPR/HDPE compound, and (c) the EP/EPR/EOC compound.

4.3.2 Effect of flow

Similar to the method explored by van Erp et al. [114], the influence of the thermomechanical history during cooling was investigated by applying flow as a step function of one second in a range of shear rates (3-180 1/s). Air was used for cooling (∼1 °C/s) to provide a narrow temperature window during the shear pulse. In this study, the shear temperature, $T_{\dot{\gamma}}$, was chosen equal for all materials and investigated at a fixed temperature of 30 °C below the pressure corrected melting temperature, $T_m(p)$, of the PP matrix. $T_{\dot{\gamma}}$ is defined as:

$$T_{\dot{\gamma}} = T_m(p_0) + \kappa\,(p - p_0) - \Delta T, \tag{4.1}$$

where κ is the pressure shift factor of 2.75 °C/100 bar, assumed similar to isotactic polypropylene [107], p_0 the atmospheric pressure in bar and ΔT the level of undercooling, set to 30 °C. Since the melting temperature was determined by DSC (10 °C/min) at 165 °C, $T_{\dot{\gamma}}$ was set at 138 °C. This level of undercooling was chosen such that get clear but not too strong effects of the flow applied. All experiments were performed at an elevated pressure of 100 bar. Dilatometry is a convenient way to study the influence of pressure on the crystallization kinetics. However, here we will focus on the effect of flow. To easily compare the influence of different thermomechanical histories on the crystallization process, rather than to focus on the absolute value of the specific volume, the raw data is converted in a normalized specific volume, ν^*, using:

$$\nu^* = \frac{\nu - \nu_s}{\nu_m - \nu_s}, \tag{4.2}$$

where ν is the measured specific volume, ν_s the specific volume in the solid state at 40 °C and ν_m the specific volume in the melt at 200 °C.

EP/EPR base material

The effect of flow on the evolution of the normalized specific volume is plotted for the EP/EPR in Figure 4.5. The influence of flow is clear; with increasing shear rate, the crystallization temperature increases with as much as 20 °C. As a result of the applied flow, the molecules are arranged in flow direction, decreasing the melt entropy, thus increasing the driving force for crystallization. Molecular orientation stimulates the formation of flow induced nuclei, which, depending on the conditions, can tremendously increase the rate of crystallization [6]. The difference between the quiescent case and the lowest shear rate (3 1/s) condition is hardly noticeable. At the highest shear rate (180 1/s), the crystallization temperature equals the shear temperature, which evidences a very high crystallization rate and formation of flow-induced structures [114]. Obviously, upon a further increase of the shear rate, the crystallization temperature can never exceed the shear temperature. Note the 'dip' in the data at the shear temperature of 138 °C, this is an experimental error due to the sudden movement of the rotor piston inside the Pirouette and is further ignored.

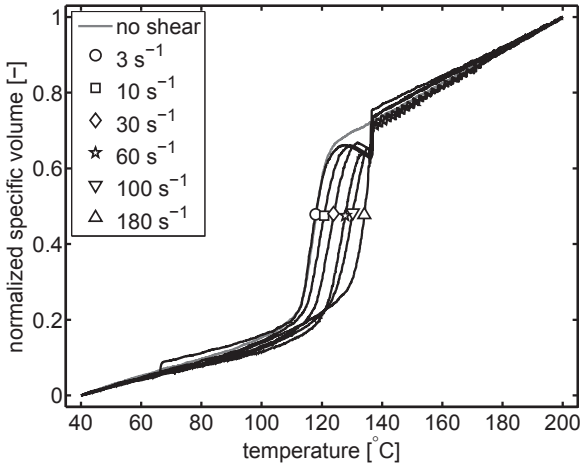

Figure 4.5: Effect of shear flow on the normalized specific volume evolution of EP/EPR.

The phase structure of heterophasic PP impact copolymers is determined by three main factors: the viscosity ratio between the matrix and elastomer, phase compatibility and the deformation history during processing [120, 122, 125, 141]. Since both the viscosity and phase compatibility are pre-determined factors by the choice of (compounded) material, the structure was studied as a function of the thermal and deformation history only, taking the sample crystallized in quiescent conditions as a reference state. Where earlier work on these materials focuses on the particle size distribution or the interaction between the different components [125, 141], we will focus only on the effect of flow on the final morphology and the mechanical properties thereof (next section).

To visualize the final morphology, detailed TEM pictures were taken on 70 nm thick coupes cut in the shear direction. Samples crystallized from the melt in quiescent conditions, with intermediate flow strength (30 1/s) and strong flow (180 1/s) were examined, see Figure 4.6. High- and low-detail pictures, representative for the entire sample, were selected for each condition. The matrix material shows a spherulitic PP structure in which amorphous EP regions are dispersed [143]. Inside the modifier, multiple crystalline PE inclusions are located, recognized by bright lamellae, designating the dispersed phase as a core-shell particle. It is known that with increasing ethylene content, the amorphous particles become larger and may possess several crystalline inclusions, also known as salami-particles [144, 145]. Here, the amount of ethylene is sufficient to form a number of inclusions in each EPR domain. Upon intermediate flow conditions, flow-enhanced features can be observed such as a number of lamellae that have grown perpendicular to the direction of flow (kebabs). Meanwhile, the modifier content remains unoriented. A stretched EPR particle can be considered as a deformed and confined viscoelastic droplet, which may relax to a spherical particle, depending on the ratio between interfacial forces and viscosities [146]. If the relaxation process is slow, the particle remains stretched on solidification, alternatively, it relaxes back to the original shape. The exact parameters for this relaxation process are not known for this system. However, we have explored a sufficiently large range of shear rates to cover the full range of deformed EPR particles. The effect of strong flow conditions, displayed in the bottom half of Figure 4.6, is best noticed through the particle anisotropy. The matrix material also shows an increased level of orientation, which can be deduced from the alternating light and dark bands found perpendicular to the direction of flow. Inside the EPR shell, the PE inclusions remain unoriented and still appear in the spherulitic confirmation. Due to the high $T_{\dot{\gamma}}$ with respect to the melting point of PE, the PP matrix orients upon flow and crystallizes ahead of the small percentage of ethylene within the EPR regions.

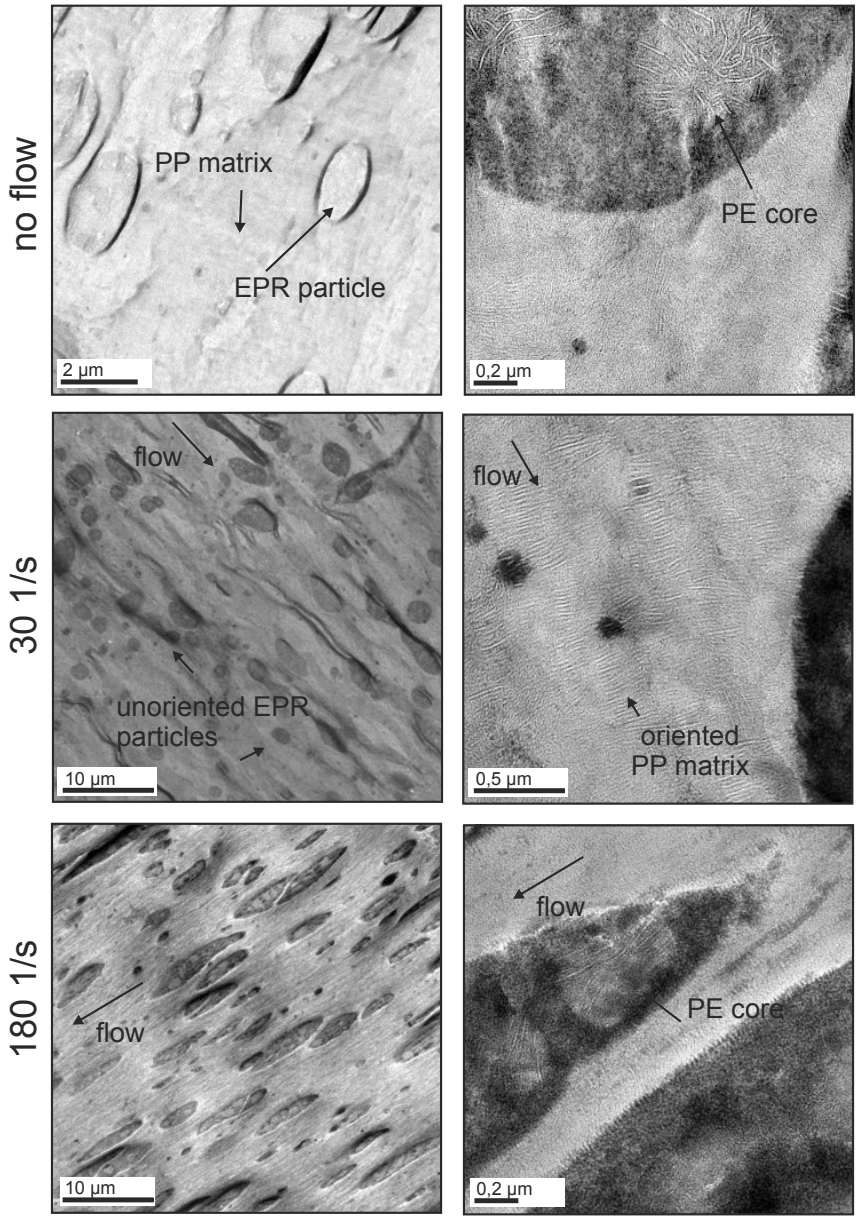

Figure 4.6: TEM micrographs of the morphology after solidification without flow (top), with intermediate flow (middle) and strong flow (bottom) of the EP/EPR material in low detail (left column) and high detail (right column). PE inclusions are recognized inside the modifier. With flow, oriented lamellae are formed in the matrix perpendicular to flow direction. After strong flow, the modifier remains slightly stretched in the oriented matrix.

EP/EPR/HDPE compound

The same experimental protocol was applied for the EP/EPR/HDPE compound. Upon low shear conditions, the results in Figure 4.7 are similar to those in Figure 4.5; flow only increases the crystallization temperature with a few degrees. However, upon strong flow conditions, e.g. 60 1/s and above, crystallization is completed in a two step process. Here, the first crystallization process starts during or directly after the shear pulse and is completed at a temperature of approximately 130 °C. It is not before the end of the second crystallization process, which sets in around 120 °C, that space filling is complete and ν^* overlaps the solid regime data of the unsheared sample.

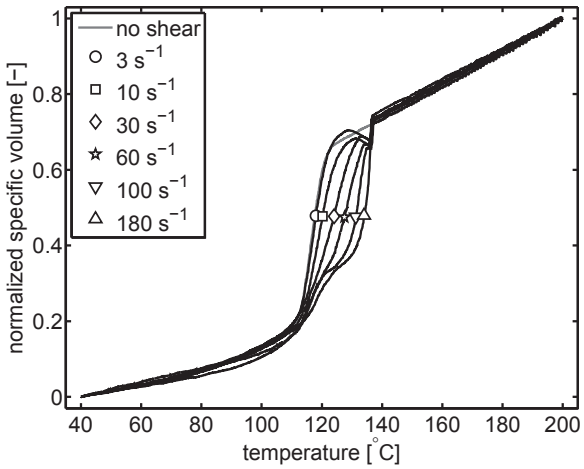

Figure 4.7: Effect of shear flow on the normalized specific volume evolution of the EP/EPR/HDPE compound.

Since the material investigated is a multi-component system, each component having different crystallization kinetics, the multiple volume fractions will crystallize at different temperatures. In the absence of flow and for the lowest shear rates, crystallization of the matrix component overlaps with crystallization of the HDPE component, as observed in DSC and dilatometry, Figures 4.3 and 4.4b, respectively. For higher shear rates, the first process at higher shear rates is attributed to flow-induced crystallization of the matrix material. Since $T_{\dot{\gamma}}$ is well above the melting temperature of HDPE, it is assumed the relaxation times of this component are relatively short and the molecules are able to relax after flow. Still, crystallization of the HDPE component is slightly enhanced with flow, i.e. the second process shifts towards higher temperatures. It is expected that the heavily oriented PP matrix acts as a nucleating surface for the crystals formed by the HDPE, a detail which could be extracted from the TEM pictures in Figure 4.8.

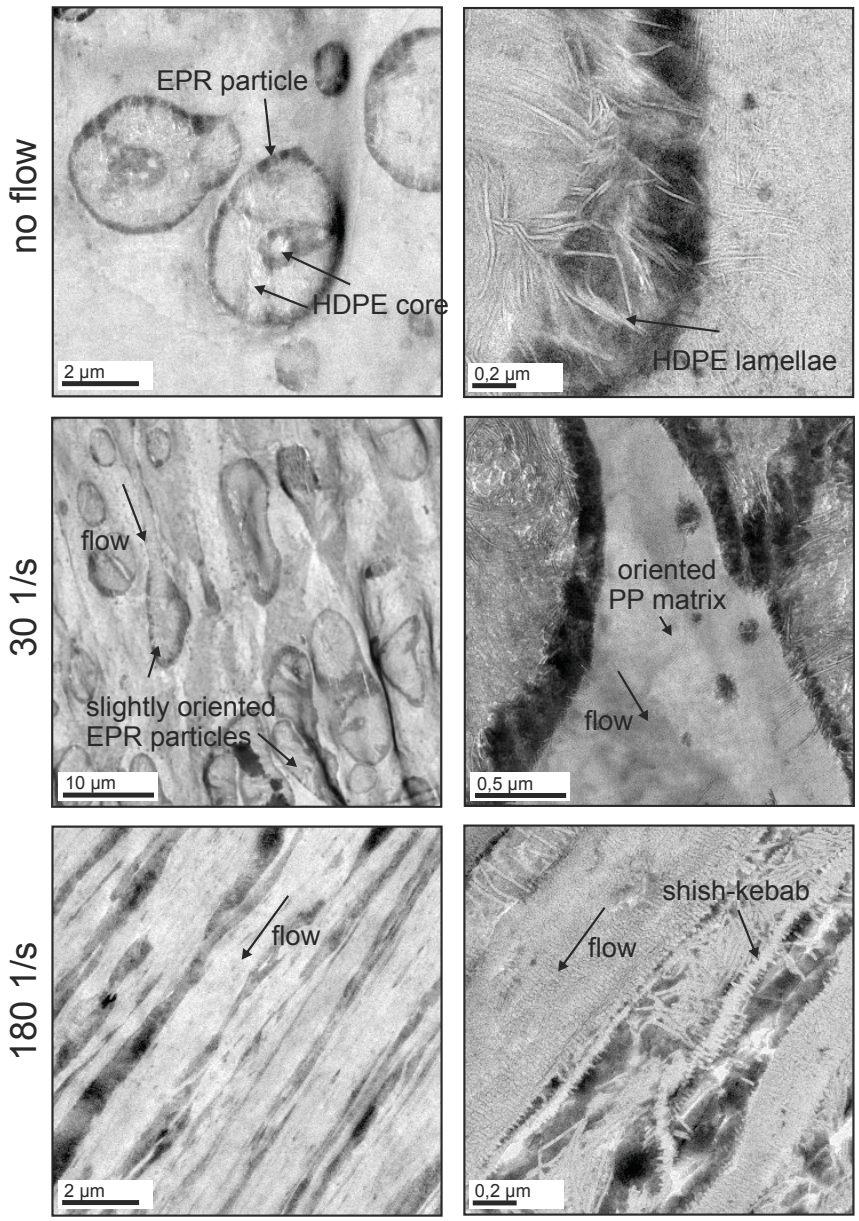

Figure 4.8: TEM micrographs of the morphology after solidification without flow (top), with intermediate flow (middle) and strong flow (bottom) of the EP/EPR/HDPE material in low detail (left column) and high detail (right column). PE lamellae are recognized at the modifier boundary. With medium flow, oriented lamellae are formed in the matrix perpendicular to flow direction, while the modifier particles remain unoriented. After strong flow conditions, the matrix and modifier are fully oriented and shish-kebab structures can be observed from the matrix.

The morphology of the unsheared sample shows EPR shells that contain a (high-density) polyethylene core, which itself, in some cases, contains an amorphous section with again an ethylene core. The HDPE (and ethylene from the base material, it is not possible to distinguish between the two) form distinct lamellae, which are situated mostly within the amorphous regions. A significant number of lamellae have grown from the matrix inside the shell or vice versa, and are expected to increase the adhesion level between matrix and modifier particle. Opposite to the TEM pictures of EP/EPR, a small number of thick PE lamellae can also be recognized within the PP matrix as a result of the partial miscibility of the components [125]. At intermediate flow conditions, TEM reveals a slightly oriented matrix and modifier content. After flow, most rubber inclusions are not able to relax, most probably due to the high adherence level, or compatibility, between matrix and particle with HDPE content [125, 129, 141]. Most intriguing is the morphology of the strongly sheared samples; heavily oriented features were obtained, where the EPR particles are stretched throughout the matrix. The HDPE content is still recognized as the most light regions, mainly located at the edge of the amorphous zones. When examined in high detail, shish-kebab structures can be seen clearly in the matrix section. Any misalignment of the shish with the flow direction is expected to be caused by preparation of the fragile ultra-thin sample coupes. The HDPE fractions are always located inside the EPR particles and, most importantly, found adjacent to the PP shish-kebabs, which provide the HDPE lamellae with a suitable growth surface, assumed responsible for the somewhat higher crystallization temperature in dilatometry measurements, Figure 4.4b. This is compatible with results for iPP/PE blends, where the PE fraction was found to epitaxially crystallize on an oriented crystalline iPP interface, which generated an increased number of nuclei [147–149].

EP/EPR/EOC compound

Finally, the EP/EPR/EOC compound is investigated for varying thermomechanical histories. From the results presented in Figure 4.9, it is clear that, once more, crystallization of the matrix component is severely enhanced with flow. For the two highest shear rates, nearly identical crystallization kinetics are observed. Here, the strength of flow is such that, already at 100 1/s, crystallization starts during the shear pulse and the shift of T_c reaches it's maximum. With increasing shear rate, a small shoulder in the specific volume evolution is present around 110 °C as a result of the fraction crystallizing at these low temperatures only. Due to data overlap at low temperatures, it is hard to distinguish between the different curves and a more detailed picture of the 90-130 °C temperature window is presented in Figure 4.9b. From the DSC data (taking into account a shift of ∼3 °C in T_c due to the pressure difference) it is evident that this shoulder concerns crystallization of the polyethylene content within the base material. The EOC will crystallize at a later stage, i.e. at a much lower temperature of ∼60 °C.

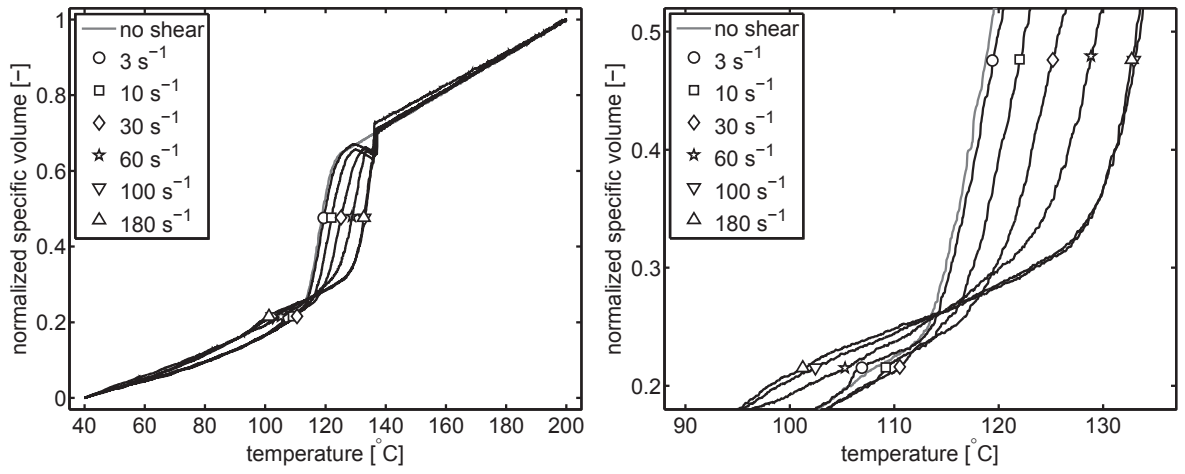

Figure 4.9: Effect of shear flow on the normalized specific volume evolution of the EP/EPR/EOC blend (a) and a zoom-in on the temperature region of the second crystallization process.

For the 100 and 180 1/s shear rate, and to a smaller extend for 60 1/s, a higher specific volume is obtained after crystallization of the matrix and, subsequently, the shoulder is shifted to temperatures around 100 °C. From the dilatometry data alone, it is difficult to explain this phenomena. Therefore, we first investigate the morphology as visualized by TEM, Figure 4.10.

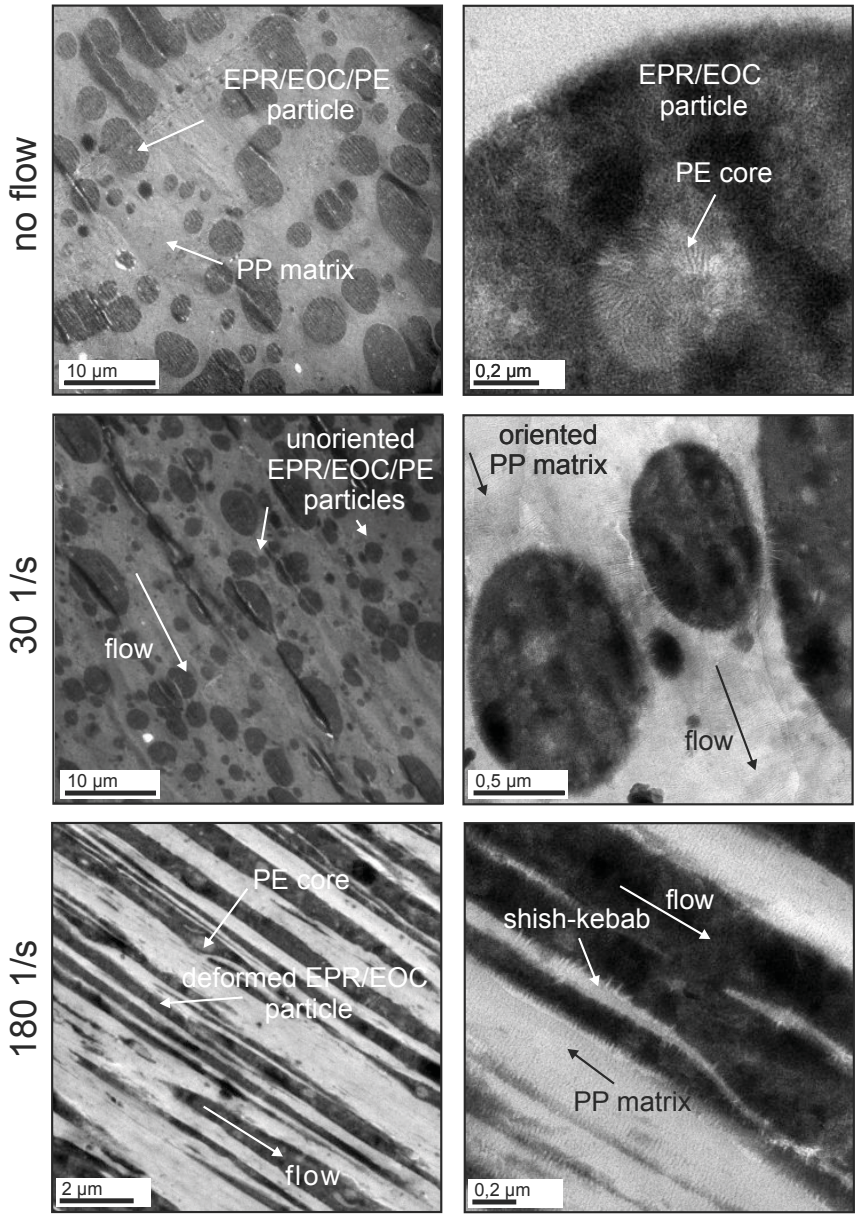

Figure 4.10: TEM micrographs of the morphology after solidification without flow (top), with intermediate flow (middle) and strong flow (bottom) of the EP/EPR/EOC material in low detail (left column) and high detail (right column). PE inclusions are found in the modifier, in which the EOC content is dissolved. With medium flow, oriented lamellae are formed, while at first, the modifier particles remain unoriented. After strong flow conditions, the matrix and modifier are fully oriented and shish-kebab structures can be observed from the matrix.

In contrast to EP/EPR/HDPE, see Figure 4.8, the EOC compound does not form visible crystalline lamellae within the particles. In fact, it is not possible to recognize the EOC in the TEM micrographs. A large part of the EOC content is dissolved in the amorphous regions, enabled by the partial miscibility between both components [125, 141]. Moreover, upon high concentrations of (long-chain) branching content, literature reports on EOC to 'order' in so-called fringed-micellae or bundle-like structures [53, 59] which are hard to distinguish using TEM. The lamellae that are visible in the high-detail picture of the unsheared sample, originate from the ethylene content in the base material, see also Figure 4.6. Similar to the other materials investigated, the intermediate shear rate only induces an oriented matrix and does not or only weakly affect the filler particles. The influence of EOC content on the morphology displayed in the bottom of Figure 4.10 is severe, especially when the sheared base material is taken as a reference (Figure 4.6). TEM reveals heavily deformed EPR/EOC particles among with the embedded crystalline PE. In high-detail, flow-induced PP structures are found in the matrix amidst the amorphous regions. Although we cannot draw any strong conclusions regarding the shift of the shoulder found with dilatometry, it is expected that (flow-induced) crystallization of the matrix and ethylene content are suppressed by the long-chain branched EOC which is partly dissolved in the EPR particles and acts as tie-chains. With flow, the EOC content will be distributed throughout the matrix; with an increase of topological constraints (knots, ties) collecting suitable crystallizing chain sequences to the crystal front (or rejecting branches from crystals) is slowed down [150], hence, crystallization, an increase of the overall density, is measured at a lower temperature.

4.3.3 Mechanical properties

For each of the three heterophasic copolymers investigated, the components and the final morphology play a decisive role during deformation. Extensive work in this field has been performed by Bucknall [151] and by Kim and Michler et al. [144, 152, 153], of whom the latter categorized a number of micro-mechanical deformation mechanisms for a range of filled polymer compounds using combined electron microscopy and in-situ tensile testing. In general, a three-stage mechanism is present for particle filled semi-crystalline systems:

- *1. Stress concentration of the modifier* - Due to the different elastic properties, the particles act as stress concentrators, which leads to the development of a tri-axial stress inside these particles.
- *2. Void and shear band formation* - Build up of high stress concentrations induces void formation through cavitation inside the particles or due to debonding at the particle matrix interface. At the same time, weak shear bands are formed between the voids.
- *3. Induced shear yielding* - After cavitation or debonding, stress is locally released into the matrix, increasing the shear component and inducing shear yielding.

A standard characterization of the different materials used was performed. Table 4.2 summarizes the mechanical performance of materials as tested under standard impact and bending conditions. The HDPE addition results only in a limited stiffness reduction, with positive impact strength effects at ambient and sub-zero temperatures. In contrast, the EOC addition reduces the stiffness significantly while boosting impact strength much more. This is in line with modification results achieved for single-phase PP grades [141].

Table 4.2: Standard characterization results of the investigated materials.

Composition			EP/EPR	EP/EPR/HDPE	EP/EPR/EOC
MFR ISO 1133	230°C/2.16 kg	[g/10min]	8	8	8
Flexural ISO 178	Modulus	[MPa]	1303	1267	998
	Flex. Strength	[MPa]	34.4	32.3	25.8
	Flex. Strain	[%]	6.5	6.6	6.5
Charpy ISO 179	1eA+23°C	[kJ/m^2]	8.7	12.31	54.5
	1eA-20°C	[kJ/m^2]	3.95	4.48	7.4

The mechanical behaviour during homogeneous deformation, the intrinsic stress strain response, can be measured by means of uniaxial compression tests. However, for the samples obtained from dilatometry (see previous section) such experiments are not feasible. Therefore, macroscopic phenomena such as yield stress and strain hardening were determined as function of flow strength using tensile testing. From each ring-shaped dilatometry sample, two dogbone shaped specimen were cut. Since we do not see plastic localization during our experiments, we can interpret our data to analyse the strain hardening modulus. The stress-strain response of all three materials is plotted in Figure 4.11

as true stress versus the neo-Hookean strain measure, $\lambda^2 - \lambda^{-1}$, to emphasize the effect of flow on strain hardening. Measurements on both specimen taken at equal flow conditions show, in most cases, good agreement. The highest stress levels during deformation were recorded for the EP/EPR base material. With the addition of HDPE, the stress level is slightly reduced, whereas it drops significantly for the material with EOC content, which is in agreement with the results obtained from the bending tests, see Table 4.2.

The mechanical response of the EP/EPR material in Figure 4.11a shows only a slight increase of the (yield) stress level with shear, which corresponds to the low sensitivity for flow on morphology development as observed with TEM, see Figure 4.6. Regarding the two compounded materials, see Figure 4.11b and c, a small increase in stress was measured for the lower range of shear rates, e.g. up to 60 1/s. For higher shear rate values, an increase of both the yield stress, σ_y, and strain hardening modulus, G, was measured. This is in line with earlier work on PE and polyethylene teraphtalate (PET) by Schrauwen et al. [154] who showed that both σ_y and G are significantly affected by the level of molecular orientation present in the material as function of the processing conditions. For the materials under investigation, we can deduce that below 60 1/s, no significant level of orientation is present. Indeed, only a partially oriented matrix component was observed for samples sheared at 30 1/s, see Figure 4.8 and 4.10. Upon a further increase of the shear rate, enhanced orientation of the matrix occurs and, ultimately, the flow strength is sufficient to also form oriented EPR inclusions, which results in an additional increase of both σ_y and G.

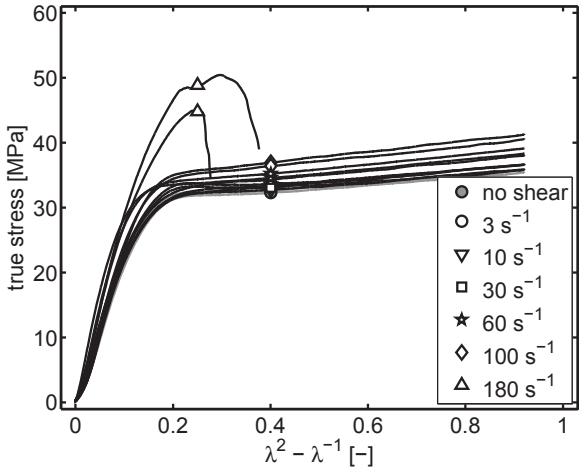

(a)

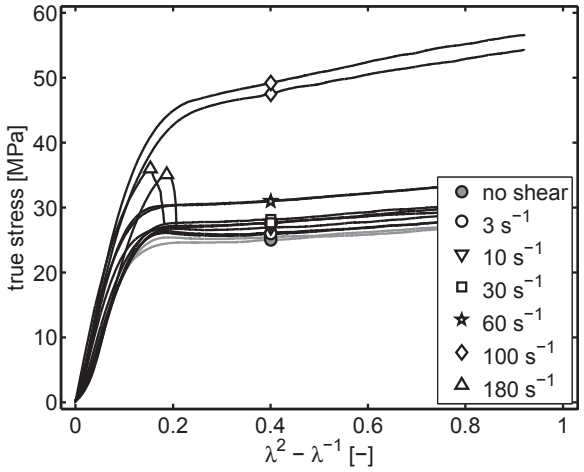

(b)

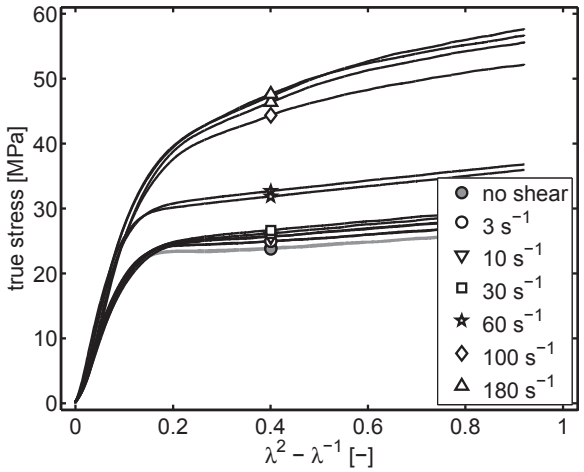

(c)

Figure 4.11: True stress vs strain for (a) EP/EPR, (b) EP/EPR/HDPE, and (c) EP/EPR/EOC. Markers represent the different level of shear flow during processing.

The different crystallization regimes can be recognized for all materials when the yield stress and strain hardening modulus is plotted versus shear rate, see Figure 4.12. Van Meerveld et al. [108], described different crystallization regimes as function of the Weissenberg number, Wi, with $\mathrm{Wi} = \lambda\dot{\gamma}$ and λ a characteristic relaxation time, as a measure for the strength of flow. Since here, it is not possible to define a characteristic relaxation time for the complex material composition we are studying, we use the shear rate as a measure for the flow strength. We can link the constant yield stress at low shear rates to either no influence of flow, or to a flow enhanced nucleation process within the matrix component. The molecular chains are sufficiently stretched and oriented creating extra nuclei, while the growth rate and growth-mechanism remain unaffected. As a consequence of the higher T_c caused by flow, slightly thicker lamellae are formed which should attribute to the gradual increase of the yield stress [155]. In this case, the difference in T_c is insufficient to increase σ_y. At higher Wi numbers, high amounts of shear induced nuclei are generated and oriented crystalline structures are formed, effectively increasing σ_y and G. Using X-ray analysis, van Erp et al. [114] confirmed that in the first two regimes, no significant amount of molecular orientation is present, while for the final regime, highly oriented patterns can be observed typical for shish-kebab structures. Notice that the three crystallization regimes plotted in Figure 4.12 correspond to (I) no influence of flow or point-like nucleation, (II) flow-induced nucleation in the matrix and (III) flow-induced crystallization of the matrix (shish-kebab formation), including orientation and flow induced nucleation and oriented crystals in the rubber inclusions, respectively. Both compounded materials show a higher slope in all regions in Figure 4.12a, evident for the large influence of flow compared the EP/EPR base material.

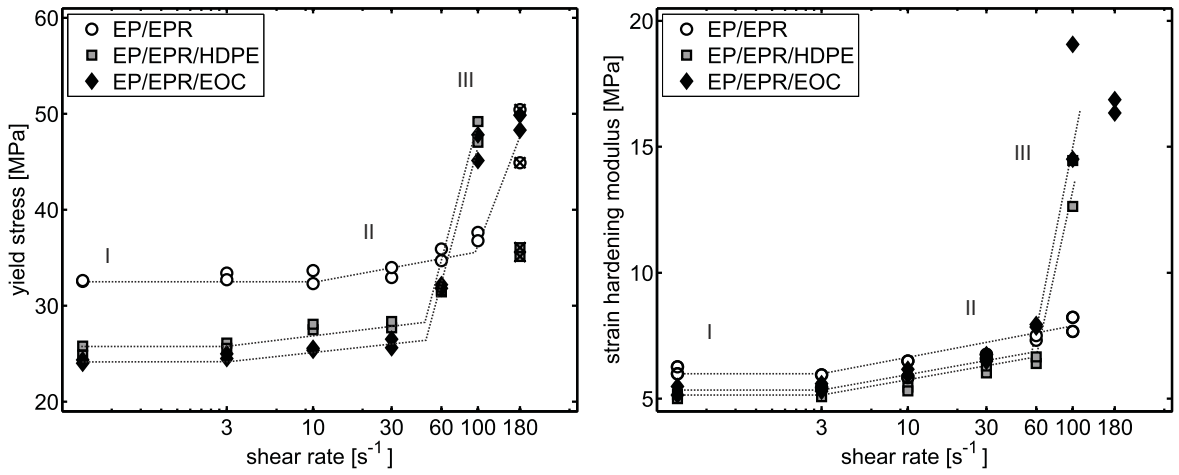

Figure 4.12: Effect of shear flow on (a) the yield stress and (b) strain hardening modulus for the different materials and crystallization regimes: (I) no influence of flow or point like nucleation, (II) flow induced matrix and (III) formation of flow induced structures including oriented particles. Markers with 'x' represent brittle failure.

For the EP/EPR/EOC compound σ_y is nearly equal for the two highest shear rates. This can be understood from the crystallization kinetics during and after flow which is the same, see Figure 4.9. Both the EP/EPR and EP/EPR/HDPE material show brittle failure for the maximum shear rate conditions. Careful observation of the deformed specimen shows that all samples failed ductile were non-transparent due to stress whitening caused by void formation. The samples obtained from the highest shear rate do not show stress-whitening. Due to the high level of orientation of the matrix and the severe deformation of the modifier content, the toughening effect of the particles is not effective any more, leading to embrittlement of the material and the absence of growing voids.

4.4 Conclusion

In the present study, samples of three different heterophasic polypropylene copolymer compositions were processed under well-controlled conditions and investigated for differences in final morphology and mechanical properties. It has been shown that for quiescent cooling conditions, crystallization of the individual material components will occur at well separated temperatures. For conditions involving flow, however, crystallization of the components may hinder or promote each other. Depending on the flow strength, here defined as the shear rate, multiple types of morphology can be formed; the material can either remain unoriented, contain an oriented matrix component with shish-kebab structures, or become fully oriented including deformed modifier particles. The different morphology types are clearly represented in the mechanical properties, i.e. yield stress and strain hardening modulus. Regarding the final morphology and mechanical properties of the samples, both compounded materials with HDPE and EOC were most sensitive for flow. The highest flow strength investigated resulted in a high orientation of both the matrix and modifier content, with the inability of growing voids inducing brittle failure. These results clearly show the importance of the processing step for final product properties which for multi-phase materials is at least as high as for single-phase homopolymers.

Chapter 5

Structure development of low-density polyethylenes during film blowing: A real time wide-angle X-ray diffraction study

Reproduced from: Martin van Drongelen, Dario Cavallo, Luigi Balzano, Giuseppe Portale, Iakovos Vittorias, Wim Bras, Giancarlo Alfonso and Gerrit Peters, *Macromolecular Materials and Engineering*, 299:1494-1512, 2014

Abstract

We studied experimentally the structure development, i.e. crystallinity and orientation, during film blowing for three different low-density polyethylene grades and a combination of low and high levels of take-up and blow-up ratios. For this, we combined blown film extrusion with in-situ X-ray diffraction at a synchrotron radiation beamline. The measurements of the three different grades were performed at rheological similar conditions at the die exit, i.e. at nearly the same Weissenberg number (Wi), with each grade possessing different molecular properties in terms of molecular weight distribution and long and small chain branching content. The development of crystallinity and molecular orientation was determined as function of the distance from the die. It is shown that the combined approach of wide-angle X-ray acquisition with blown film extrusion is a valuable method to study structure evolution in the complex process of film blowing. Therefore, this method can provide data from which polymer structuring in industrial conditions can be understood and controlled and, moreover, which can be used to validate results from numerical models for film blowing and help to improve and/or extend these models.

5.1 Introduction

The blown film extrusion process is extensively used in the packaging industry to make large volumes of polymer films. Because of the large, worldwide demand for these kinds of products, the manufacturing speed is high and, consequently, shaping the product involves high deformation rates and steep thermal gradients. Due to the considerable amount of research dedicated to polymer processing in the last few decades, it has become well known that the conditions applied during the production process, together with the molecular features of the polymer resin, determine the final microstructure, i.e. the crystalline and amorphous morphology and orientation thereof [6,156–160] and, thus, the final mechanical, optical and barrier properties [154,161,162]. However, the coupled relations between these quantities are often complex and rather difficult to seperate.

Some of the most common materials used in film blowing are high- and low-density polyethylenes, HDPE and LDPE, respectively. For these ethylene-based polymers, depending on the material and the processing conditions, different structures of organized lamellae are formed during crystallization [163–165]. In the absence of flow, spherulitic structures are formed by lamellae that grow in radial direction, with the growth rate being a function of temperature and pressure. As a result of stretching of the melt, row nucleated or fibrillar (shish-kebab) structures may develop. The radial growing lamellae are either twisted at low stress levels or straight at higher stress levels [166]. During film blowing, the conformation of the molecules is strongly affected by biaxial stretching. Typically, the final film consists of a mixture of the lamellar structures mentioned. In the machine direction, defined as the production direction, e.g. from the die towards the niprolls, the stretch is defined by the ratio between the pick-up speed of the niprolls and the average feeding speed at the die (defining the take-up ratio, the TUR), in the cross-machine direction the stretch is defined by the bubble inflation, i.e. the ratio between the final bubble diameter and the die diameter (defining the blow-up ratio, the BUR) [164, 167].

The morphology of the blown film has been extensively studied by means of different experimental methods, such as for instance differential scanning calorimetry (DSC) [161], scanning/transmission electronic microscopy (SEM/TEM) [168], birefringence [169] or X-ray scattering techniques [161, 170]. However, these measurements were carried out *post mortem*. They can be used to modify the process by trial and error, which can be expensive and time consuming since experiments need to be repeated several times before optimal processing conditions are found. Therefore, a systematic study of the morphology development, i.e. the crystallization kinetics along the film line, which can be achieved by using accurate on-line methods, is considered to be of great importance for a better understanding of the production processes and will ultimately lead to improving and fine-tuning of the film properties. There are a number of models that describe the film blowing process [171–176], of which the most detailed ones are published recently. The experimental results we obtained can be used to validate or improve/extend such models.

In film blowing lines in industry, online measurements of the film quality are established by means of optical quality check in order to locate surface defects such as shark-skin or to detect the occurrence of melt fracture. On a smaller scale, several researchers report on real-time measurements combined with different methods such as SALS [177], Raman spectroscopy [178] or birefringence [168, 179]. Among various characterization methods, X-ray diffraction techniques such as small-angle X-ray scattering (SAXS) or wide-angle X-ray diffraction (WAXD), provides for a direct measurement technique to obtain the crystallinity and molecular orientation within a sample. For practical reasons, on-line structure analysis using X-ray based methods was still reserved for lab-scale environments [180, 181]. Combining a pilot-plant film blowing setup with X-ray leads to many impracticalities and limits the accessibility of the blown film line because of the presence of radiation sources. The experiments reported in this work were made possible by combining a medium scale film blowing setup with a synchrotron radiation beam line.

Due to the combination of a high X-ray flux and a high degree of collimation of the X-ray beam and an advanced detector, structure formation could be examined in-situ. In this way, a combination of different machine settings, relevant for processing conditions, could be explored within a short amount of time and with an accuracy beyond the capacity of laboratory sources [182]. The goal of the present study is to investigate the crystallinity and molecular orientation along the film line for different processing conditions and materials. Three different grades of LDPE are investigated for different blow-up ratios and take-up levels. For a better understanding of the structure evolution during processing in terms of the molecular properties, an extensive material characterization is provided by using oscillatory rheology and gel-permeation chromatography (GPC).

5.2 Materials and Methods

5.2.1 Materials

All tested samples are commercial low-density polyethylene (LDPE) grades from the Lupolen product family of LyondellBasell. These samples were selected because they allow for the investigation of the role of molecular features in the crystallization behavior under complex conditions. The LDPEs vary in molecular weight distribution (MWD), long-chain branching (LCB), thermal, and rheological properties.

5.2.2 Molecular characterization

The molecular weight distribution of the studied polymers was determined by gel-permeation chromatography, GPC, using a Polymer Laboratory PL 210, at 140 °C. A Wyatt DAWN EOS was used as detector to perform multi-angle-laser-light scattering (MALLS) measurements in order to determine the long-chain branching. Samples were dissolved in trichlorobenzene, TCB, (0.04 wt%) and eluted at 0.6 ml/min. For MALLS calibration, linear PS and PE standards were used.

5.2.3 Thermal characterization

Differential scanning calorimetry (DSC) was used to quantify the melting and quiescent crystallization behavior, using a DSC Q2000 apparatus (TA Instruments). The sample was heated with 20 °C/min from -10 to 200 °C and subsequently cooled with the same rate to -10 °C and again heated to 200 °C. The melting peak (of the 2nd heating run), T_m, the crystallization peak, T_c, and the onset of crystallization (temperature where heat-flow decreases below the base-line), $T_{c,onset}$, are determined using the TA Universal Analysis 2000 software.

5.2.4 Rheological Characterization

The granulate samples were compression-molded at 200 °C and at 200 bar for 4 minutes to approximately 1 mm thick plates, from which the samples were cut out. The rheological characterization was performed in an AntonPaar MCR301 rheometer. Dynamic oscillatory shear measurements were performed at three temperatures, 150, 190 and 210 °C. Curves were shifted to a mastercurve at T = 190 °C and the activation energy, E_a, was calculated. Elongational viscosity measurements were done at 150 °C using a mounted SER fixture [183] with strain rates 0.05, 0.1, 0.5, 1, 5, and 10 1/s.

5.2.5 Film blowing setup

A Collin Blown Film Unit type 180-400 and extruder were mounted on the X-ray beamline. A picture of the experimental hutch with the setup placed in position is shown in Figure 5.1. The used die diameter and die gap were 50 and 0.8 mm, respectively. The processing conditions used are given in Table 5.1. Since film blowing is a complex problem and we wanted to make the experiments as much as possible ”comparable” we tried to keep the most important conditions the same. This includes the throughput, the BUR and TUR values (i.e. the biaxial stationary stretched state) and, finally, the shear history of the materials before it leaves the die. For the latter we choose the Weissenberg number (the product of relaxation time and shear rate) to be similar for the different grades. Therefore, the extrusion temperature was set to 200 °C for all zones for the grade(s) with the high viscosity (grade 1 & 2) and to 180 °C for the low viscosity grade (grade 3), respectively. In this way the viscoelastic behavior at the exit of the die is similar for the three grades for similar other processing conditions. Die exit velocity has been calculated considering a melt density of 0.768 for grade 3 and 0.757 g/cm^3 for grade 1 and 2, respectively [184]. The processing

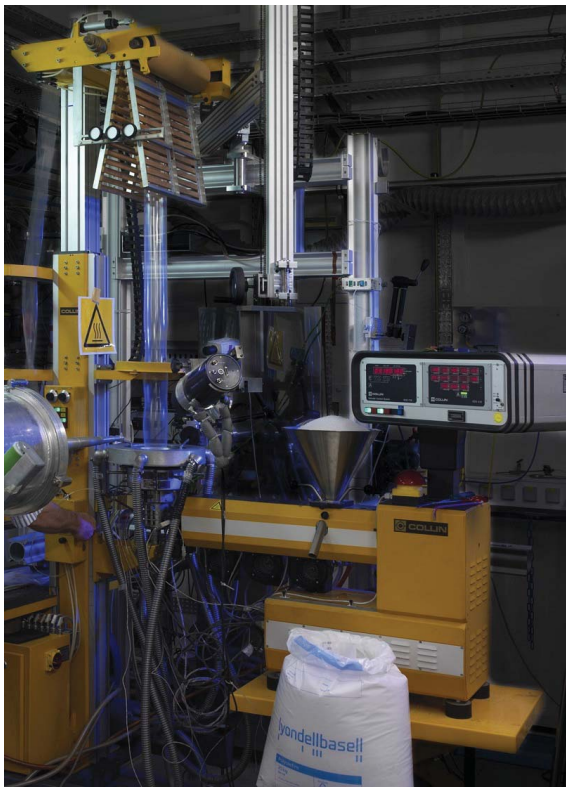

Figure 5.1: Blown film unit (left) and extruder (right) mounted at BM26B, DUBBLE@ESRF. (X-ray detector not yet into position).

conditions were tuned in order to approximate a similar set of blow-up ratios (BUR) and take-up ratios (TUR) for all grades. Take-up ratio is defined as the ratio of the take-up velocity (at the niprolls) with respect to the average speed at the die, while blow-up ratio is defined by the ratio of the final bubble diameter with respect to the diameter of the die.

Each material was blown in four different conditions following a combinatorial approach, i.e. for each of the two BUR values two TUR levels were employed.

Table 5.1: Processing conditions. Data in column marked by (*) is given only when available.

Experiment	Bubble diam. [mm]	Throughput [g/min]	Take-up vel. [m/min]	TUR [-]	BUR [-]	F-L height* [cm]	Film thick. [μm]
1-BURL-TURL	95	14.4	1.30	8.2	1.9	31.25	41
1-BURL-TURH	95	14.4	2.66	16.8	1.9		41
1-BURH-TURL	124	14.2	1.31	8.4	2.5	23.75	54
1-BURH-TURH	121	14.4	2.66	16.8	2.4		53
2-BURL-TURL	95	14.6	1.36	8.5	1.9	25.50	41
2-BURL-TURH	95	14.0	2.76	17.9	1.9		41
2-BURH-TURL	127	14.6	1.34	8.3	2.5	20.00	56
2-BURH-TURH	118	14.2	2.76	17.7	2.4		51
3-BURL-TURL	95	13.8	1.32	8.8	1.9	25.00	41
3-BURL-TURH	95	14.4	2.78	17.8	1.9		41
3-BURH-TURL	131	13.8	1.32	8.8	2.6	17.00	57
3-BURH-TURH	131	14.2	2.76	18.0	2.6		57

5.2.6 Particle tracing

To identify the velocity of the film at a certain distance from the die, and the time to reach that position, movies of the bubble were collected for each processing condition by means of a CCD camera and analyzed using the Kinovea® software package. For that purpose, pieces of black tape were placed on the film surface as a marker and tracked as a function of time. As an example, some movie frames are shown in Figure 5.2. Due to a slight misalignment of the die, an asymmetry is observed in the bubble shape. The position of the tracker given by

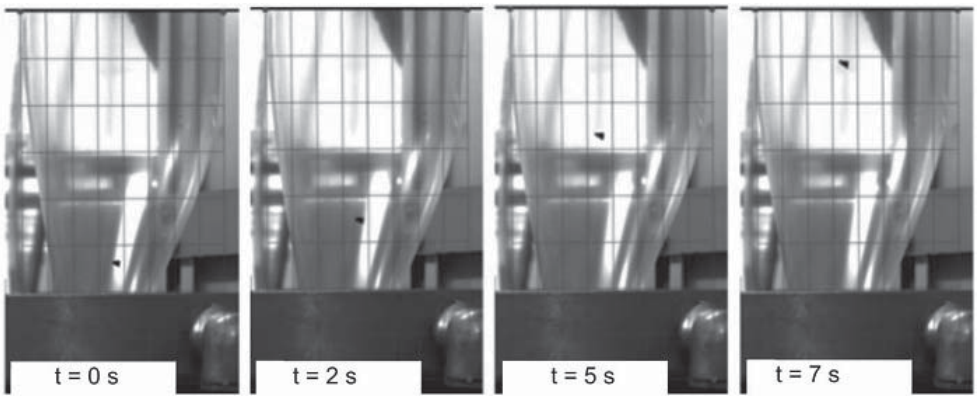

Figure 5.2: Example of marker position in time, machine direction is vertical.

the software, i.e. pixel vs. time, was first converted into distance from the die as a function of time by means of a calibration image, and then smoothed. The axial velocity profile, v_z, as function of distance from the die, z, was obtained by calculating the time derivative of the

data. For each experimental condition, data from three different movies was averaged and fitted with the following expression:

$$v_z(z) = a + \frac{b}{1 + exp(-\frac{z-c}{d})}, \tag{5.1}$$

where a,b,c, and d are all fitting parameters. An example of the measured and fitted velocity profile is plotted in Figure 5.3.

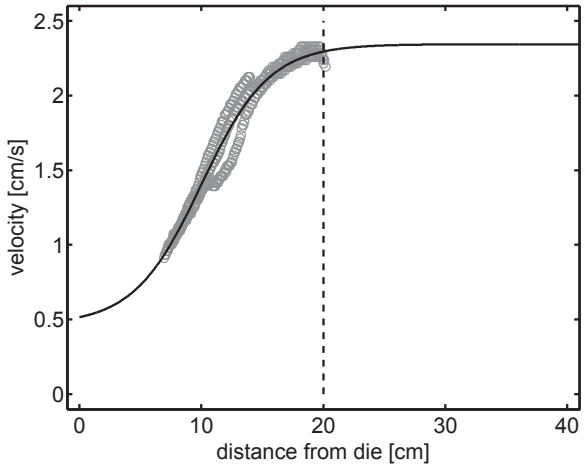

Figure 5.3: Measurements for two markers (symbols) and fitted average velocity profile (solid line) as function of distance from the die. The dashed vertical line indicates the frost-line position.

The particle tracing method was mainly used to acquire the axial position of the frost-line. This is the distance from the die where a constant axial velocity of the fitted profile is achieved, i.e. the melt has changed into a solid. This transition is mainly determined by external cooling of the extruded melt. In practice, a cooling ring is mounted on top of the die with the dual function to increase the cooling rate and stabilize the blown film. For the film blowing setup used, the air flux control was limited, leading to either a frost-line located very close to the die (at high air flux), or, in the absence of air flux, at a large distance from the die. Since the scope of this work was to measure the structure evolution along the machine direction, MD, at multiple distance levels from the die and below the frost-line, no additional air cooling was used. Since the vertical displacement of the extruder was limited, a maximum travel range of ∼25 cm, the X-ray beam could not be directed close to the frost-line height for high TUR conditions (see next section for more details about the setup). Additionally, the camera could not capture a sufficient amount of bubble surface to determine the frost-line height. As a result, the frost-line height could only be analytically determined for the conditions with low take-up ratio, i.e. low film speed, where solidification still took place at relatively close distance from the die. Even so, the results of the experiments at lower TUR still provide valuable information to discuss structure evolution with respect to the frost-line level.

5.2.7 X-ray experiments and framework for data analyses

The film blowing experiments were combined with 2D wide-angle X-ray diffraction (WAXD) measurements at the Dutch-Belgian (DUBBLE) beamline BM26 of the European Synchrotron Radiation Facility in Grenoble, France [13, 185]. The vertical position of the extruder with respect to the X-ray beam could be adjusted by raising the die and extruder step-by-step through a manually operated hydraulic lift table. The adopted setup is shown schematically in Figure 5.4. The source-ray photon wavelength was set to 1.033 Å, the X-ray beam was 300 μm in diameter. Measurements were done at ten die-beam distances between

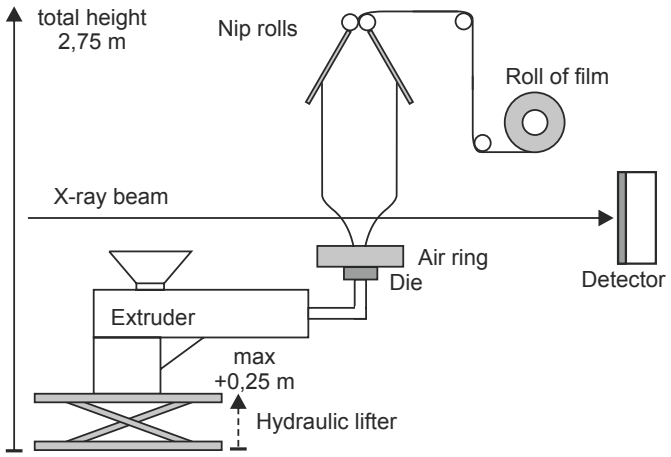

Figure 5.4: Schematic setup of the film blowing device, X-ray beam and detector position.

15 and 40 cm. In each position, 10 WAXD patterns were acquired with an exposure time of 10 s, which resulted in a time average of about 2 minutes. For each height step in a given experiment, crystallinity and molecular orientation were evaluated as the average of at least three patterns. With an average film thickness of about 50 μm, the exposure time used provided a clear diffraction pattern. All patterns were collected by means of a Frelon CCD detector (Photonic Science, UK) with 1024 x 1024 pixels of 97.65 x 97.65 μm placed at approximately 170 mm from the bubble surface. All WAXD data were background subtracted, corrected for static noise, and integrated using the software package FIT2D (ESRF, France). The X-ray crosses the bubble twice and, depending on the bubble diameter, the diffracted patterns of the front and back face of the bubble can be either conjoined or separated. In our experiments, we have taken care that the WAXD patterns are sufficiently separated. From the blown bubble, only the diffraction from the second wall was used throughout the whole of the analysis. The crystallinity level was determined by comparing the area underneath the radially integrated diffraction peaks of the orthorhombic unit cell of polyethylene (d = 4.17 and 3.70 Å), to the total area underneath the diffracted pattern. The amorphous halo, required to evaluate the crystalline contribution, was obtained from a pattern of the molten polymer acquired at a short distance from the die. For the crystallinity a standard deviation of 1.5% was obtained, a typical value for this type of calculation.

Crystal orientation along MD has been estimated from the reflections of the (110) and (200) Bragg peaks, after removal of the scattering from amorphous material, by two different methods: the relatively simple method, based on the full-width-at-half-maximum (FWHM) of the (110) reflection and the more detailed Hermans' orientation factor. The use of both methods allows us to monitor both the overall orientation evolution and, in more detail, the orientation of the a-, b-, and c- crystalline axes of the orthorhombic unit cell of polyethylene. For both cases, the machine direction is considered as 0° and the transverse direction as 90°. In the following, both methods are briefly discussed.

Method I: Full width at half maximum

The intensity distribution of the (110) reflection is used to quantify the overall orientation level by fitting two Lorentzian functions to the azimuthal intensity profiles. The full-width-at-half-maximum (FWHM) of the curve is a measure for the degree of orientation, where a lower value, i.e. a smaller radial extent, indicates a higher level of orientation. In the case of a twisted lamellar structure, or Type I morphology, a summation of two coupled functions is required; the a- and c- crystallographic axis continuously twist around the b-axis, resulting in a (∼50°-spaced) double peak profile [166], such as displayed in Figure 5.5. The expression

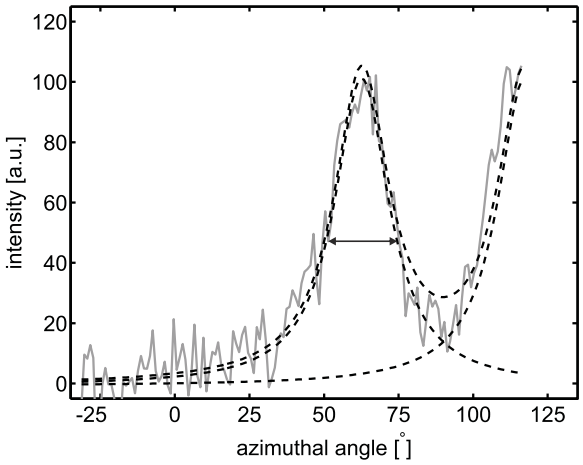

Figure 5.5: Example of fitting the Lorentzian curves (dashed lines) to the azimuthal scattering profile (thick line) to determine the FWHM for a Type I oriented structure.

for each fitted Lorentzian function is given by:

$$I_L(\beta) = A + \frac{B\gamma}{(\beta - \beta_0)^2 + \gamma^2}, \tag{5.2}$$

where A and B are scaling parameters, β_0 the center of a peak and γ is a parameter specifying the width. Now, for the FWHM it simply follows that:

$$FWHM = 2\gamma. \tag{5.3}$$

For reasons of data interpretation, the obtained FWHM is converted in radians and plotted as 1/FWHM, where a higher value represents a higher level of orientation. We found a standard deviation of 4% on the average value of the FWHM.

Method II: Hermans' orientation factor

A second approach to determine the orientation is formalized by using the Hermans' orientation factor [186, 187]. An important constraint of this method for 2D WAXD patterns is the validity of the assumption that rotational symmetry is found in the machine direction, e.g. such as present in fiber production. In the ideal case, pole figures are measured to acquire a unique solution for the distribution of each crystallographic axis [188]. There is no need to argue that this is impossible for the current type of experiment. In this work, we deal with bi-axially stretched films and, at first sight, Hermans' orientation factor does not qualify for determination of the molecular orientation. Nevertheless, since the stretch in the machine direction exceeds the level of stretch in the lateral direction by at least one order of magnitude, it is assumed valid to use this approach without significant miscalculations. Application of Hermans' orientation factor is further supported by investigating the crystal plane orientation (CPO) parameter, which is defined as the ratio between the peaks of the (200) and (110) reflection [189]. In the case of strongly decreasing CPO values, the occurrence of uniplanar orientation of the (200) plane in the direction perpendicular to the film surface would prevent scattering of this plane due to non-Bragg conditions.

The orientation factor is denoted by f_H, which is defined as

$$f_H = \frac{3\langle cos^2\phi\rangle - 1}{2}, \tag{5.4}$$

where ϕ is the angle between the crystallographic axis and a reference axis, e.g. the machine direction, and $\langle cos^2\phi\rangle$ is the average value of the cosine squared of this angle. The orientation factor f_H is zero for a fully random orientation, and 1.0 or -0.5 for a sample fully oriented parallel and perpendicular to the machine direction, respectively.

For the orthorhombic symmetry found in the unit cell of polyethylene, the orientation factors can be calculated from the ratio of the measured reflection of the (110) and (200) planes. The reflection of the (020) plane is calculated based on the relations demonstrated by Wilchinsky [190]. The a- and b-axis orientation (f_a, f_b) can now be obtained by substituting $\langle cos^2\phi_{200}\rangle$ or $\langle cos^2\phi_{020}\rangle$ in the expression for f_H, (Equation 5.4), respectively. Since orthogonal symmetry applies, the total of all orientation factors adds up to 1 and the value for f_c follows automatically. Typically, we found a standard deviation of 0.04 on the average value of the orientation factor, f_H.

5.3 Results and Discussion

The evolution of the microstructure within the blown film is investigated along the machine direction for multiple processing conditions and materials. Different structures of organized lamellae may form during crystallization [163–165]. Hence, two scenarios for flow-induced structure formation are briefly discussed, followed by the results of several characterization techniques which were used to acquire, in detail, the structural features. For clarity we present a stepwise analysis of the data. The effect of different processing conditions on the evolution of crystallinity is evaluated first, followed by the level of orientation, which is quantified by both, the FWHM approach and the Hermans' orientation factor. The FWHM method will provide a measure for the molecular orientation on the arbitrary unit scale, in addition, use of the Hermans' orientation factor allows us to study the evolution of orientation in a more detailed level. Since the results of different processing conditions on the orientation are very similar for the three grades, the latter is only discussed for LDPE1. Finally, the effect of different molecular architectures is discussed by comparing the structure evolution, i.e. the development of crystallinity and orientation, for the different polymers under similar processing conditions.

5.3.1 Background

During the film blowing process and for a given flow condition at sufficiently high temperature, the molecules of the high-end tail of the molecular weight distribution, possessing long relaxation times, are able to orient into fibrous crystals in the direction of flow. Subsequently, lamellae grow laterally outward from these nucleation sites, resulting in the well known shish-kebab structure. The most commonly accepted physical picture of oriented structure formation in polyethylene films is given by the row-nucleated model [163], which is also used for the interpretation of the data presented in this work. To a large extend, the magnitude of stress imposed on the polymer melt, which is equivalent to the molecular stretch [191], controls the crystallization behavior [192]. At low stresses, the lamellae, growing perpendicular to the shish, form twisted ribbons with a preferential orientation of the crystalline a-axis towards the machine direction, which is also known as the (Keller-Machin) Type I structure, displayed in Figure 5.6a. At high stresses, the growing lamellae form regularly folded chains, with the c-axis (or chain direction) parallel to MD; a structure which is also known as Type II, schematically represented in Figure 5.6b. For both cases, a schematic 2D WAXD pattern is included. Considering the level of processing conditions close to resembling industrial values, Type II structures have only been observed in HDPE blown film [193]. For different grades of LDPE and LLDPE, combinations of spherulitic and oriented Type I morphologies can be expected depending on the deformation induced stress level, a function of the molecular architecture [164, 165].

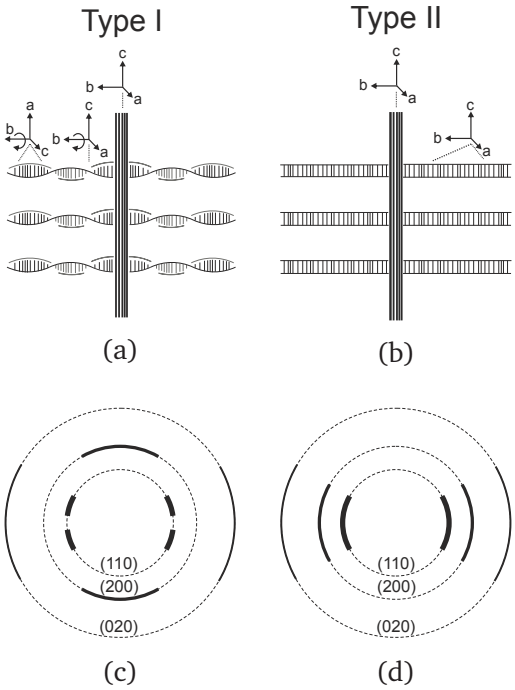

Figure 5.6: Schematic picture and typical WAXD pattern of oriented polyethylene of twisted (a,c) and untwisted/regular lamellae (b,d), machine direction is vertical.

The influence of branching content on (flow-induced) crystallization is less well documented, especially in the case of film blowing applications. In short, branching content in polyethylenes can be composed of long-chain branched (LCB) and short-chain branched (SCB) chains. An increase of SCB will reduce density and maximum crystallinity since less perfect crystalline lamellae can be formed [58]. LCB increases shear thinning and orientability of the materials, the level of LCB can therefore have a large impact on the final morphology of the film. The focus of this research is more on the role of LCB on structure evolution during film blowing. The effect of SCB is only slightly touched on since, based on the density differences, we expect LDPE2 to have a lower content of SCB. Multiple characterization techniques were selected to identify the molecular details and processing related properties for each of the selected materials, i.e. the molecular weight distribution (MWD), the long chain branching content (LCB), the viscosity and elongational properties. Sufficient knowledge on the molecular architecture is of importance in order to anticipate on the differences in structure evolution during the actual film blowing process. Moreover, a much larger set of materials would be required for a comprehensive, systematic study on the combined effect of LCB and SCB and much more experiments need to be done (future work).

5.3.2 Material characterization

Molecular characterization and thermal properties

The most important properties of these materials, determined with DSC and GPC-MALLS, are given in Table 2. From the GPC-MALLS results, depicted in Figure 5.7, it can be concluded

Table 5.2: Materials studied. Density, weight-averaged molecular weight, M_w, and polydispersity, M_w/M_n with M_n the number averaged molecular weight and average long-chain branching, $LCB/1000\ CH_2$, from GPC-MALLS as calculated by the Zimm-Stockmayer model for trifunctional branches. Melting temperature, T_m, and crystallization temperature, T_c, are determined by DSC at a cooling rate 20 °C/min.

Material	Density [g/cm^3]	M_w [kg/mol]	M_w/M_n [-]	LCB/1000 CH_2	T_m [°C]	T_c [°C]	$T_{c,onset}$ [°C]
LDPE1	0.923	390	8	0.35	109	97	101
LDPE2	0.927	200	7	0.24	113	100	103
LDPE3	0.923	200	5	0.29	112	96	100

that LDPE1 has a significantly broader MWD, a larger fraction of high molecular weight and higher LCB degree. LDPE2 and LDPE3 exhibit similar MWD with LDPE3 having slightly more low molecular weight chains. With regard to LCB, quantified by the deviation of measured radius of gyration, R_g, with respect to the linear reference, the LDPE2 has the lowest branching degree of all three samples, even though LDPE2 shows a significant increase in LCB concentration at ultra-high molecular (UHM) weights ($10^6 < M < 10^7$). Since a high UHM weight fraction is needed for the formation of flow-induced structures, it is expected for LDPE1 to show a relatively high amount of orientation compared to the other LDPE grades.

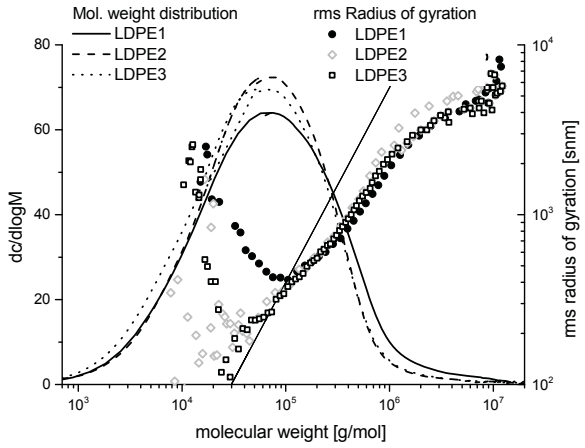

Figure 5.7: Molecular weight distribution and root mean square (rms) radius of gyration, R_g, measured as determined by GPC-MALLS. The solid line represents the reference rms R_g as a function of molecular weight for a linear polymer. The higher the deviation between measured and reference, the higher the LCB degree.

Rheological characterization

The storage and loss moduli of the three grades are given in Figure 5.8, the phase angle versus complex modulus (van Gurp-Palmen plot) and the dynamic viscosity are shown in Figure 5.9. From these data the corresponding Maxwell spectra were determined, see Figure 5.10a. LDPE1 has, in agreement with the measured MWD, a broader rheological spectrum and the highest viscosity of all three grades. LDPE2 and LDPE3 have, mainly due to the narrower MWD, a narrower spectrum. The difference in flowability between the latter two is due to the higher LCB degree of LDPE3 and is mainly observed for the lower dynamic viscosity. The difference in LCB is not manifested in the van Gurp-Palmen plot (phase lag vs. complex modulus); LDPE2 and LDPE3 show almost the same behavior, see Figure 5.9a, while GPC-MALLS reveals significantly higher LCB degree for LDPE3. This is, however, typical for LDPE's; due to the complex branched structure, linear rheology is not sensitive enough to elucidate structural differences. The high branching degree is the main relevant parameter during the extensional flow, since it is believed that this dominates the material behavior during film blowing. Elongation viscosity curves measured at $T_{ref} = 150$ °C are given in Figure 5.11a. Only a small difference is found in the linear regime. For all materials a clear viscosity upturn is observed (strain hardening), with a larger onset time for LDPE3. As stated earlier, the melt temperature during processing was chosen such that the rheological behavior is nearly identical for the three grades for similar processing conditions. Rheological identical is defined here in terms of the Maxwell-spectra, e.g. relaxation modulus and time, which were determined from the rheological spectra in Figure 5.10. By changing the melt temperature during processing, these were made nearly the same, see Figure 5.10b compared to 5.10a. Notice that the linear viscoelastic curve for the time dependent extensional viscosity also becomes the same for the three grades, see Figure 5.11b. The non-linear behaviour can, of course, not be controlled.

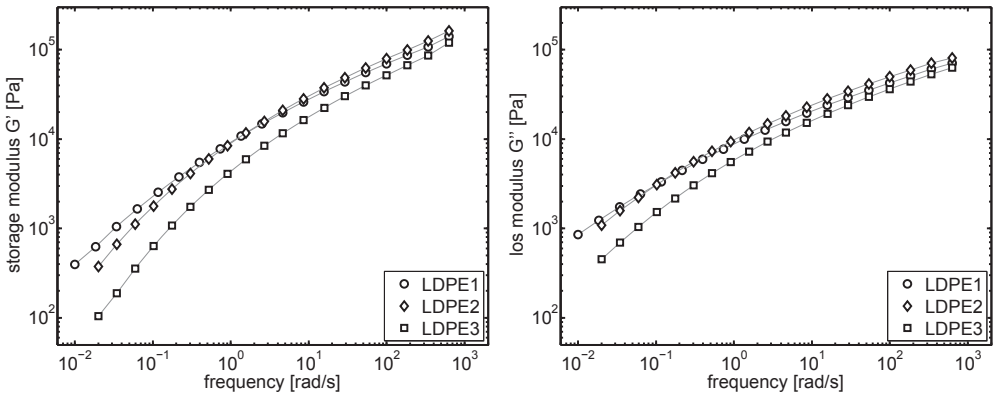

(a) (b)

Figure 5.8: Storage (a) and loss modulus (b) for all LDPE's, $T_{ref} = 190$ °C.

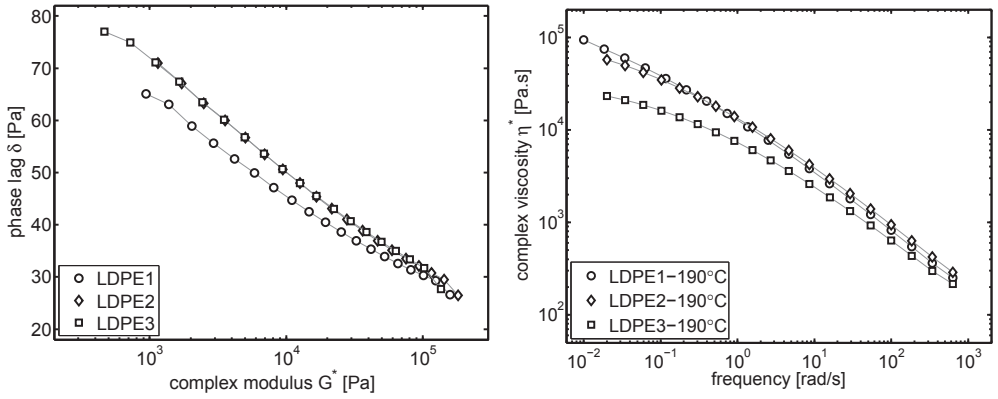

(a) (b)

Figure 5.9: Phase angle vs complex modulus (a) and complex viscosity (b), $T_{ref} = 190$ °C.

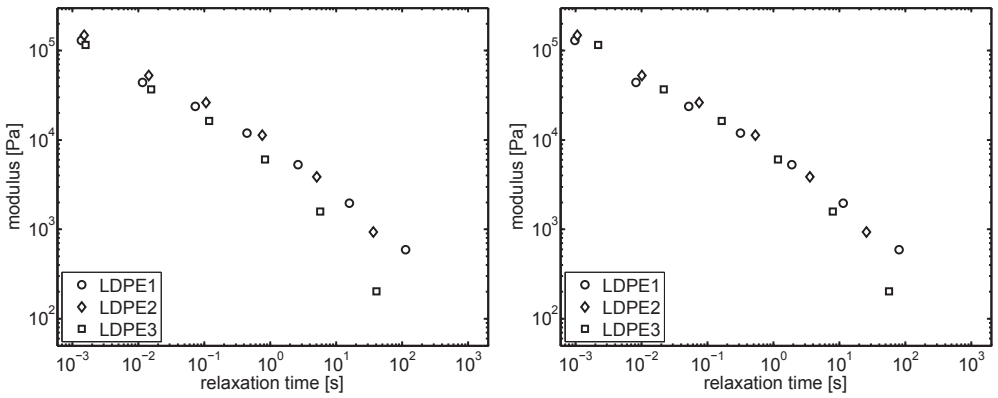

(a) (b)

Figure 5.10: Moduli versus relaxation times for the three LDPE's at $T_{ref} = 190$ °C (a) and at process temperature (b), 200 °C for LDPE1 and LDPE2 and 180 °C for LDPE3, respectively.

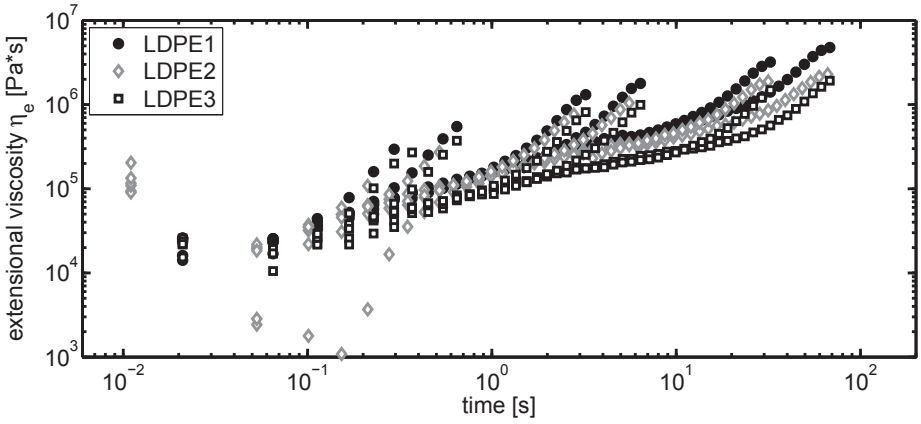

(a)

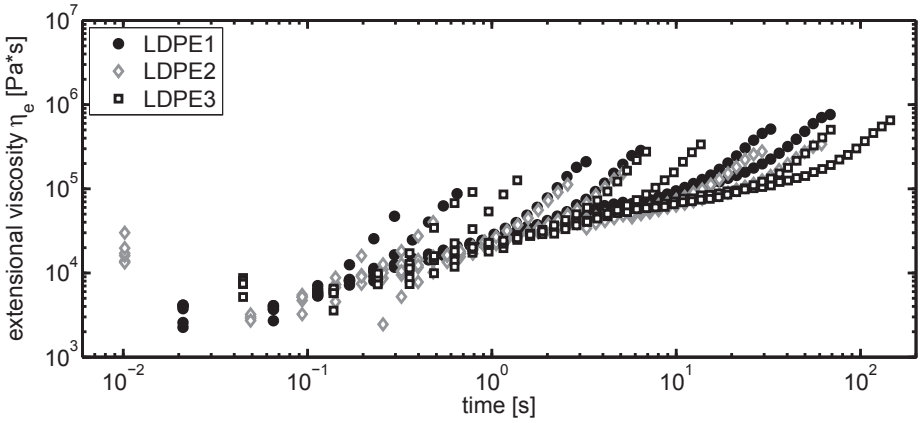

(b)

Figure 5.11: Extensional viscosity versus time for the three LDPE's at T_{ref} = 150 °C (a) and with data shifted to the process temperature (b), 200 °C for LDPE1 and LDPE2 and 180 °C for LDPE3, respectively. Strain rates are 0.05, 0.1, 0.5, 1, 5, and 10 1/s.

5.3.3 Effect of processing conditions

For clarity we have separated the discussion on the effects of processing conditions from the influence of molecular differences between the three grades. The latter will be presented in the next section by using the same results but organized in a different way.

Crystallinity

Changing the processing conditions affects the crystallization process in two different ways: first by influencing flow-induced crystallization (already discussed in Section 3.1) and second by changing the thermal history, in particular the cooling conditions. Once the polymer melt flows through the die-exit, it will experience a level of cooling proportional to the film thickness, the temperature difference between the film and the surrounding air and the (average) velocity of the film. For example, increasing the blow-up ratio results in a

decrease of the film thickness and, therefore, a (slightly) higher cooling rate.

Figure 5.12 shows, for all combinations of blow-up and take-up ratios, the measured crystalline fraction as function of both, the distance and time elapsed since the melt left the die. Due to the height of the air-ring on top of the die, the minimum accessible distance measured from the die-exit is about 15 cm. The maximum distance from the die is constrained by the vertical displacement of the hydraulic lift table and, therefore, the point of full crystallinity development could not be captured, especially for high-TUR conditions. The position of the frost-line, determined from the velocity profile when possible, is also included in these figures.

For the low-BUR/low-TUR setting, which is considered as the 'startup' condition in film blowing, crystallinity gradually develops with distance from the die and reaches a plateau value, just within the investigated window. With an increase of the TUR the crystallinity development takes place further away from the die. The opposite effect is achieved with increasing the BUR. The crystallinity versus time is rather instructive since it shows the evolution of the crystallization for the different conditions more clearly. From Figures 5.12b,d, and f it is seen that, as expected, with higher molecular deformation caused by a higher TUR and/or BUR, the crystallization rate is enhanced. In fact, for all investigated grades, the fastest crystallization is observed for high-BUR/high-TUR conditions, followed by the low-BUR/high-TUR setting, the high-BUR/low-TUR and, finally, the low-BUR/low-TUR condition. This ranking of crystallization rates also evidences that, due to the higher values of axial strain rate in comparison with those in the tangential direction, TUR dominates over BUR in dictating the crystallization rate of the polymers.

With increased stress the frost-line also shifts towards a position closer to the die. It is evident that the frost-line does not mark a crystalline equilibrium state, but rather a degree of crystallization (approximately 15-20%) that transforms the material into the solid state. This indicates that even above the frost-line molecular re-arrangements can still take place. This result is in agreement with similar experiments performed by Ogale et. al. who observed a further sharp increase of the crystallinity closely beyond the frost-line [180].

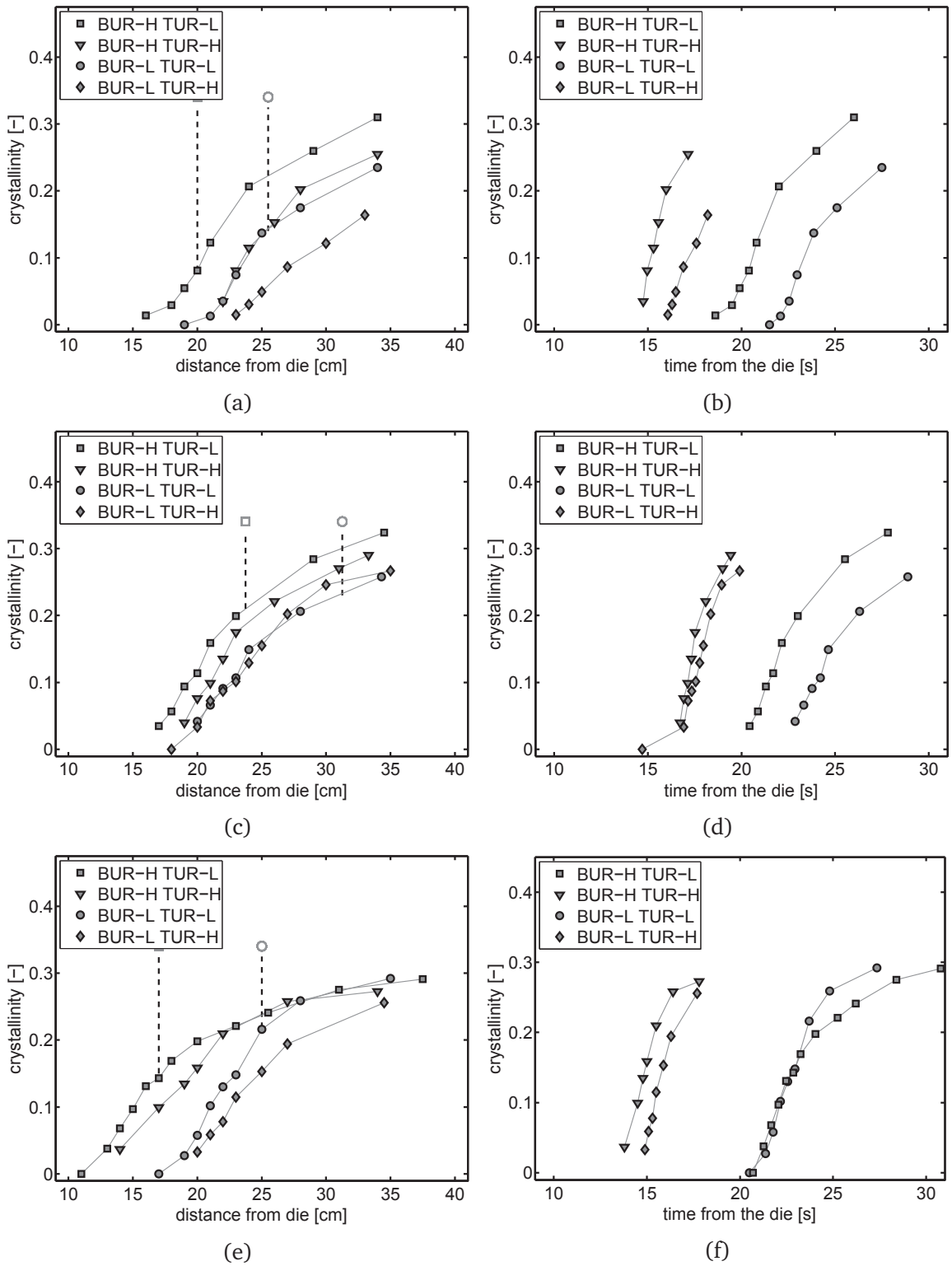

Figure 5.12: Crystallinity of LDPE1 (a,b), LDPE2 (c,d) and LDPE3 (e,f) vs distance (a,c,e) and time (b,d,f) from the die for different processing conditions. Dashed vertical lines represent the position of the frost-line. Indices L and H represent high and low settings, respectively.

Molecular orientation

An indicative measure for the orientation evolution of the crystalline structure is achieved by analyses of the FWHM of the (110) diffraction peak in the azimuthal direction. The results are presented in Figure 5.13. Notice that we present 1/FWHM instead of the FWHM since this shows the trends much more clearly. A sharp decrease in the FWHM of this peak is found at relatively small distances from the die-exit after which it reaches a plateau value. Such a decrease in FWHM is caused by an increasing fraction of oriented structures during solidification. It is clear that the observable development of structural features occurs in a very limited range, typically over a distance of about 5 cm, between 15 and 25 cm from the die exit.

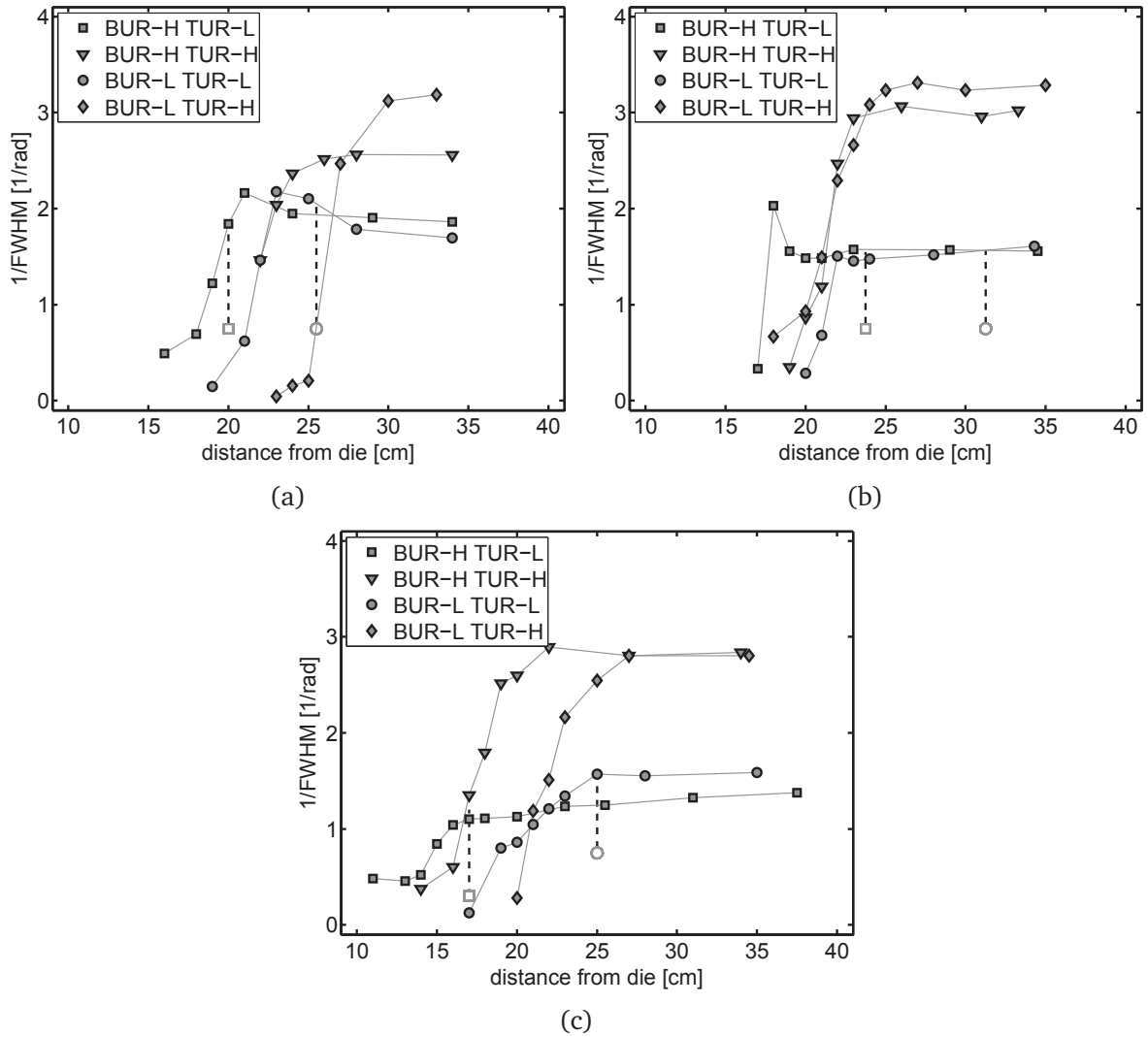

Figure 5.13: FWHM versus distance from the die for different processing conditions for (a) LDPE1, (b) LDPE2 and (c) LDPE3. Dashed vertical lines represent the position of the frost-line. Indices L and H represent high and low settings, respectively.

Regarding the final FWHM level, a difference is found between high and at low TUR. The orientation at the maximum observable distance from the die is larger with higher take-up ratio, especially LDPE2 and LDPE3 show this effect clearly. A much smaller effect is found for the blow-up ratio. Just as observed for the crystalline content, TUR dominates over BUR in affecting the structure evolution. Regarding the position of the frost-line, measured at the point where the vertical velocity component becomes constant, it is observed that the frost-line is mostly located in the beginning of a final FWHM plateau region. This suggests that the frost-line could be a measure for the point where the overall molecular orientation level becomes constant.

For a more detailed picture of the orientation (i.e. at the level of the crystal lattice) we apply the Hermans' orientation factor. This analysis is here restricted to the results for LDPE1. When discussing similar results as a function of the molecular difference (next section), all grades will be taken into account. First, we show that for all experiments and materials, the crystal plane orientation factor (CPO) was found to be independent of the distance from the die, and averaged 0.43 ±0.06 without significant deviations, see Figure 5.14. This result indicates that the experiments described in this study are resembling uniaxial conditions and molecular orientation can be described using Hermans' orientation factor.

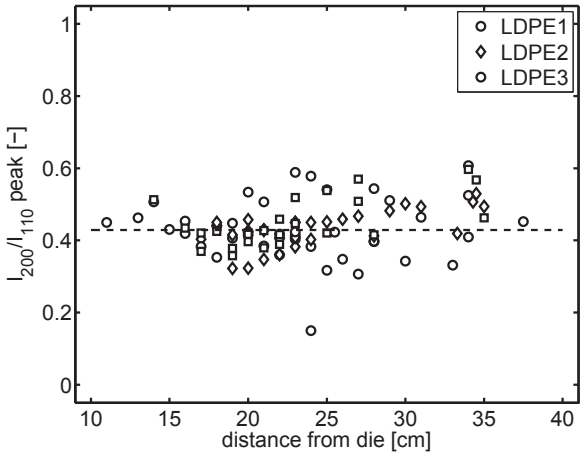

Figure 5.14: Peak ratio between the (200) and (110) reflection vs distance from the die for all materials and experiments investigated. The black dashed line represents the average value.

Figure 5.15 shows the orientation factors, f_a, f_b, and f_c, versus the distance from the die; results are displayed in a sub-figure for each combination of processing conditions. A moderate level of a- and c-axis orientation can be observed. The c-axis is already slightly oriented in the MD at relatively close distance to the die. From that distance onwards, the a-axis orientation increases at the expenses of the c-axis orientation. Meanwhile, the b-axis tends to become almost fully perpendicular to MD. In general, the molecular orientation in the flow direction is low (a value of 1 represents perfect alignment, f_c only reaches a value as much as 0.25). The level of f_c is indicative for the formation of oriented nuclei, row nuclei

or/and shish and regular lamellae in the kebab (Type II). A positive final c-axis orientation, a negative final b-axis orientation and a moderate final orientation of the a-axis is found. The latter can be explained by the formation of twisted lamellae (Type I, see Figure 5.6) in the kebabs that contain, on average, a preferred a-axis orientation. Although it is reported that a high a-axis orientation not necessarily indicates Type I structures [194], a larger number or size of the kebabs must increase f_a at the cost of f_c. Increasing the blow-up ratio at low-TUR shows no significant effect on the orientation of the crystallites. In the case of low-BUR/high-TUR conditions, a clear drop of the c-axis orientation is observed at larger distance from the die. This is accompanied with a pronounced a-axis orientation increase, marking the increase of the amount of twisted lamellae content at later stage. The difference between the evolution of f_c and f_a is best recognized for high-TUR conditions. No noticeable effect of applying different processing conditions is observed in the evolution of f_b, which always tends to approach a value between -0.25 and -0.3.

To confirm that the high a-axis orientation levels are a consequence of the presence of Type I morphologies, 2D WAXD patterns are compared for the minimum (low-BUR/low-TUR) and maximum (high-BUR/high-TUR) conditions, see Figure 5.16. The 2D diffraction images are taken at a maximum distance from the die. In both cases, there is indeed a clear sign of Type I structure formation, indicated by the (200) reflection located at 0° and the partitioned (110) reflection at 90°. Due to scattering from the front- and back-faces of the bubble, minor signs of the scattered front-face can be observed at high scattering angles.

The frost-line height, only available for the conditions presented in Figures 5.15a and 5.15c, shifts towards the die with an increase of the blow-up ratio. It is also observed that f_c seems to level off at the frost-line. This is supported by (but not a proof of) the results found by the FWHM analyses in Figure 5.13. One can notice that for the conditions in Figure 5.15b and d no frost-line could be detected within the range in which the deformation could be measured, and this is in agreement with f_c not leveling off.

As stated before, a large part of the crystalline fraction is formed beyond the frost-line position. A constant f_c indicates that the formation of row nuclei has ceased. Hence, the increase of crystallinity must be caused by the continuing growth of kebab structures, which increase the overal crystallinity level and the average orientation of the a-axis in the flow direction. In additions, f_b evolves towards -0.5 by the continuous growth of the kebabs perpendicular to the direction of the shish. This observation will be discussed for the other polymers in the next section where the effect of molecular composition is compared.

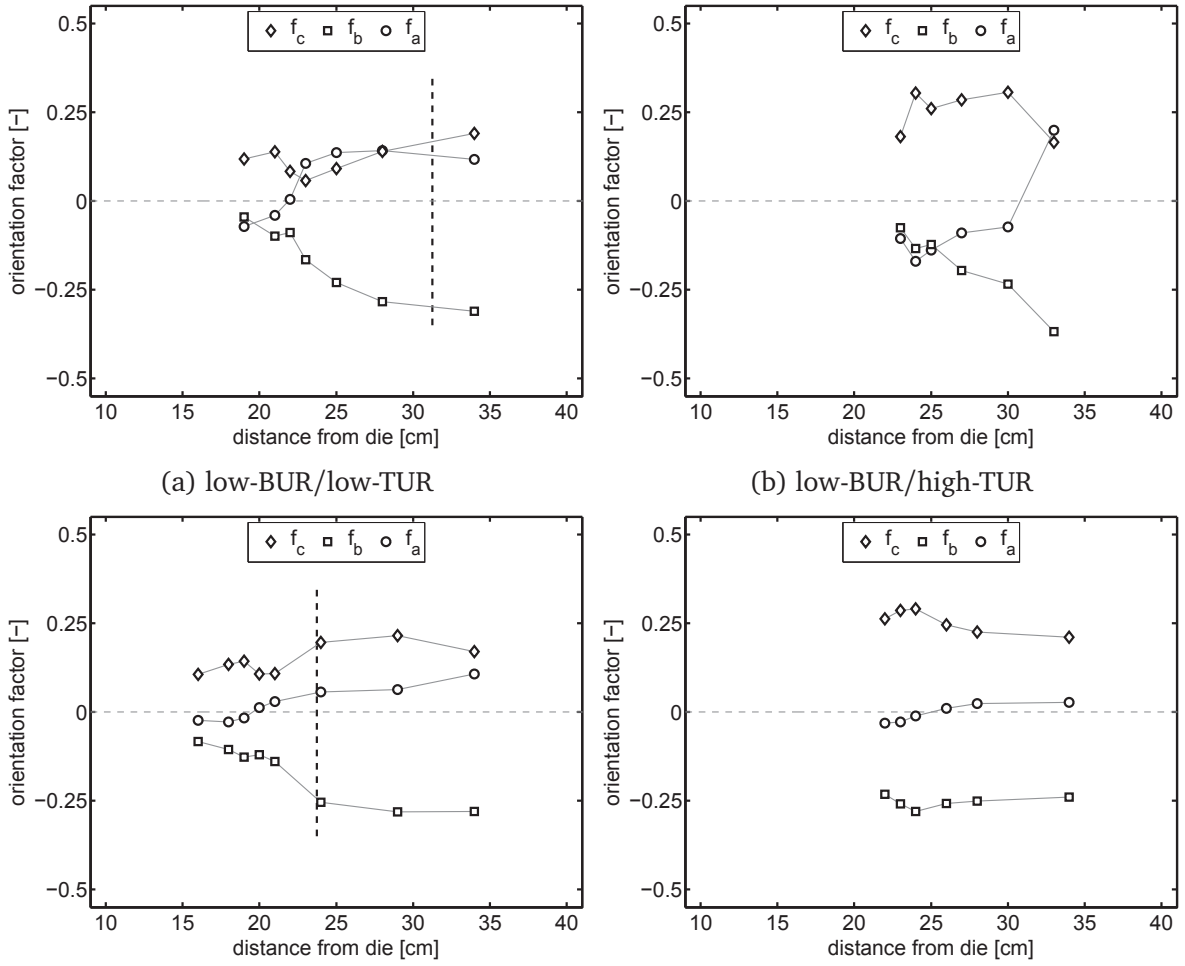

(a) low-BUR/low-TUR (b) low-BUR/high-TUR

(c) high-BUR/low-TUR (d) high-BUR/high-TUR

Figure 5.15: Hermans' orientation factor for LDPE1 for all molecular axes for each different processing condition with high (H) and low (L) blow-up ratio (BUR) and take-up ratio (TUR), respectively. Dashed vertical lines represent the position of the frost-line. Indices L and H represent high and low settings, respectively. On the plotted average values, a standard deviation of 0.04 should be taken into account.

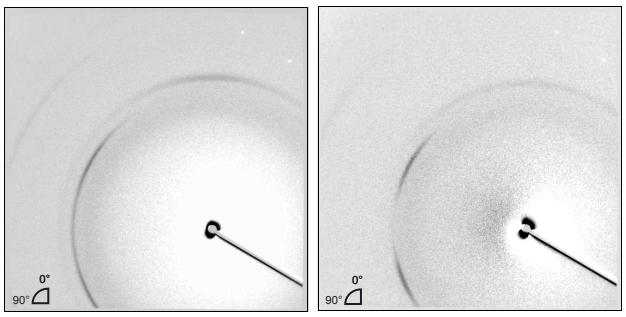

(a) low-BUR/low-TUR (b) high-BUR/high-TUR

Figure 5.16: 2D WAXD patterns for two extreme values of processing conditions for LDPE1, in the lower left corner the machine direction (0°) and transverse direction (90°) are indicated.

5.3.4 Effect of molecular composition

Crystallinity

The development of crystallinity is compared for all grades per processing condition, see Figure 5.17. As stated before, this is the same data as presented in Figure 5.12a,c, and e, but rearranged in such a way that, if it is present, the effect of molecular features is highlighted. The sequential order in the crystallization rate of the three materials immediately becomes clear from the figure. For the conditions investigated, crystallization is found at closest distance from the die for LDPE3, closely followed by LDPE2 and, finally, LDPE1. The (mild) exception is seen for low-BUR/high-TUR where LDPE2 and LDPE3 start to crystallize at the same position. However, is difficult to correlate this behavior to the material properties in Table 5.2. One has to remind that the three LDPE grades were extruded at different temperatures (see Table 5.1) in order to obtain similar rheological conditions during processing. LDPE3 was processed at 180 °C instead of 200 °C as for the other two grades and this can also cause the crystallization to take place slightly earlier in time and distance compared to the other materials. The results suggest that a relatively high M_w in combination with a relatively low M_w/M_n (less content of UHM-chains, or high flow-ability) combined with a significant branching content, i.e. LDPE3, is most effective to achieve a high crystallization rate during the process. From these results we cannot draw any strong conclusion with respect to the final crystallinity level as a function of the molecular characteristics. One could speculate that, based on the higher density and the corresponding lower SCB, LDPE2 should reach a slightly higher final crystallinity level. Although such trend is observed for all cases except low-BUR/low-TUR, it is not really clear so we do not want to draw any strong conclusion on this. Independently of the LDPE grade the frost-line is observed at 20% and ∼15% crystallinity, for the low-BUR/low-TUR and high-BUR/low-TUR conditions, respectively.

Molecular orientation

Once more, the full-width-at-half-maximum is used to provide an estimate of the development of orientation along the MD. This time, data of different materials is combined and plotted in a separate figure for each individual condition, see Figure 5.18.

Clearly, the development of orientation is strictly correlated to the occurrence of crystals, which can be deduced from the sharp decrease in FWHM. Similar to the results presented in Figure 5.13, LDPE3 shows the most rapid transition from the melt towards the oriented crystalline state. This is best observed in Figure 5.18d at close distance from the die. For the other two LDPE grades, the onset of crystallization is less clear, although LDPE2 appears to orient slightly faster.

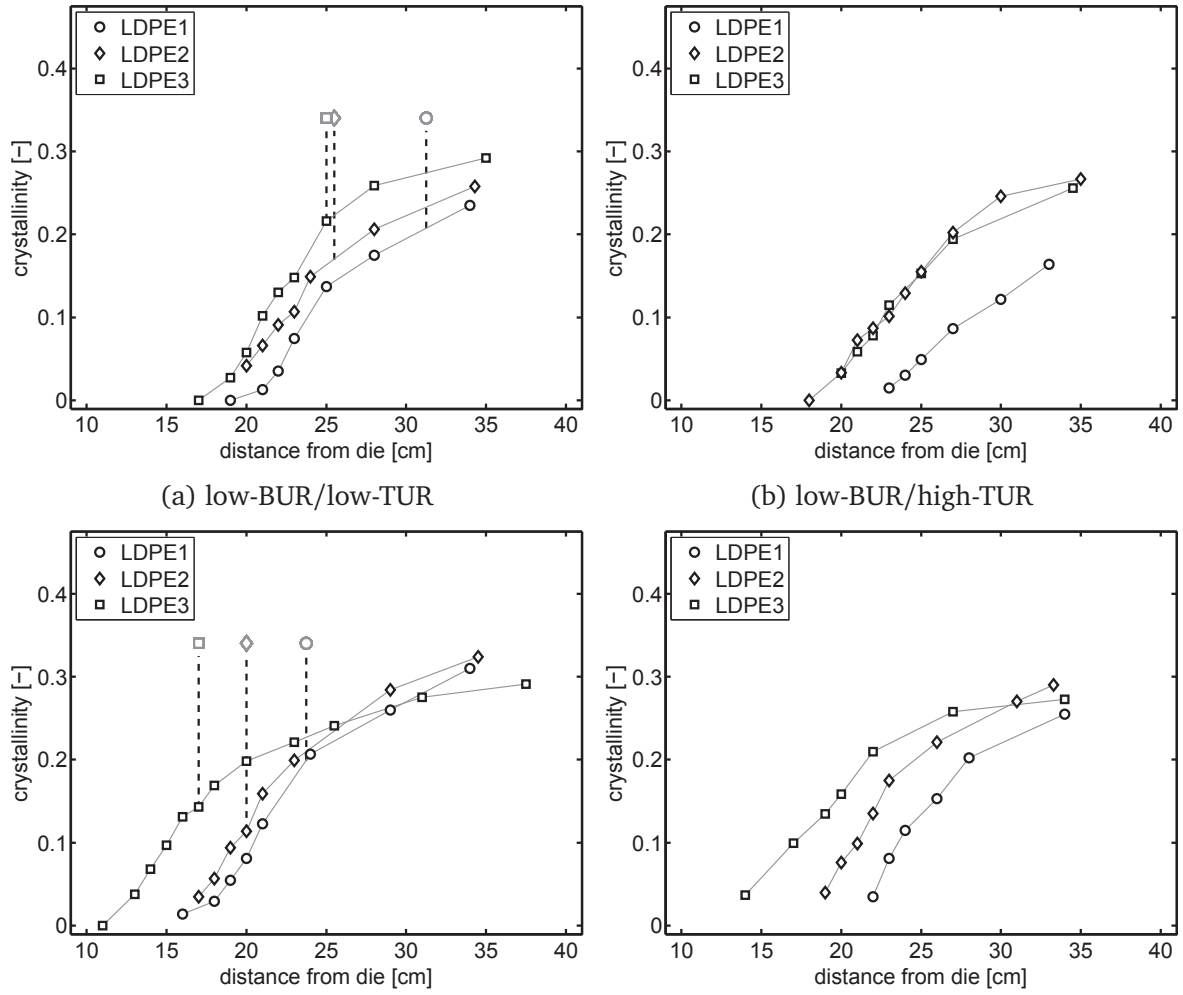

(a) low-BUR/low-TUR

(b) low-BUR/high-TUR

(c) high-BUR/low-TUR

(d) high-BUR/high-TUR

Figure 5.17: Crystallinity versus distance from the die for four different processing conditions. Dashed vertical lines represent the position of the frost-line.

From the data at large distance from the die it follows that the orientation levels scale with molecular weight. The polymer with the higher content of high molecular weight fraction, LDPE1, is able to strongly orient due to stretching, despite the slowest crystallization kinetics. LDPE3, having a slightly lower molecular weight content compared to LDPE2, develops the lowest level of orientation. Apparently, the rate of crystallization and the final level of orientation vary, as a function of molecular weight, in opposite directions. Considering the high-TUR processing conditions, the difference in orientation between the polymers is less pronounced, at least as can be distinguished using the FWHM method.

Since the FWHM method gives only a relative measure of the crystal orientation, the Hermans' orientation factor is again used to further elaborate on the differences in the structure formation. This should allow us to draw more detailed conclusions on the influence of molecular composition on the orientation of each of the crystallographic axes and the relation of these with the frost-line height.

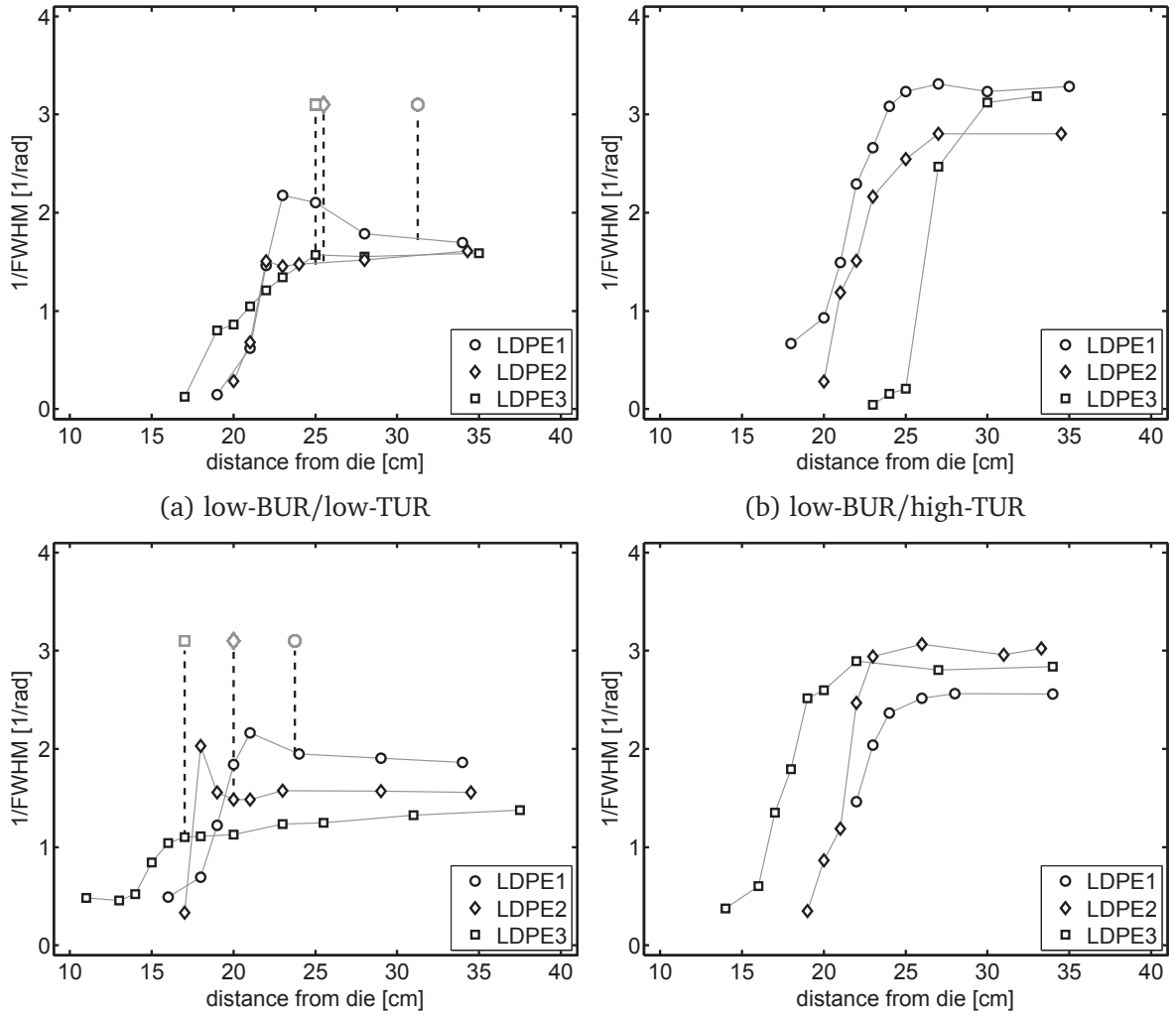

(a) low-BUR/low-TUR

(b) low-BUR/high-TUR

(c) high-BUR/low-TUR

(d) high-BUR/high-TUR

Figure 5.18: FWHM versus distance from the die for four different processing conditions. Dashed vertical lines represent the position of the frost-line.

Data for each crystallographic axis are compared between materials for the different processing conditions, see Figure 5.19 and 5.20. For a low-TUR the results show some scatter, but a clear trend in the development of the orientation of the different axes is visible (see Figure 5.19). Both the a- and c-axis increase in the MD direction while the b-axis orientation is perpendicular to the bubble axis and tends towards -0.3. The orientation factors f_a and f_c are considered as most informative, since f_c indirectly acts as a measure for the mechanical properties in the machine direction [154], and the balance between f_c and f_a gives an indication for the amount of lamellar twisting within the material. LDPE1 and LDPE2 show similar amounts of a-axis orientation where LDPE3 has a significantly lower value. Regarding the c-axis orientation, LDPE3 prevails, followed by LDPE2 and LDPE1, respectively. LDPE3 is highly oriented in the flow direction, which is (although we cannot be conclusive) thought to be due to the high flow ability and the increased branching content.

For high-TUR, see Figure 5.20, remarkably high f_a values are found at low-BUR for LDPE2 and at high-BUR for LDPE3. Apparently, the a-axis orientation is very sensitive for a difference in branching contents upon an increase in BUR. For all high-TUR conditions, the highest c-axis orientation is noted for the high molar mass LDPE1. Meanwhile for LDPE3, the chain direction is only mildly oriented upon low-BUR, where an almost random orientation is observed at high-BUR. The opposite is found for LDPE2, where a low f_c is found at low-BUR, even smaller compared to the value at high-BUR.

It is quite evident that molecular features, such as average molar mass and content of branched repeating units, are reflected in how crystallization kinetics and crystal orientation are influenced by the deformation. However, at this stage, no unambiguous relation can be found between the orientation of the crystallographic axes, processing conditions and the molecular architecture of the polymer. It is clear that blown film extrusion is a complex process where non-isothermal crystallization is influenced by the thermo-mechanical history of the melt inside the die and the bi-axial stretching outside the die. The final result of this entire process is partly determined by the molecular architecture which influences the rheological behavior as well as the kinetics of crystallization. It is strongly believed by the authors that only a combination of extended material characterization (rheological, thermal and flow enhanced crystallization kinetics) [82, 114] and a full numerical model [115,191,195,196], i.e. a model in which all of these aspects are included, will lead to a full understanding of these kind of experiments. On the other hand, such numerical simulations can only make sense when they are compared with the results of experiments at realistic processing conditions, such as presented here.

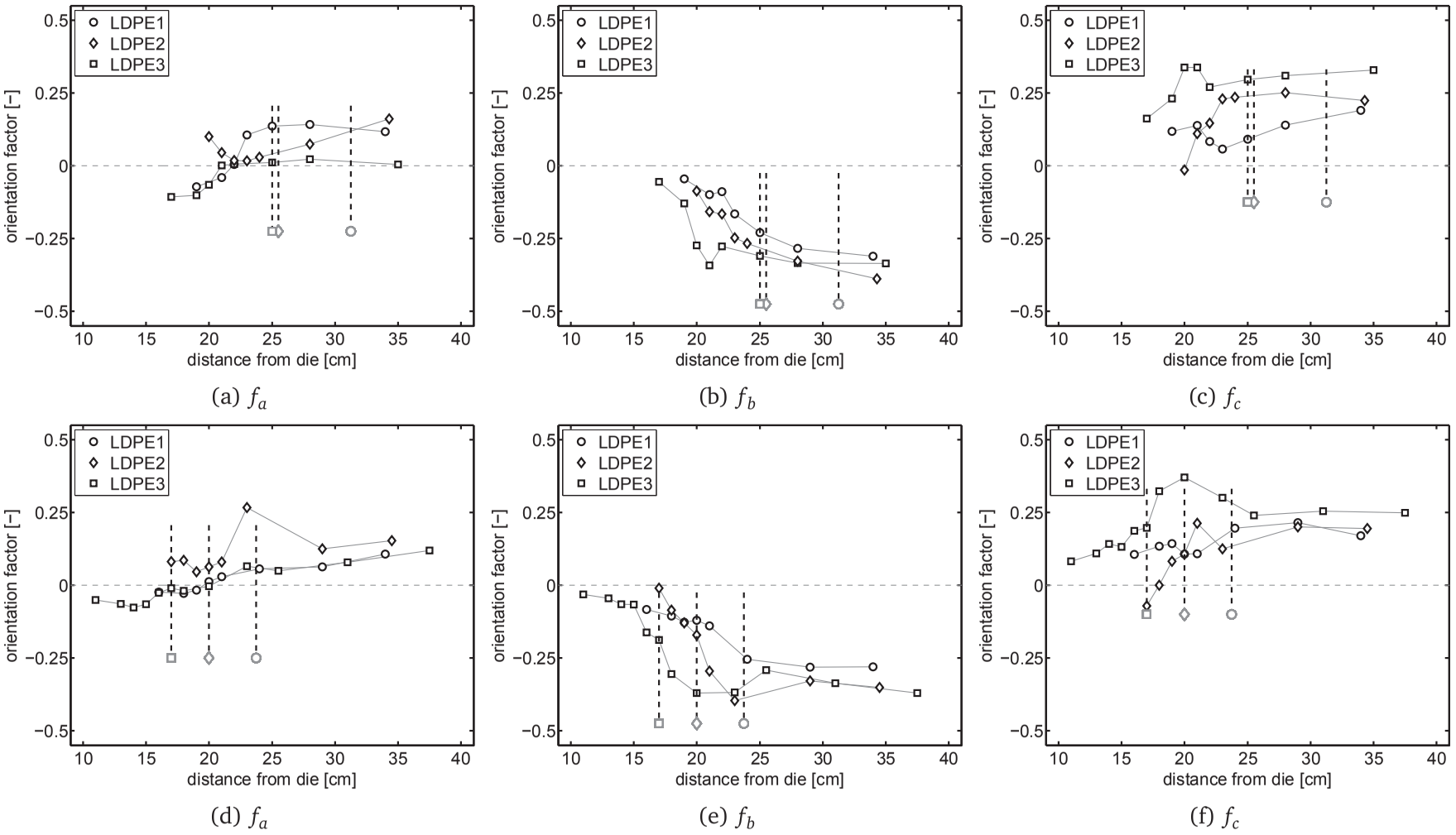

(a) f_a (b) f_b (c) f_c

(d) f_a (e) f_b (f) f_c

Figure 5.19: Hermans' orientation versus distance from the die for the three LDPE's, for low-BUR/low-TUR (top row) and high-BUR/low-TUR (bottom row). Dashed lines indicate the position of the frost-line. On the plotted average values, a standard deviation of 0.04 should be taken into account.

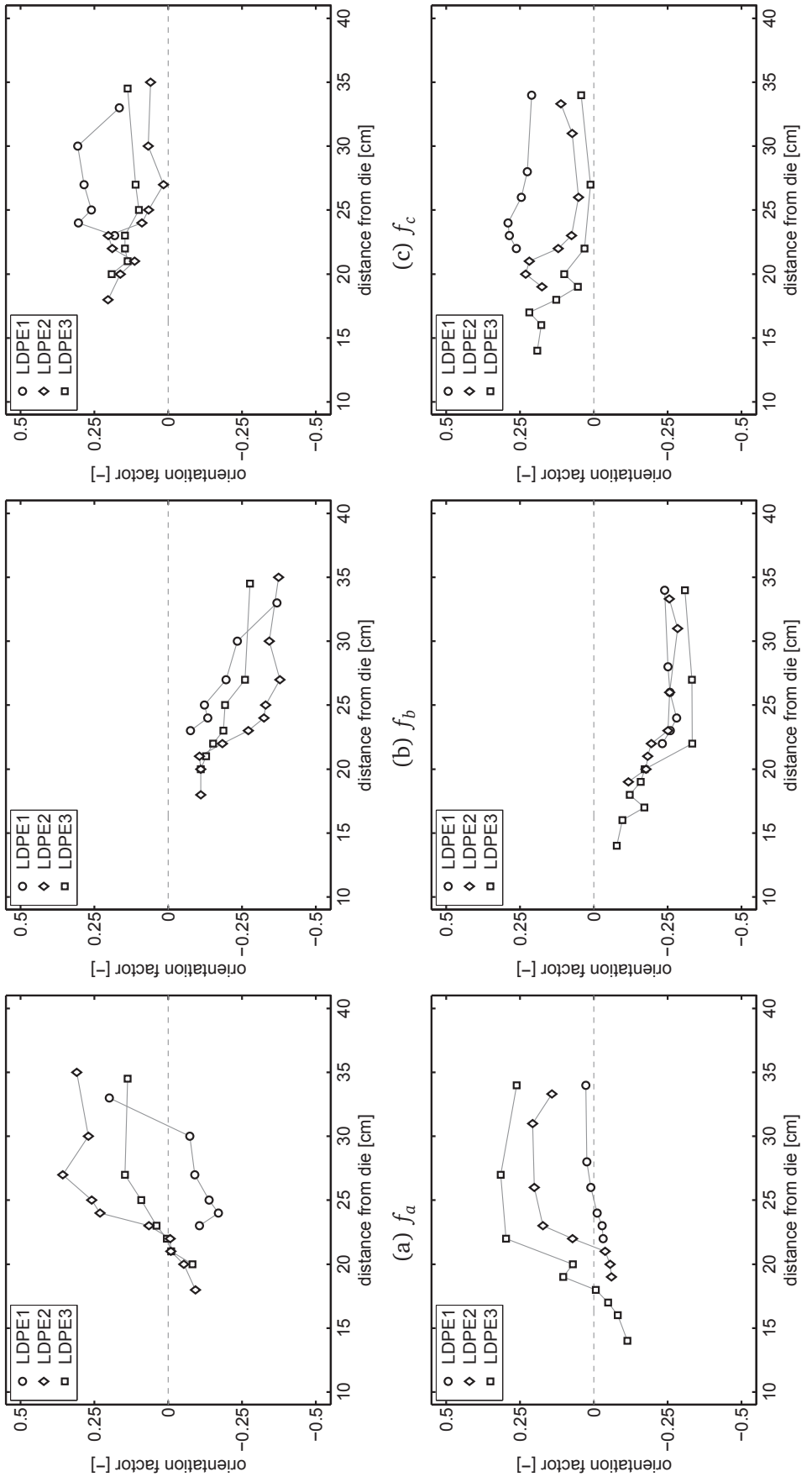

(a) f_a (b) f_b (c) f_c

(d) f_a (e) f_b (f) f_c

Figure 5.20: Hermans' orientation versus distance from the die for the three LDPE's, for low-BUR/high-TUR (top row) and high-BUR/high-TUR (bottom row). Dashed lines indicate the position of the frost-line. On the plotted average values, a standard deviation of 0.04 should be taken into account.

5.4 Conclusion

The experimental work reported in this chapter demonstrates that combining blown film extrusion with synchrotron X-ray radiation enables one to acquire a full set of data describing the evolution of crystallinity and crystal orientation along the bubble, in the machine direction. For the designed set of processing conditions, it is demonstrated that, in terms of the influence on crystallization and orientation, the take-up ratio (TUR) dominates over the blow-up ratio (BUR). Moreover, a combination of a moderate M_w in combination with relatively low content of UHM-chains implies relatively high rates of crystallization, whilst a high molecular weight, as expected, leads to the highest overall orientation level. Also, it was observed that a high branching content and higher UHM fractions do not speed up crystallization. Due to the complexity of the film blowing process, a transient non-isothermal flow enhanced crystallization process with changing non-linear viscoelastic properties, no clear relation between material properties and orientation of the crystallographic axes could be found. For the LDPE's studied and independent of both the material and processing conditions, the frost-line is observed at about ∼20% crystallinity. At this position also the final average orientation of the crystallographic c-axis is reached. Experimental results like these can help to understand and control polymer structuring in industrial practice and, moreover, can be used to validate results from numerical models for film blowing and help to improve and/or extend these models.

Chapter 6

Kinetics of the deformation induced memory effect in polyamide-6

in preparation

Abstract

Nascent polyamide-6 shows a peculiar and irreversible effect; the quiescent crystallization kinetics on cooling are accelerated upon deformation in the melt, even after full relaxation of the melt. This phenomenon, known as the orientation (or better, deformation) induced memory effect of polyamide materials, is explored in a step-by-step manner using in-situ wide-angle X-ray diffraction. For this purpose, unique samples were used, which were created by compression moulding the virgin pellets just below the average melting temperature. The experimental data shows that only the imposed strain level controls the irreversible change in the quiescent crystallization kinetics. During cooling of the undeformed melt, an unusual crystallization behavior is observed, i.e. the stable α-phase converges into the less stable β-mesophase. Possible causes for the memory-effect are discussed and related to hypotheses from the literature.

6.1 Introduction

Polyamide-6 (PA-6) is a semi-crystalline polymer mainly used for engineering applications. The physical properties of the material are significantly influenced by the crystalline morphology within the sample, which, in turn, is controlled by the conditions during processing [49, 197–200]. Two different polymorphic structures may form upon crystallization from the relaxed melt, namely, the monoclinic α-phase [50] and, at high cooling rates or upon cold-crystallization, a pseudo-hexagonal β-mesophase [36,47,49,201]. Both polymorphs exhibit a strong dependency on the intermolecular hydrogen bonding between different amide groups. The most stable α-structure contains fully extended, anti-parallel chains and is characterized by sheet-like hydrogen bonding. The less stable β-mesophase is described as an aggregate of parallel and straight but conformationally disordered chain segments with cylindrical symmetry. The structure of the β-mesophase is much alike the stable pseudo-hexagonal γ-phase, which can be obtained by an iodinating treatment of PA-6 [202, 203], spinning fibres at high speeds [204] or crystallization in confined systems [205]. The existence of the β-mesophase and the γ-phase easily leads to confusion, mainly because the profiles obtained with wide-angle X-ray diffraction (WAXD) are similar. Only a technique based on infrared spectroscopy is able to distinguish between both structures [203,206], although this is not easy. Some authors summarize that, based on the setting of the hydrogen bonds and chain confirmation, the β-mesophase can be viewed as an intermediate structure between the α- and γ-phase [197, 204]. This suggests that the difference between the γ- and β-mesophase can only be found in the degree of crystal perfection [198, 207].

The overview above briefly illustrates the complexity of the different polymorphs present in PA-6. However, what remains is that in the case of quiescent crystallization, for a relaxed polymer melt, the crystallization rate on cooling depends on the temperature dependent nucleation density and growth rate of the crystal aggregates [32, 208]. Melt-memory effects may occur when, prior to (re-)crystallization, a sample is brought to a low temperature or when the annealing period is short. Eventually, this leads to an increase in the crystallization rate [209, 210] or a change of the final crystal morphology [211, 212]. It is well known that for most semi-crystalline systems, prolonged time in the melt prior to crystallization reduces these effects of the original structure by gradual destruction of the crystal aggregates [209, 213]. For polymers with strong hydrogen bonding, such as polyamides, stronger melt-memory effects are reported because the structures are harder to relax [214, 215]. In addition to these *temperature* controlled memory effects, a large difference exists between the crystallization temperature of raw reactor material and mechanically treated polyamides [216–219]. Upon cooling at 10 °C/min, a shift upwards of 15 °C was reported for extruded PA-6 samples. This irreversible phenomena is often called the *orientation* induced memory effect, but for obvious reasons shown in this work is referred to as the *deformation* induced memory effect. This matter forms a long-lasting research topic including ongoing debate

on the (molecular) origin. Different mechanical treatments were classified based on the induced shift in crystallization rate, ranging from solution precipitation (maximum shift) to the untreated virgin material (no shift). Despite the abundance of work published on this topic [205, 216–222], no systematic study on the influence of melt deformation on virgin material is reported *during* solidification and/or melting. The reason for this is found in the fact that dedicated experimental setups always require samples of specific dimensions. Hence, raw reactor material is mechanically deformed prior to structural investigation, erasing the original material behavior. Subsequently, only the *thermally* induced memory effect can be studied instead [223].

The work reported here was inspired by the work of Janssens et al. [222], who studied the deformation induced shift of the crystallization kinetics of virgin material in a step-by-step manner using RheoDSC. After a careful sample preparation procedure, we obtained unique disk shaped samples with crystallization and melting kinetics similar to the raw reactor material. These samples were examined using a shear cell setup combined with WAXD in a synchrotron. Crystallization and melting of virgin material is monitored in-situ after various shear pulses with different strength and total strain. In addition, the effects of delay time and shear temperature were investigated. Possible causes for the measured change in crystallization kinetics are discussed and related to hypotheses from the literature.

6.2 Material and Methods

6.2.1 Sample preparation

The material investigated is a commercial polyamide-6 Akulon grade (DSM, the Netherlands). As-received granular material, from here on referred to as virgin material, was dried for 48 hrs in vacuum at 80 °C according to the specifications supplied by the manufacturer. Disk shaped samples of 32 mm in diameter and approximately 1.2 mm thick were compression moulded at a relatively low temperature of 204 °C for one minute under low pressure. The samples were sandwiched between two thin aluminium layers coated with silicon free release agent to minimize any adherence between the polymer and the aluminium. Each sample was removed from the mould and quenched between two metal plates of room temperature. Immediately after, the sample was sealed in a small aluminium bag, enclosed with standard silica bags to prevent moisture absorbance by the sample. Since sample preparation is a crucial aspect within this work, more details are included in the results section.

6.2.2 Thermal analyses

Differential scanning calorimetry (DSC) was used to investigate crystallization and melting of the virgin and mechanically deformed samples under non-isothermal conditions. Use was made of a Mettler-Toledo 823e/700 module in combination with a Cryostat intracooler. Razor blade cut samples of approximately four mg were placed in standard 40 μL aluminium crucibles. Two subsequent heating and cooling runs were performed, always at a rate of 20 °C/min and in the range of 25-260 °C. The highest temperature was held for five minutes to erase any thermal history. In between both runs an equilibration period of one minute was used at the lowest temperature.

6.2.3 Shear experiments

The influence of strain was investigated using a CSS-450 Shear Cell (Linkam, UK), combined with 2D wide-angle X-ray diffraction (WAXD) measurements at the Dutch-Belgian (DUBBLE) beamline BM26 of the European Synchrotron Radiation Facility (ESRF) in Grenoble, France [13]. The source-ray photon wavelength was set to 1.033 Å, with an X-ray beam of 300 μm in diameter. Patterns were acquired with an exposure time of three seconds at repeated intervals of five seconds. All patterns were collected by means of a Frelon CCD detector (Photonic Science, UK) with 2048 x 2048 pixels of 48.83 x 48.83 μm at approximately 145 mm from the sample surface. Data was integrated, corrected for static noise, and background subtracted using the Fit2D software package (ESRF, France). All integrated scattering patterns were rescaled to a Cu-α radiation source ($\lambda = 1.54$ Å) to easily compare the data to other literature. The morphology of the individual samples was investigated throughout the temperature profile displayed in Figure 6.1. The sample was brought to 260 °C (first heating) and maintained at this temperature for four minutes to erase all thermal history. At the end of this annealing period, a shear pulse was applied. Subsequently, the sample was cooled to 80 °C (first cooling) and kept at 80 °C to ensure the crystallization process was complete. Next, the sample is reheated (second heating) to evaluate the melting kinetics and again cooled to room temperature (second cooling). Unless stated otherwise, cooling and heating rates were always 20 °C/min.
In this way, one X-ray image (three seconds) contains the collected scattering content over one degree Celcius, with a time increment of 5/3 °C between sampling. Experiments were performed to investigate the influence of total strain (0, 9, 18, 27, 54, and 108). For a constant strain value, the shear rate was varied (0, 4.5, 9, 18 and 27 1/s). To investigate the effect of shear temperature (250, 255, 260 and 265 °C, shear temperature kept for one minute after annealing period at 260 °C) and relaxation time prior to the onset of cooling (0, 1 and 3 minutes), a shear pulse with constant strain and shear rate was used.

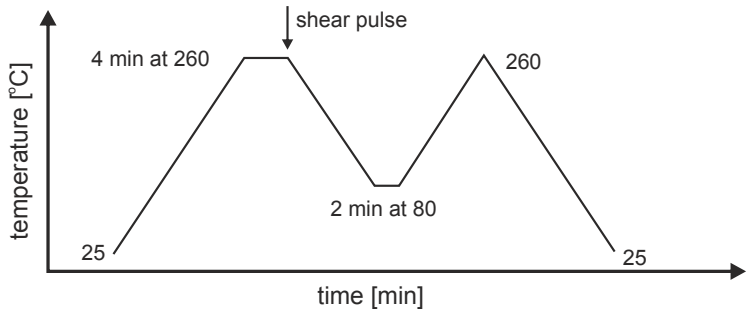

Figure 6.1: Time-temperature profile during the shear cell experiments with in-situ WAXD. Heating and cooling rates are 20 °C/min.

To reduce thermal conductivity of the heating stages towards the frame, and obtain an improved temperature control over the sample, the original plates within the shear cell were replaced with perforated glass plates. Three holes of five mm in diameter were drilled in the bottom glass at 7.5 mm of the centre and 120° inter-spacing. Consequently, to allow for the X-ray beam to pass through the entire setup, strain was applied by rotating the bottom plate n·120°.

6.3 Results

First, the methods used for sample preparation and the initial morphology of the samples is briefly discussed. Second, the outcome of the shear-cell experiments with in-situ WAXD is presented.

6.3.1 Crystallization and melting of differently prepared samples

The objective of the sample preparation process was to obtain specimen that had undergone a minimum amount of mechanical treatment and could still be handled and investigated using the shear cell. Initially, standard methods such as freeze grinding with liquid nitrogen and compression moulding above the melting temperature were evaluated. The melting and crystallization behaviour was investigated using DSC and is plotted in Figure 6.2 and summarized in Table 6.1. Compression moulding the pellets to a thin film of 0.5 mm thick at high temperature resulted in a large shift upwards of 20.2 °C in the crystallization temperature, T_c, relative to the virgin sample. An intermediate case was found for the grinded sample which shows two populations during crystal formation; one high temperature process at 180 °C, the second at approximately 160 °C. Similar results were found for the virgin pellet, where, although a much lower T_c was obtained, a shoulder is noted at higher temperatures. Although the origin of this shift is not discussed here, it can be

hypothesized that every sample, even a pellet obtained directly from the manufacturer, contains a percentage of mechanically deformed material. In the case of the virgin pellet, this section could be located in the shell, where, during the pellet creation process, the highest shear levels are experienced.

Table 6.1: Peak crystallization temperature, T_c and peak melting temperature, T_m, for multiple sample preparation methods during first cooling and second heating at 20 °C/min in DSC.

Sample	T_c [°C]	T_m [°C]
moulded at 260 °C	173.5	216.4
grinded	162.7	216.0
moulded at 205 °C	156.1	215.7
moulded at 204 °C	154.1	212.1
virgin	153.7	211.9

It is well known that the melting behaviour of PA-6 is complex, and may be accompanied with phase transitions, reorganization, and/or multiple melting peaks [205, 224–226]. Two endothermic peaks can be recognized in the heating traces plotted in Figure 6.2b. A shift towards the higher melting temperature, T_m, is displayed for both the compression molded and freeze grinded sample with respect to the virgin sample. Simultaneously, the heating trace of the latter shows a significant re-crystallization peak followed by a double melting process at higher temperatures. This re-crystallization peak was also obtained by Zhang et al. [226], who studied the gradual heating of quenched (non-virgin) PA-6 samples using WAXD and attributed the peak to the formation of a high temperature α-phase. Androsch et al. [227] showed that the less stable β-mesophase within quenched samples gradually converts into α-phase crystals at temperatures above 187 °C, which is well in agreement with the location of the re-crystallization peak in our results. On the contrary, the re-crystallization process of the virgin pellets is observed after cooling at 20 °C/min, which, in the case of a fully relaxed melt, should easily allow for the formation of stable α-phase crystals [36]. Tol and co-workers showed that, in the case of confined PA-6 droplets, crystallization in the region between 175 and 130 °C yields the formation of γ-crystals [205]. They suggest that less stable γ-phase content reorganizes prior to melting and correlate the lower and higher peak to melting of stable γ- and α-crystals, respectively. Hence, the absence of both the recrystallization and lower melting peak for the compression moulded sample suggests formation of purely α-crystals during cooling. This implies that, upon mechanical deformation, structure formation within virgin PA-6 gradually shifts from γ-phase towards the α-phase. The absence of the re-crystallization peak in the 'memory-free' high temperature moulded sample provides a first indication for hindered crystallization in the virgin material. To increase understanding on this phenomena, melting and cooling of virgin and mechanically deformed PA-6 is further investigated in the next section using WAXD.

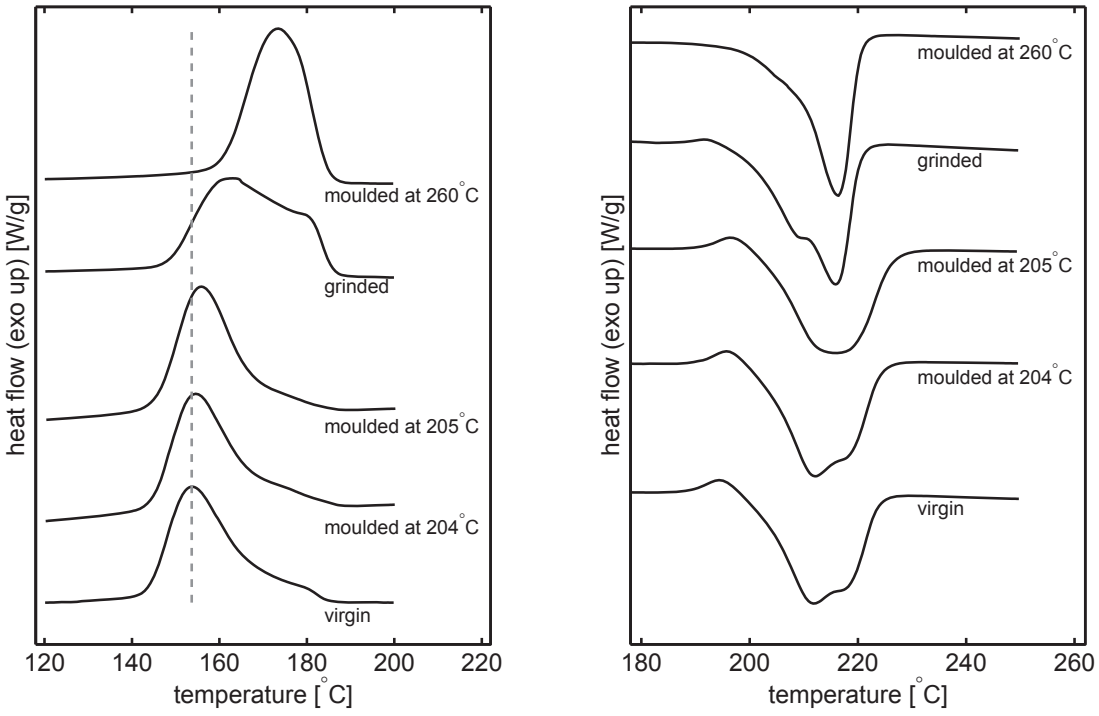

Figure 6.2: Heat flow versus temperature during first cooling (a) and second heating (b) in DSC at 20 °C for multiple sample preparation methods. Vertical dashed line in (a) is included to emphasize the large shift in crystallization temperature depending on the sample preparation method.

The preparation of specimen with similar crystallization/melting properties as the virgin material was realized by compression moulding the pellets at a relatively low temperature of 204 °C. The fraction of the material having the lowest melting temperature (presumably a small portion of the γ-crystals) is used to merge the pellets into a disk, see Figure 6.3. The sample is brittle, but the adherence between the individual, and still recognizable, pellets is sufficient to transport or store the disk in one piece. The crystallization and melting behaviour of the sample was validated using DSC and is included in Figure 6.2. It can be appreciated that the mechanical deformation of the pellets inside the disk is kept to a minimum, showing melting and crystallization kinetics almost equal to the virgin pellets. It is emphasized that the mould temperature selected forms a critical aspect in the preparation of the near-virgin disk. This is illustrated by including DSC traces of a disk prepared at 205 °C, already showing enlarged mechanical deformation, which can be judged from the increased T_c and T_m.

Figure 6.3: Final disk-shaped sample, 32 mm in diameter with near-virgin melting and crystallization kinetics.

Finally, the WAXD reflections of a virgin pellet and a disk shaped sample are compared, see Figure 6.4. A total of three different reflections can be distinguished at scattering angles of 20.3, 21.3, and 23.9°. The pair at 20.3 and 23.9° is associated with the (200) and (020)/(202) lattice planes of the monoclinic α-phase [49]. Here, the (200) plane, α_1, corresponds to the interchain distance within the hydrogen bonded sheets, while the (020)/(202) plane, α_2, reflects the intersheet distance between the sheets. The small peak at 21.3° corresponds to the average interchain distance in the β-mesophase and/or the (001) diffraction plane in the γ-phase. For clarity, this peak is referred to as γ_1, although it might also correspond to the formation of the less stable β-mesophase. In addition, a slight shoulder at 19.2° can be attributed to the so-called amorphous δ-phase, which consists of very small crystallites with many defects [225]. The coexistence of the δ- and α-phase at temperatures well below T_m shows that the crystallinity of the sample is relatively low. During compression moulding, the pellets were kept at 204 °C for one minute and quenched to room temperature immediately after. A decrease of the γ_1-peak can originate from re-crystallization of β-mesophase content into the α-phase upon heating, or by freezing in the random confirmation of the partially γ-crystals upon quenching.

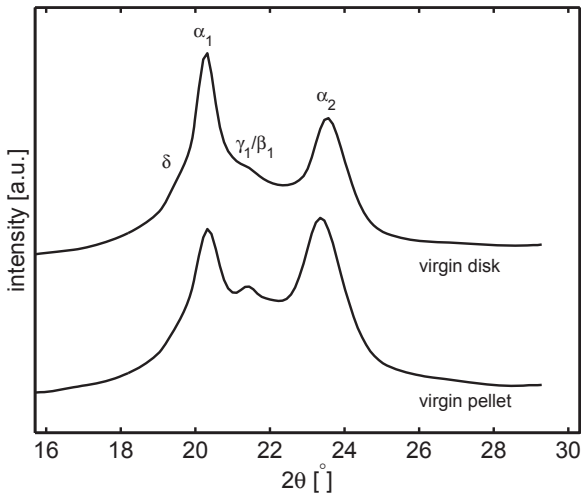

Figure 6.4: WAXD pattern of a virgin pellet and disk at room temperature. Patterns are shifted along the vertical axis for clarity.

6.3.2 Shear cell experiments

First heating

The disk-shaped samples were placed in the shear cell setup and the structural morphology was monitored during the first heating run using in-situ WAXD. In order to homogenize the sample prior to the shear pulse, i.e, remove the interface between the individual pellets and erase the thermal memory effect, the polymer was brought above the equilibrium melting temperature, T_m^0. In the case of PA-6, estimations for this value can be found as low as 215 °C [228] to as high as 306 °C [229]. In practice, annealing temperatures equal to or above 260 °C are considered sufficient [230, 231]. In our case, we used this minimum allowed temperature to avoid sample degradation since the sample was not flushed with a constant nitrogen flow.

Figure 6.5 shows the integrated scattering intensity as function of temperature. During heating, the α_1- and α_2-peak move closer, but do not fully merge into a single reflection. As a result of the anisotropy in thermal expansion of the crystal lattices in cross-chain direction, the monoclinic α-phase usually converts into the hexagonal α^*-form on heating, a process known as the Brill-transition [224, 232]. Although a shift towards higher angles was noted for the (200) plane on heating, i.e. a decrease of the interchain hydrogen-bond length, the two peaks did not fully merge, indicating thermal stability via stable hydrogen bonds until the crystals melted. The slight shoulder of the δ-phase remained present at equivalent scattering angles during heating. From temperatures below 240 °C and onwards, a fully amorphous pattern was obtained.

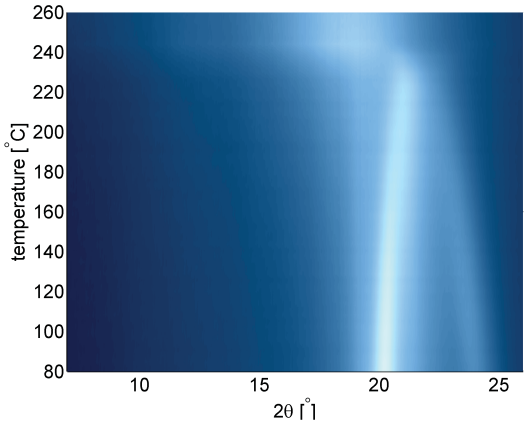

Figure 6.5: Intensity versus scattering angle collected during first heating.

First cooling and second heating without shear

The evolution of the crystal morphology on first cooling and subsequent heating is displayed for the experiment without shear in Figure 6.6. Below 160 °C (with T_c from DSC at ∼155 °C) two reflections are recorded at 21.3 and 10.4° corresponding to the formation of γ-phase (and/or β-phase since we cannot distinguish between these phases), values taken at 80 °C. At lower temperatures, the intense γ_1-reflection shifts towards higher diffraction angles, indicating thermal shrinkage of the diffraction plane. In view of clarification, the temperature window between 180 and 150 °C is plotted in a different way in Figure 6.7a. By superposing the integrated scattering patterns, it becomes clear that, judging from peak broadening at approximately 22°, first a small content of high-temperature α-crystals, α', is formed. At slightly lower temperatures, the amorphous halo decreases significantly and the γ_1-peak emerges. These results are in agreement with the DSC cooling scans of the virgin pellet included in Figure 6.2a, where a high temperature shoulder was obtained prior to the main crystallization peak. Both the peak and shoulder in DSC can now be attributed to crystallization of the high temperature α-phase and the γ-phase or β-mesophase at lower temperatures, respectively. What is unusual is that, simultaneously with the appearance of the γ_1-peak, the weak reflection corresponding to the (200) plane of the α'-phase gradually merges with the intense γ_1-peak. From the scattering data it is clear that the α'_1-reflection shifts to higher angles, corresponding to a decrease of the interchain distance within the hydrogen bonded sheets.

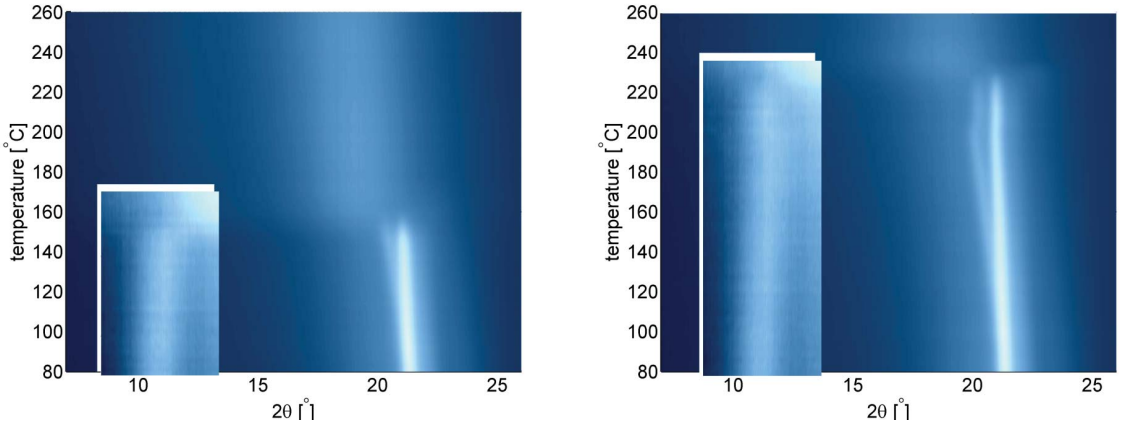

Figure 6.6: Intensity versus scattering angle collected during first cooling (a) and second heating (b) of a virgin sample without shear. The (weak) peak at 10.4° is inserted separately with a different range of the intensity in order to increase contrast.

A possible transition of the apparently meta-stable α'-crystals to γ-crystals is provoked by a cooperative twist of the molecular chains about the amide groups, which enables the hydrogen bonds to switch from antiparallel chains to parallel chains [233]. It is important to note that this transformation is commonly observed in reversed order on heating [200].

Interestingly, this is also the case in this experiment, see Figure 6.6b. The evolution of the γ_1 and α_1' peaks is fully reversible. It is presumed that the shift of the α_1'-reflection towards lower angles corresponds with the arrangement of hydrogen bonds within the (200) planes, which reaches equilibrium at approximately 190 °C. Finally, the weak scattering signal at approximately 22° at 230 °C is attributed to melting of stable α-phase crystals present in the pre-deformed part of the pellet. For clarification purposes, this part of the heating segment is again plotted separately in Figure 6.7b. On heating, only a fraction of the structures that correspond to the γ_1-reflection converges into α'-crystals. Again, notice that the diffraction patterns of the γ- and β-mesophase are indistinguishable. Penel-Pierron et al. [203] showed that melt-cast films of β-phase morphology reorganized into the stable α-form on heating from 120 °C onwards. In addition, they reported that the stable γ-phase may undergo a transition towards the α-phase, however, only upon tensile drawing and at high temperatures. Deducing from these results in literature and the high melting peak of the γ_1-reflection in our experiments, i.e. above 215 °C, we can conclude that the remaining structures contributing to the γ_1-reflection correspond to stable γ-crystals. Meanwhile, the present β-mesophase reorganizes into α-crystals. No such re-crystallization process was observed during heating in DSC in the 120-180 °C range, which suggests that the observed transition in WAXD is largely thermally balanced or that the heating rate applied in DSC was too high to clearly distinguish this process. Although we cannot draw any strong conclusions based on our combined observations from DSC and WAXD, it is hypothesized that the unusual and reversible transformation between the α-phase and the β-mesophase is caused by a strong molecular memory effect. For verification purposes, this experiment was repeated for two different samples, from which equal data was obtained. Data on second cooling is equivalent to first cooling (not shown).

No observations can be made in the scattering data related to the re-crystallization peak obtained in DSC at ∼190°C. On the other hand, the lack in α-phase reflections confirms the perfectioning process of γ-crystals proposed by Tol [205].

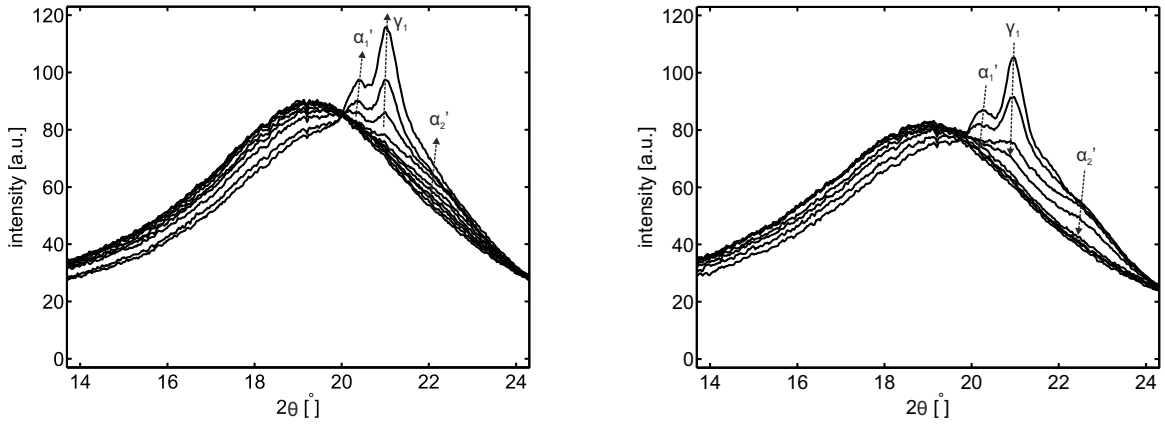

Figure 6.7: Integrated scattering signal of patterns in the range of 180-150 °C on first cooling (a) and in the range 224-244 °C on second heating (b) of a virgin sample without shear.

Effect of strain

Multiple experiments were performed with varying shear pulses to investigate the influence of mechanical treatment on the deformation induced memory effect. As a typical example, the evolution of the crystal morphology after maximum deformation (total strain = 108, shear time = 12 s, and shear rate = 9 1/s) is examined. The scattering profiles during first cooling and second heating are displayed in Figure 6.8. Compared with the unsheared sample (Figure 6.6), the shear pulse did have a great effect on the crystallization and melting kinetics. The sample shows an enhanced crystallization rate, where first signs of crystal reflections can be recognized from 180 °C onwards. This shift in T_c with respect to the virgin sample (T_c = 155 °) corresponds to the observations made in DSC, Figure 6.2a. On cooling, one clear peak is first formed due to the occurrence of the hexagonal α^*-phase. Towards lower temperatures, the Brill-transition, i.e. expansion and shrinkage of respectively the (200) and (020)/(202) difraction plane, leads to the characteristic scattering angles at 20.3 and 23.9° of the monoclinic α-phase. On heating, the reversed process is recognized. These WAXD patterns evidence the formation and melting of stable α-crystals only. No signal reflecting the growth of either the γ- or β-phase is detected, indicating that the deformation induced memory effect is fully erased by the mechanical deformation applied.

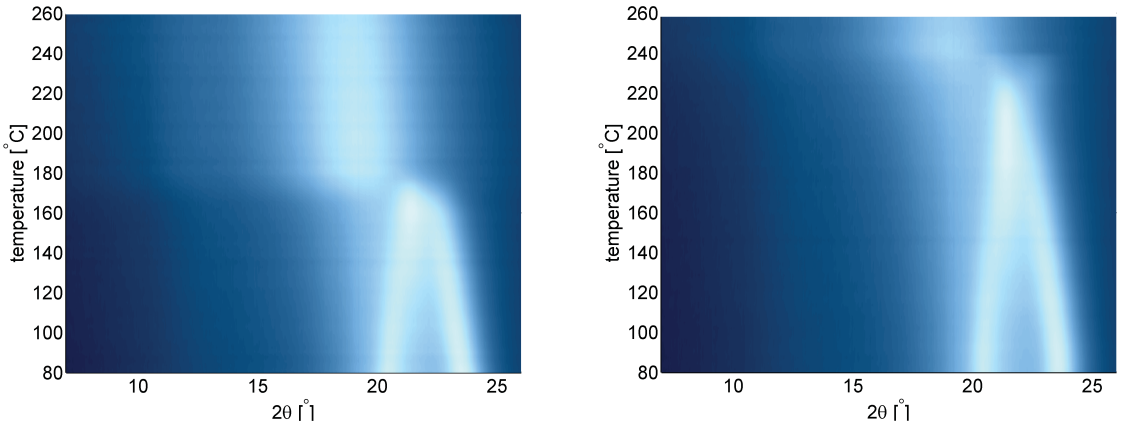

Figure 6.8: Intensity versus scattering angle collected during first cooling and second heating for a sample exposed to maximum strain.

Next, the effect of different total strain is evaluated. Rather than to compare the integrated scattering intensity versus temperature for each experiment, the WAXD reflections at (or closest to) 80 °C during second cooling are collected. An overview is presented in Figure 6.9 and a summary of the flow conditions is given in Table 6.2. It is clear that with strain, the final morphology progresses from a dominant γ-phase/β-mesophase towards the α-phase. For the minimum strain value, still a small γ_1-reflection is detected. Hardly any difference can be noted between the WAXD patterns after a total strain of 54 and 108. Remarkably, first the α_2-peak increases with strain, followed by the α_1-peak.

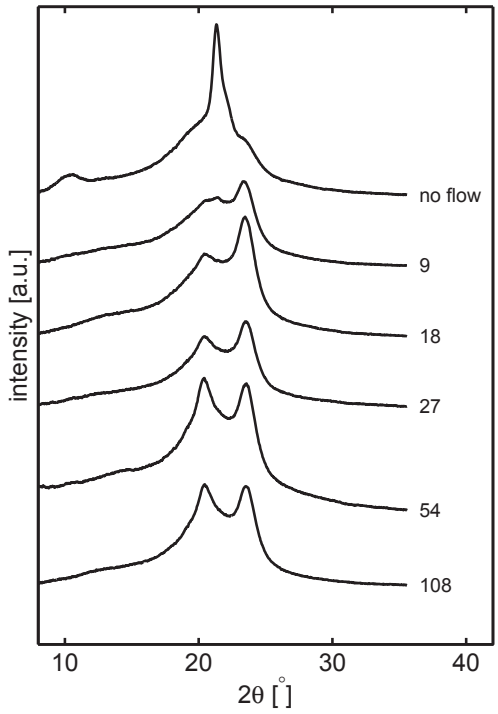

Figure 6.9: Intensity vs scattering angle at 80 °C during second cooling for samples with different total strain. Patterns are shifted along the vertical axis for clarity.

Table 6.2: Details on the different shear pulses given during separate experiments. Shear temperature was 260 °C, cooling started directly after the shear pulse.

Experiment	Strain [-]	Shear rate [1/s]	Shear time [s]
1	0	0	0
2	9	9	1
3	18	9	2
4	27	9	3
5	54	9	6
6	108	9	12

Since the shear temperature was set to 260 °C, no molecular orientation within the sample is expected as a result of flow-induced crystallization. To rule out any possibility of preferred crystal orientation in the direction of flow, the WAXD patterns were evaluated. As it can be appreciated from Figure 6.10, all individual Debye-rings show a constant intensity along the azimuthal angle. Small signs of orientation seem to show in Figure 6.10f, although a similar effect in the inner reflection of the kapton film suggests a slight misalignment of the shear cell setup with respect to the X-ray beam. We do not consider this as important.

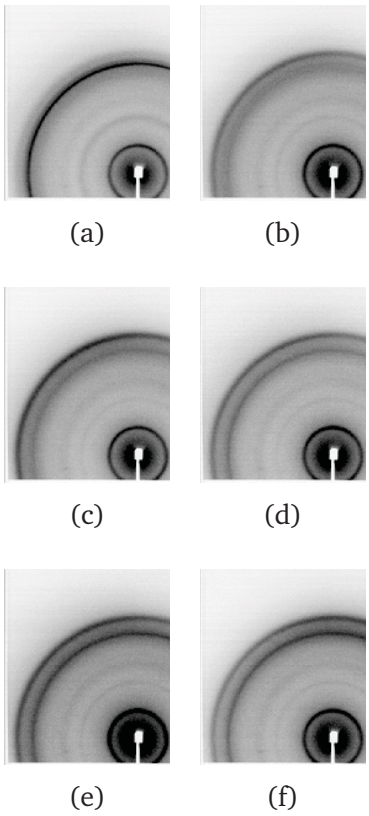

Figure 6.10: WAXD patterns obtained during second cooling at 80 °C for experiments 1-6 (a-f).

Since both the α_1- and α_2-reflection increase with strain while maintaining their respective peak position, see Fig. 6.9 and 6.10, it can be concluded that strain does not effect the level of crystallographic mismatches. After all, this would lead to significant peak broadening or a departure of the α_1- and α_2-spacings from their ideal value [204]. Unfortunately, these 2D WAXD experiments do not reveal details on crystallographic orientation in the gradient direction. This prevents us from drawing strong conclusions on any crystal anisotropy at low strain. For simplicity, we will use the ratio between the intensity of the α_1- and α_2-peak as a characteristic measure for the transformation between a virgin sample and one wherein where the memory effect was fully erased, i.e. an isotropic crystal structure was obtained. Results are plotted in Figure 6.11 for all variables investigated. Integrated scattering patterns are not shown here but included in the Appendix instead. From Fig. 6.11a it can be appreciated that the peak-ratio progresses towards an equilibrium value with strain. Herein, the first experiment with non-zero strain forms an exception since the γ_1-peak superposes both α-reflections, i.e. the peak ratio can be determined in a less accurate way (see again Fig. 6.9). Equilibrium is reached between 27 and 54 strain units, which uniquely provides a quantitative measure for the mechanical deformation needed to fully erase the memory effect. Concerning the other experimental parameters, shear rate, delay time, and shear temperature, it is evident from respectively Fig. 6.11b-d that, within experimental error, the crystalline morphology is not affected.

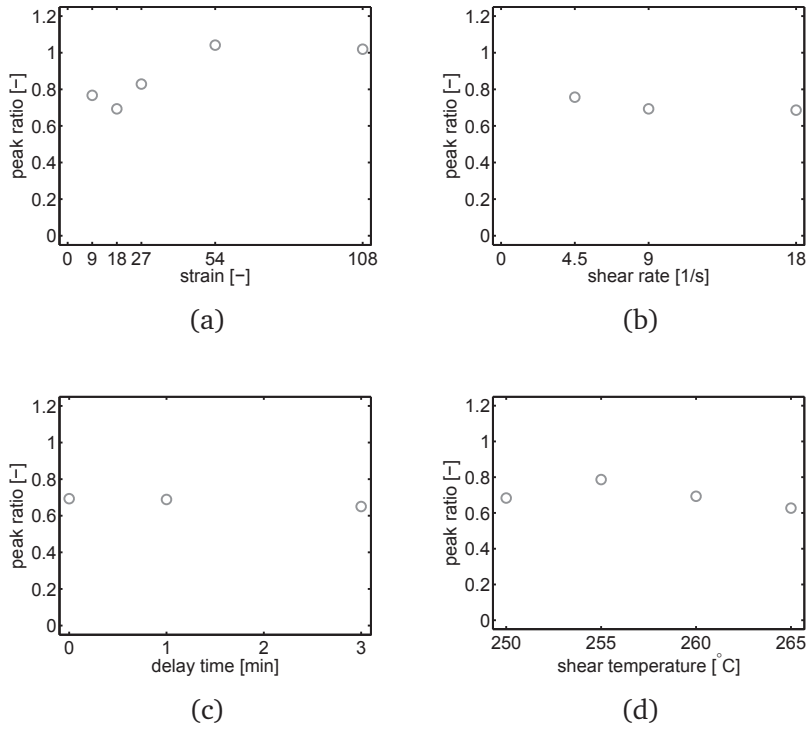

Figure 6.11: Peak ratio of the α_1- and α_2-reflection as function of strain (a), shear rate (b), delay time or relaxation time af shear (c), and shear temperature (d).

6.4 Discussion

In this section, possible causes for the memory-effect are discussed using the experimental data at hand and relating these to hypotheses from the literature [221, 222].

Perhaps the most straightforward explanation for the observed shift in T_c could be found in a decrease of the molecular weight following mechanical treatment. Processing the virgin pellets could lead to a reduced viscosity and facilitate increased chain mobility. However, multiple authors showed by using gel-permeation chromatography (GPC) that after a first processing cycle, the molecular weight remained constant while the crystallization kinetics were enhanced [217, 234]. In addition, a lower molecular weight could not explain the shift in polymorphism shown in Figure 6.9.

A second explanation could be found in the improved dispersion of heterogeneous contaminants, incorporated throughout the matrix material during processing. Melt deformation would increase the nucleation density, providing a higher crystallization temperature and allow for the formation of a large number of smaller spherulites. This hypothesis does not clarify the preferred γ-phase crystallization at lower T_c, neither the experiments of Aharoni [220], who observed a maximum shift in T_c when virgin PA-6 was diluted in a pure solution, free of any form of contaminant.

The third and most likely possibility involves an initial confinement of chains due to an inhomogeneous hydrogen bonding activity. It is well established that conditions that allow for limited chain mobility, such as high cooling rates, low temperatures, or the presence of a large number of nanocomposites, promote the formation of γ-crystals and/or β-mesophase [36, 225–227]. Meanwhile, slow cooling or high crystallization temperatures lead to unrestricted formation of α-phase. It is known that a large number of inter- and intra-molecular hydrogen bonds are still present above the melting temperature [235]. Therefore, clusters of these hydrogen bonds cannot be removed by an annealing process alone, a certain level of mechanical treatment is needed to break and evenly distribute these clusters. In the RheoDSC study of Janssens [222], it was shown that erasing the memory effect becomes easier in the presence of water. Hence, complementary to the reduction of the glass transition temperature with moisture content [236], it becomes easier to drag the chains out of their 'locked' confirmation because of increased molecular mobility. If we review the unusual crystallization behaviour observed in Figure 6.6, the virgin sample first crystallizes from the melt into the γ-form, wherein hydrogen bondings is almost complete [237]. In addition, a small fraction of α-crystals is formed, which, most probably, is forced to reorganize into the β-mesophase because of energetic reasons. On heating, the mobility of the chains is again increased, releasing the stress on the β-mesophase which recrystallizes into the α-phase [207].

6.5 Conclusions

The main results concerning the crystallization and melting behaviour of virgin PA-6 upon melt deformation are the following.

- Even an as-received PA-6 pellet contains a small fraction of melt deformed material. Unique disk-shaped samples, with unaltered properties with respect to the virgin pellets, were realized by compression moulding at relatively low temperature and used in a shear cell with in-situ WAXD. The ability to produce such samples is crucial for the following shear experiments.
- The melt-memory effect in PA-6 is purely governed by strain. Upon mechanical deformation in the melt, the material gradually shifts from stable γ-form crystallization at lower temperatures towards formation of the stable α-form at higher temperatures and this effect saturates at a critical strain.
- An unusual and reversible phase-transition between the α- and β-mesophase is observed for the sample without shear.

The discussion on the molecular origin of the melt memory effect is still open. This matter is not answered here in detail. Therefore, suggestions for future research include:

- The use of FTIR to distinguish between stable γ-crystals and less stable β-mesophase within the virgin samples during or after cooling.
- Investigate the influence of strain on the specific crystal orientation using 2D WAXD with the X-ray beam parallel to the shear direction.

Acknowledgements

The authors would like to thank A. Stroeks, L. Balzano, and P.C Roozemond at DSM for the useful discussions. D. Cavallo is acknowledged for the assistance with the glass plates. The authors are indebted to the people at DUBBLE - ESRF for the X-ray beamtime provided.

Appendix

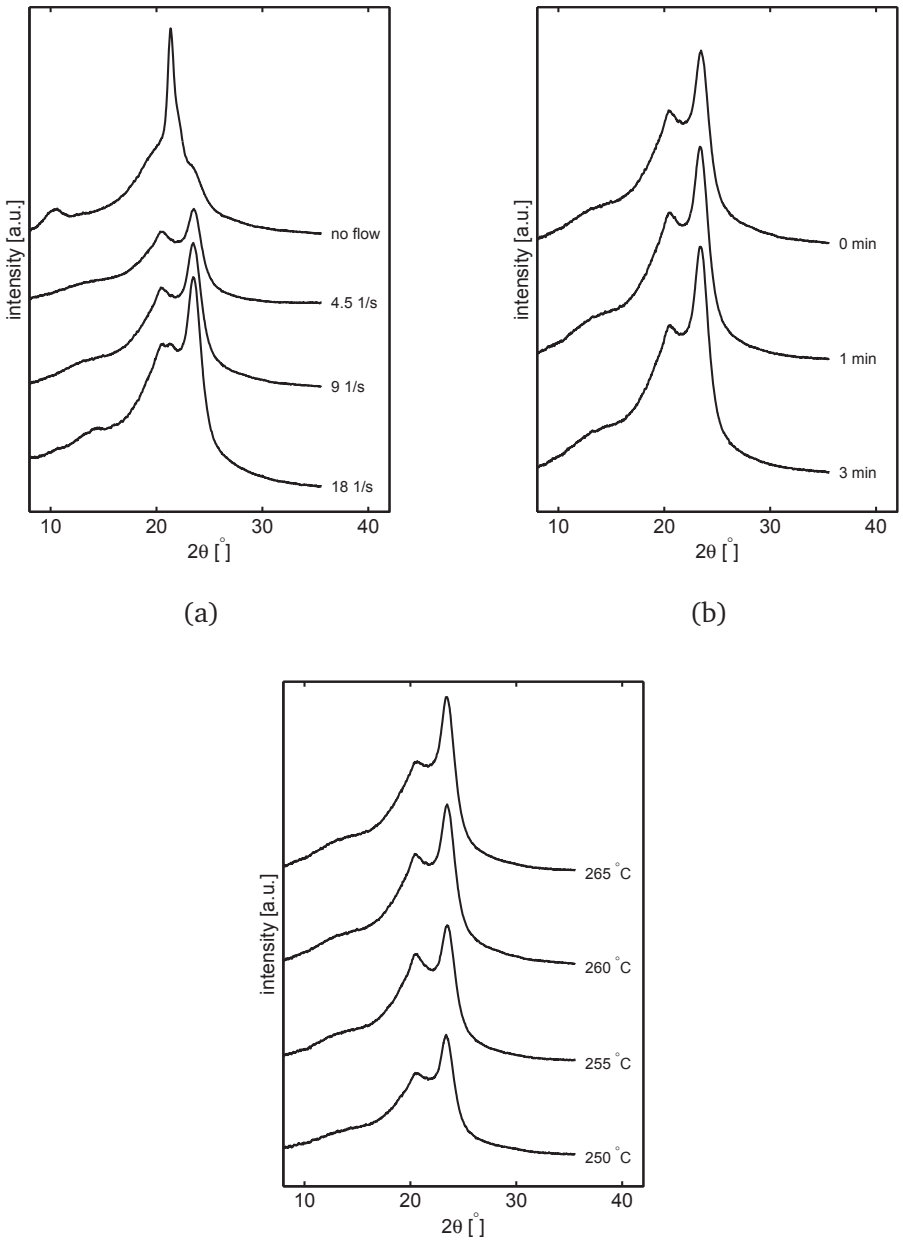

Figure 6.12: Intensity vs scattering angle at 80 °C during second cooling for a sample with intermediate deformation (total strain = 18), with different shear rates (a), delay time after the shear pulse (b), and shear temperature (c). Patterns are shifted along the vertical axis for clarity.

Chapter 7

Conclusions and Recommendations

7.1 Conclusions

This research focused on experimentally determining structural details on the solidification behaviour of semi-crystalline polymers in conditions resembling those found in real life processing. The results are implemented in predictive models that can be used as input for numerical codes for process modelling and for validation of these codes. Advanced experimental methods, such as microfocus X-ray scattering, extended dilatometry and fast scanning chip calorimetry were applied in this work and part of the results serve as a proof of principle for some of these advanced experimental methods.

The main conclusions are:

Microfocus WAXD of polymer crystallized in a FSC

- It is shown, for the first time, that microfocus wide-angle X-ray diffraction with synchrotron radiation can be employed to characterize the phase structure of polymer samples solidified in a fast scanning chip calorimeter.

Primary and secondary crystallization kinetics of m-LLDPE

- Deconvolution of the heat flow signal from combined DSC and FSC can be used to extract the evolution during cooling of the different crystalline fractions of m-LLDPE, i.e. for the primary and two secondary crystallization processes. Primary crystallization was described using functions for nucleation density and spherulitical growth, both measured as function of temperature using SALS.
  To describe the secondary processes a method based on a convolution integral and two rate functions was developed. Good agreement between measurements and model was obtained in a range of 0.07 - 2000 °C/s.

- Using the derivative of the specific volume versus temperature from dilatometry, a DSC-equivalent signal was obtained that includes the influence of flow and pressure. It was shown that flow promotes primary crystallization, while the low-temperature secondary process, producing bundle-like structures, is strongly reduced at the highest flow conditions.
- When the strength of flow is expressed as the dimensionless Weissenberg number, different transition temperatures, indicating the change to another regime for the influence of flow on the crystallization proces, are found for different thermomechanical histories. Nevertheless, the flow-induced crystallization model used is able to capture the measured crystallization kinetics, reasserting the applicability of the stretch criterium selected which governs the onset of flow-induced structure formation.

Flow-induced solidification of high-impact polypropylene

- The extended dilatometry technique required ring shaped samples, which can be processed under well controlled conditions, examined in terms of microstructure using TEM, and tested for mechanical performance using tensile testing.
- During processing, crystallization of the multiple components in heterophasic polypropylene copolymers may hinder or promote each other. Depending on the flow strength, multiple types of morphologies can be formed: the material can either remain unoriented, contain an oriented matrix component with shish-kebab structures, or become fully oriented including deformed modifier particles.
- Highly oriented heterophasic systems do not posses the ability to grow voids upon mechanical deformation, resulting in brittle failure. This clearly shows the importance of the processing step for final product properties, which for multi-phase materials is at least as high as for single-phase homopolymers.

Structure development of LDPE during filmblowing

- Combining blown film extrusion with synchrotron X-ray radiation enables one to acquire a full set of data describing the evolution of crystallinity and crystal orientation along the bubble, in the machine direction.
- Independent of both, the LDPE grade used or the processing conditions selected, the frost-line is observed at about ∼50% space filling. At this position also the final average orientation of the crystallographic c-axis is reached.
- A combination of a moderate M_w in combination with relatively low content of UHM-chains implies relatively high rates of crystallization while, on the other hand, a high molecular weight, as expected, leads to the highest overall orientation level. Also, a high branching content and higher UHM fractions do not speed up crystallization.

- Due to the complexity of the film blowing process, a transient non-isothermal flow enhanced crystallization process with changing non-linear viscoelastic properties, no clear relation between material properties and orientation of the crystallographic axes could be found.

  The memory-effect in PA-6

- The crystallization rate of nascent PA-6 is enhanced with strain only. With applied deformation in the melt, the material gradually shifts from stable γ-form crystallization at lower temperatures towards formation of the stable α-form at higher temperatures and this effect saturates at a critical strain.

7.2 Recommendations

In this thesis, (already) a wide variety of experimental setups was used. Even though, when the author is asked about future recommendations, also a 'wish-list' of possible experiments comes to mind:

- In Chapter 2, the morphology of a sample crystallized in a Flash-DSC 1 was investigated ex-situ using microfocus WAXD. A logical follow-up would be to alter the FSC apparatus such that it allows for high speed in-situ experiments and make full use of the available range of scanning rates. Such an experiment was recently performed by Goderis et al. [238] using a separated sensor environment combined with stroboscopic filtering of the data. Exposure times of 4.7 ms were used to monitor solidification up to 200 °C/s. In case an even more recent and noiseless detector would be used, such as the LAMBDA developed at DESY (Hamburg, Germany), exposure times of 0.5 ms dispensate the need for stroboscopic filtering and allow for investigating even higher cooling rates.

- The aforementioned experiment could provide more insight in the kinetics of secondary crystallization, e.g. such as shown in Chapter 3. In this thesis, a deconvolution method was applied to the heat signal originating from crystallization of m-LLDPE. In-situ microfocus WAXD experiments could provide more details on the type and rate of (secondary) morphology development.

- Chapter 3 provides an extensive characterization of the quiescent crystallization kinetics of an m-LLDPE in a wide range of cooling rates. The rate equation approach to describe secondary crystallization could be further tested for: 1) A different m-LLDPE with higher amount of co-monomer or a different type of co-monomer, 2) a different polymer which also shows secondary crystallization, such as isotactic polypropylene, 3) cooling rates intermediate to those investigated using conventional DSC and Flash-DSC, for example, using HyperDSC.

- A key component in Chapters 3 and 4 is found in the Pirouette dilatometer. The range in possible pressures (100-1200 bar), shear rates (0-180 1/s) and cooling rates (0.1, 1.0, and 90 °C/s) is unique. Nevertheless, an interesting supplement would be to use a hot water bath to flush the apparatus (instead of cold tap water), inducing and intermediate cooling rate in the order of 10 °C/s.
- In Chapter 3, crystallization during flow was observed for the extended dilatometry experiments at the highest shear rates and 5 °C below the pressure corrected melting temperature. These observations need a deeper analysis. For example, the modelling approach taken by Roozemond et. al [239] could be used to tell if this can capture the observed steep increase in the crystallization temperature. Experimentally, one could think of performing more experiments that cover the region above $Wi > 10^4$.
- Using Fourier-transformed infrared spectroscopy (FTIR) could increase understanding on the unusual crystallization behavior of virgin PA-6 discussed in Chapter 6. FTIR allows for careful analyses of the molecular mobility, and is able to distinguish between the occurrence of stable γ-phase crystals and the β-mesophase.

Bibliography

[1] P.C. Painter and M.M. Coleman. *Essentials of Polymer Science and Engineering*, pages 7–9. DEStech Publications, Inc, 2009.

[2] Plastics Europe.

[3] A. Keller. A note on single crystals in polymers: Evidence for a folded chain configuration. *Philosophical Magazine*, 2:1171–1175, 1957.

[4] L. Mandelkern. *Crystallization of Polymers*. McGraw-Hill, New York, 1964.

[5] K. Armitstead, G. Goldbeck-Wood, and A. Keller. *Macromolecules: Synthesis, Order and Advanced properties*, chapter Advances in Polymer Science, Vol. 100/1, pages 219–312. Springer; Berlin, Heidelberg, 1992.

[6] G. Eder and H. Janeschitz-Kriegl. *Processing of Polymers. Materials science and technology: A comprehensive treatment*, volume 18, chapter 5, pages 269–342. Wiley VCH, Weinheim, 1997.

[7] G. Strobl. Crystallization and melting of bulk polymers: New observations, conclusions and a thermodynamic scheme. *Progress in Polymer Science*, 31:398–442, 2006.

[8] J. Ray, W. MacNaughtan, P.S. Chong, J. Vieira, and B. Wolf. The effect of limonene on the crystallization of cocoa butter. *Journal of the Americal Oil Chemists' Society*, 89:437–445, 2012.

[9] D.M. Huong, M. Drechsler, M. Möller, and H.-J. Cantow. Electron spectroscopic imaging of the morphology of in situ polyethylene shish-kebabs. *Journal of Microscopy*, 166:317–328, 1992.

[10] J.W. Housmans, M. Gahleitner, G.W.M. Peters, and H.E.H. Meijer. Structure-property relations in molded, nucleated isotactic polypropylene. *Polymer*, 50:2304–2319, 2009.

[11] C. Schick. Differential scanning calorimetry (DSC) of semicrystalline polymers. *Analytical and Bioanalytical Chemistry*, 395:1589–16111, 2009.

[12] R. Forstner, G.W.M. Peters, and H.E.H. Meijer. A novel dilatometer for PVT measurements of polymers at high cooling - and shear rates. *International Polymer Processing*, 24:114–121, 2009.

[13] G. Portale, D. Cavallo, G.C. Alfonso, D. Hermida-Merino, M. van Drongelen, L. Balzano, G.W.M. Peters, J.G.P. Goossens, and W. Bras. Polymer crystallization studies under processing-relevant conditions at the SAXS/WAXS DUBBLE beamline at the ESRF. *Journal of Applied Crystallography*, 46:1681–1689, 2013.

[14] T.F.J. Pijpers, V.B.F. Mathot, B. Goderis, R.L. Scherrenberg, and E.W. van der Vegte. High-speed calorimetry for the study of the kinetics of (de)vitrification, crystallization, and melting of macromolecules. *Macromolecules*, 35:3601–3613, 2002.

[15] R.L. Danley, P.A. Caulfield, and S.R. Aubuchon. A rapid-scanning differential scanning calorimeter. *Americal Laboratory*, 40:9, 2008.

[16] S.A. Adamovsky, A.A. Minakov, and C. Schick. Scanning microcalorimetry at high cooling rate. *Thermochimica Acta*, 403:55–63, 2003.

[17] A.A. Minakov, D.A. Mordvintsev, and C. Schick. Isothermal reorganization of poly(ethylene terephthalate) revealed by fast calorimetry (1000 Ks^{-1}; 5 ms). *Faraday Discussions*, 128:261–270, 2005.

[18] A.A. Minakov and C. Schick. Ultrafast thermal processing and nanocalorimetry at heating and cooling rates up to 1 MK/s. *Review of Scientific Instruments*, 78:073902, 2007.

[19] V. Mathot, M. Pyda, T. Pijpers, G. vanden Poel, E. van de Kerkhof, S. van Herwaarden, F. van Herwaarden, and A. Leenaers. The Flash DSC 1, a power compensation twin-type, chip-based fast scanning calorimeter (FSC): First findings on polymers. *Thermochimica Acta*, 522:36–45, 2011.

[20] S. van Herwaarden, E. Iervolino, F. van Herwaarden, T. Wijffels, A. Leenaers, and V. Mathot. Design, performance and analysis of thermal lag of the UFS1 twin-calorimeter chip for fast scanning calorimetry using the Mettler-Toledo Flash DSC 1. *Thermochimica Acta*, 522:46–52, 2011.

[21] E. Iervolino, A.W. van Herwaarden, F.G. van Herwaarden, E. van de Kerkhof, P.P.W. van Grinsven, A.C.H.I. Leenaers, V.B.F. Mathot, and P.M. Sarro. Temperature calibration and electrical characterization of the differential scanning calorimeter chip UFS1 for the Mettler-Toledo Flash DSC 1. *Thermochimica Acta*, 522:46–52, 2011.

[22] G. Vanden Poel, D. Istrate, A. Magon, and V. Mathot. Performance and calibration of the Flash DSC 1, a new, MEMS-based fast scanning calorimeter. *Journal of Thermal Analysis and Calorimetry*, 110:1533–1546, 2012.

[23] B. Wunderlich. *Macromolecular Physics, Vol. 2, Crystal Nucleation, Growth, Annealing*. Academic Press, New York, 1976.

[24] D. Turnbull and J.C. Fisher. Rate of nucleation in condensed systems. *Journal of Chemical Physics*, 17:71–73, 1949.

[25] J.A. Koutsky, A.G. Walton, and E. Baer. Nucleation of polymer droplets. *Journal of Applied Physics*, 38:1832–1839, 1967.

[26] H.N. Beck and H.D. Ledbetter. DTA study of heterogeneous nucleation of crystallization of polypropylene. *Journal of Applied Polymer Science*, 9:2131–2141, 1965.

[27] Q. Zia, R. Androsch, H.-J. Radusch, and S. Piccarolo. Morphology, reorganization, and stability of mesomorphic nanocrystals in isotactic polypropylene. *Polymer*, 2006:8163–8172, 47.

[28] C.C. Hsu, P.H. Geil, H. Miyaji, and K. Asai. Structure and properties of polypropylene crystallized from the glassy state. *Journal of Polymer Science, Part B: Physics*, 24:2379–2401, 1986.

[29] G. Natta and P. Corradini. Structure and properties of isotactic polypropylene. *Nuovo Cimento Supplemento*, 15:40–51, 1960.

[30] A. Ziabicki. Über die mesomorphe β-form von polycapronamic und ihre umwandlung in die kristalline form α. *Kolloid-Zeitschrift*, 167:132–141, 1959.

[31] S. Piccarolo. Morphological changes in isotactic polypropylene as a function of cooling rate. *Journal of Macromolecular Science, (Physics)*, 31:501–511, 1992.

[32] V. Brucato, S. Piccarolo, and V. La Carrubba. An experimental methodology to study polymer crystallization under processing conditions. The influence of high cooling rates. *Chemical Engineering Science*, 57:4129–4143, 2002.

[33] D. Cavallo, F. Azzurri, R. Floris, G.C. Alfonso, L. Balzano, and G.W. Peters. Continuous cooling curves diagrams of propene/ethylene random copolymers. The role of ethylene counits in mesophase developments. *Macromolecules*, 43:2890–2896, 2010.

[34] D. Cavallo, G. Portale, L. Balzano, F. Azzurri, W. Bras, G.W. Peters, and G.C. Alfonso. Real-time WAXD detection of mesophase development during quenching of propene/ethylene copolymers. *Macromolecules*, 43:10208–10212, 2010.

[35] D. Mileva, D. Cavallo, L. Gardella, G.C. Alfonso, G. Portale, L. Balzano, and R. Androsch. In situ X-ray analysis of mesophase formation in random copolymers of propylene and 1-butene. *Polymer Bulletin*, 67:497–510, 2011.

[36] D. Cavallo, L. Gardella, G.C. Alfonso, G. Portale, L. Balzano, and R. Androsch. Effect of cooling rate on the crystal/mesophase polymorphism of polyamide 6. *Colloid Polymer Science*, 289:1079–1079, 2011.

[37] F. De Santis, S. Adamovsky, G. Titomanlio, and C. Schick. Isothermal nanocalorimetry of isotactic polypropylene. *Macromolecules*, 40:9026–9031, 2007.

[38] F. De Santis, S. Adamovsky, G. Titomanlio, and C. Schick. Scanning nanocalorimetry at high cooling rate of isotactic polypropylene. *Macromolecules*, 39:2562–2567, 2006.

[39] I. Kolesov, D. Mileva, R. Androsch, and C. Schick. Structure formation of polyamide 6 from the glassy state by fast scanning chip calorimetry. *Polymer*, 52:5156–5165, 2011.

[40] D. Mileva, R. Androsch, E. Zhuravlev, and C. Schick. Morphology of mesophase and crystals of polyamide 6 prepared in a fast scanning chip calorimeter. *Polymer*, 53:3994–4007, 2012.

[41] D. Mileva, I. Kolesov, and R. Androsch. Morphology of cold-ordered polyamide 6. *Colloid Polymer Science*, 290:971–978, 2012.

[42] M. Kyotani and S. Mitsuhashi. Studies on crystalline forms of nylon 6. II. Crystallization from the melt. *Journal of Polymer Science, Part A-2: Polymer Physics*, 10:1497–1508, 1972.

[43] D. Mileva, R. Androsch, D. Cavallo, and G.C. Alfonso. Structure formation of random isotactic copolymers of propylene and 1-hexene or 1-octene at rapid coolings. *European Polymer Journal*, 48:1082–1092, 2012.

[44] E. J. Addink and J. Beintema. Polymorphism of crystalline polypropylene. *Polymer*, 2:185–193, 1961.

[45] G.E. Ashby and D.F. Hoeg. Concerning the measurement of isotacticity in propylene polymers. *Journal of Polymer Science, Part C: Polymer Letters*, 19:535–538, 1959.

[46] D. Mileva, A. Monami, D. Cavallo, G.C. Alfonso, G. Portale, and R. Androsch. Crystallization of a polyamide 6/montmorillonite nanocomposite at rapid cooling. *Macromolecular Material Engineering*, 298:938–943, 2013.

[47] F. Auriemma, V. Petraccone, L. Parravicini, and P. Corradini. Mesomorphic form (β) of Nylon 6. *Macromolecules*, 30:7554–7559, 1997.

[48] L.G. Roldan and H.S. Kaufman. Crystallization of Nylon 6. *Journal of Polymer Science, Part C: Polymer Letters*, 1963:603–608, 1963.

[49] G. Gurato, A. Fichera, F.Z. Grandi, R. Zannetti, and P. Canal. Crystallinity and polymorphism of 6-polyamide. *Die Markomolekulare Chemie*, 175:953–975, 1974.

[50] D.R. Holmes, C.W. Bunn, and D.J. Smith. The crystal structure of polycaproamide: Nylon 6. *Journal of Polymer Science*, 17:159–177, 1955.

[51] A. Arndt. *Handbook of Thermoplastics*, chapter 1, pages 1–57. Marcel Dekker, 1997.

[52] D.L. Wilfong and G.W. Knight. Crystallization mechanisms for LLDPE and its fractions. *Journal of Polymer Science, Part B: Polymer Physics*, 28:861–870, 1990.

[53] S. Bensason, J. Minick, A. Moet, S. Chum, A. Hiltner, and E. Baer. Classification of homogeneous ethylene-octene copolymers based on comonomer content. *Journal of Polymer Science, Part B: Polymer Physics*, 34:1301–1315, 1996.

[54] M.Y. Gelfer and H.H. Winter. Effect of branch distribution on rheology of LLDPE during early stages of crystallization. *Macromolecules*, 32:8974–8981, 1999.

[55] K. Jokela, A. Väänänen, M. Torkkeli, P. Starck, R. Serimaa, B. Löfgren, and J. Seppälä. Differential scanning calorimetry, small-angle x-ray scattering, and wide-angle x-ray scattering on homogeneous and hetereogeneous ethylene-alpha-copolymers. *Journal of Polymer Science, Part B: Polymer Physics*, 39:1860–1875, 2001.

[56] H. Wen, H. Li, S. Xu, S. Xiao, H. Li, S. Jiang, L. An, and Z. Wu. Shear effects on crystallization behavior of poly(ehtylene-co-octene) copolymers. *Journal of Polymer Resins*, 19, 2012.

[57] H.G. Zachmann and H.A. Stuart. Schmelz- und kristallisationserscheinungen bei makromolekularen substanzen. *Die Makromolekulare Chemie*, 41:131–147, 1960.

[58] A. Alizadeh, L. Richardson, J. Xu, S. McCartney, H. Marand, Y.W. Cheung, and S. Chum. Influence of structural and topological constraints on the crystallization and melting behavior of polymers. 1. ethylene/1-octene copolymers. *Macromolecules*, 32:6221–6235, 1999.

[59] S. Vanden Eynde, V.B.F. Mathot, M.H.J. Koch, and H. Reynaers. Thermal behaviour and morphology of homogeneous ethylene-1-octene copolymers with high comonomer contents. *Polymer*, 41:4889–4900, 2000.

[60] B. Goderis, H. Reynaers, and M.H.J. Koch. Primary and secondary crystallization in a homogeneous ethylene-1-octene copolymer: Crystallinity heterogeneity studied by SAXS. *Macromolecules*, 35:5840–5853, 2002.

[61] O. Tavichai, L. Feng, and M.R. Kamal. Crystalline spherulitic growth kinetics during shear for linear low-density polyethylene. *Polymer Engineering and Science*, DOI 10.1002 pen.20608:1468–1475, 2006.

[62] T. Sedlacek, M. Zatloukal, P. Filip, A. Boldizar, and P. Saha. On the effect of pressure on the shear and elongational viscosities of polymer melts. *Polymer Engineering and Science*, 44:1328–1337, 2004.

[63] E.S. Carreras, N. El Kissi, J.M. Piau, F. Toussaint, and S. Nigen. Pressure effects on viscosity and flow stability of polyethylene melts during extrusion. *Rheologica Acta*, 45:209–222, 2006.

[64] K. Nakamura, K. Katayama, and T. Amano. Some aspects of nonisothermal crystallization in polymers. II. Consideration of the isokinetic condition. *Journal of Applied Polymer Science*, 17:1031–1041, 1973.

[65] V. La Carrubba, V. Brucato, and S. Piccarolo. Phenomenological approach to compare the crystallization kinetics of isotactic polypropylene and polyamide-6 under pressure. *Journal of Polymer Science, Part B: Polymer Physics*, 40:153–175, 2002.

[66] R.M. Patel. Crystallization kinetics modeling of high density and linear low density polyethylene resins. *Journal of Applied Polymer Science*, 124:1542–1552, 2012.

[67] M. Avrami. Kinetics of phase change. I. General Theory. *Journal of Chemical Physics*, 7:1103–1112, 1939.

[68] M. Avrami. Kinetics of phase change. II. Transformation-time relations for random distribution of nuclei. *Journal of Chemical Physics*, 8:212–224, 1940.

[69] G. Lamberti. Isotactic polypropylene crystallization: Analysis and modeling. *European Polymer Journal*, 47:1097–1112, 2011.

[70] I.H. Hillier. Modified Avrami equation for the bulk crystallization kinetics spherulitic polymers. *Journal of Polymer Science, Part A: Polymer Chemistry*, 3:3067–3078, 1965.

[71] F.C. Perez-Cardenas, L. Felipe del Castillo, and R. Vera-Graziano. Modified Avrami expression for polymer crystallization kinetics. *Journal of Applied Polymer Science*, 43:779–782, 1991.

[72] V. Hinrichs, G. Kalinka, and G. Hinrichsen. An Avrami-Based model for the description of the secondary crystallization of polymers. *Journal of Macromolecular Science, Part B: Physics*, 35:295–302, 1996.

[73] T.B. van Erp, P.C. Roozemond, and G.W.M. Peters. Flow-enhanced crystallization kinetics of iPP during cooling at elevated pressure: Characterization, validation, and development. *Macromolecular Theory and Simulations*, 22:309–318, 2013.

[74] A. Mamum, X. Chen, and R.G. Alamo. Interplay between a strong memory effect of crystallization and liquid-liquid phase separation in melts of broadly distributed ethylene-1-alkene copolymers. *Macromolecules*, 47:7958–7970, 2014.

[75] K. Nishida. Rapid temperature jump stage for optical microscope. In *Proceedings of PPS-24, Salerno, Italy*, 2008.

[76] R.S. Stein and M.B. Rhodes. Photographic light scattering by polyethylene film. *Journal of Applied Physics*, 31:1873–1884, 1960.

[77] J.W. Housmans, L. Balzano, M. Adinolfi, G.W.M. Peters, and H.E.H. Meijer. Dilatometry: A tool to measure the influence of cooling rate and pressure on the phase behavior of nucleated polypropylene. *Macromolecular Materials and Engineering*, 294:231–243, 2009.

[78] M. Sentmanat. Miniature universal testing platform: from extensional melt rheology to solid-state deformation behaviour. *Rheologica Acta*, 43:657Ű669, 2004.

[79] D.C. Bassett and A.M. Hodge. On the morphology of melt-crystallized polyethylene I. Lamellar profiles. *Proceedings of the Royal Society of London. Series A, Mathematical and Physical*, 377:25–37, 1981.

[80] D.C. Bassett, A.M. Hodge, and R.H. Olley. On the morphology of melt-crystallized polyethylene II. Lamellae and their crystallization conditions. *Proceedings of the Royal Society of London. Series A, Mathematical and Physical*, 377:39–60, 1981.

[81] D.C. Bassett and A.M. Hodge. On the morphology of melt-crystallized polyethylene III. Spherulite organization. *Proceedings of the Royal Society of London. Series A, Mathematical and Physical*, 377:61–71, 1981.

[82] M. van Drongelen, T.B. van Erp, and G.W.M. Peters. Quantification of non-isothermal, multi-phase crystallization of isotactic polypropylene: the influence of cooling rate and pressure. *Polymer*, 53:4758–4769, 2012.

[83] R. Kolb, C. Wutz, N. Stribeck, G. von Krosigk, and C. Riekel. Investigation of secondary crystallization of polymers by means of microbeam X-ray scattering. *Polymer*, 42:5257–5266, 2001.

[84] Y. Akpalu, L. Kielhorn, B.S. Hsiao, R.S. Stein, T.P. Russell, J. van Egmond, and M. Muthukumar. Structure development during crystallization of homogeneous copolymers of ethene and 1-octene: time resolved synchrotron X-ray and SALS measurements. *Macromolecules*, 32:765–770, 1999.

[85] S. Rabiej. The influence of side branches on the structure of crystalline phase in ethylene-1-alkene copolymers. *European Polymer Journal*, 41:393–402, 2005.

[86] E. Tarasova, T. Poltimäe, A. Krumme, A. Lehtinen, and A. Viikna. Study of very low temperature crystallization process in ethylene/alpha-olefin copolymers. *Macromolecular Symposia*, 282:175–184, 2009.

[87] J.D. Hoffman and R.L. Miller. Kinetic of crystallization from the melt and chain folding in polyethylene fractions revisited: theory and experiment. *Polymer*, 38(13):3151 – 3212, 1997.

[88] V.B.F. Mathot and M.F.J. Pijpers. Heat capacity, enthalpy and crystallinity for a linear polyethylene obtained by DSC. *Journal of Thermal Analysis and Calorimetry*, 28:349–358, 1983.

[89] V.B.F. Mathot. Temperature dependence of some thermodynamic function for amorphous and semi-crystalline polymers. *Polymer*, 25:579–599, 1984.

[90] K. Søndergaard, P. Minà, and S. Piccarolo. Wide-range cooling characteristics of a selected isotactic polypropylene. *Journal of Macromolecular Science, Part B: Physics*, 36:733–747, 1997.

[91] K.M. Bernland. *Nucleating and clarifying polymers*. PhD thesis, ETH Zurich, 2010.

[92] S. Acierno and P. van Puyvelde. Effect of short chain branching upon the crystallization of model polyamides-11. *Polymer*, 46:10331–10338, 2005.

[93] P. Debye and A.M. Bueche. Scattering by an inhomogeneous solid. *Journal of Applied Physics*, 20:518–525, 1949.

[94] S.B. Clough, R.S. Stein, and C. Picot. Low-angle light-scattering equations for polymer spherulites. *Journal of Polymer Science, Part A-2: Polymer Physics*, 9:1147–1148, 1971.

[95] R.J. Samuels. Small-angle light scattering from optically anisotropic spheres and disks. Theory and experimental Verification. *Journal of Polymer Science: Part A-2*, 9:2165–2246, 1971.

[96] R.J. Samuels. Small-angle light scattering and crystallization processes in solid polymers films. *Journal of Polymer Science: Polymer Physics Edition*, 12:1417–1439, 1974.

[97] J. M. Haudin. *Optical Studies of Polymer Morphology*, chapter Optical Properties of Polymers. Elsevier Applied Science Publishers, 1986.

[98] Z. Ding and J.E. Spruiell. An experimental method for studying nonisothermal crystallization of polymers at very high cooling rates. *Journal of Polymer Science, Part B: Polymer Physics*, 34:2783–2803, 1996.

[99] R.P. Patki and P.J. Philips. Crystallization kinetics of linear polyethylene: The maximum in crystal growth rate-temperature dependence. *European Polymer Journal*, 44:534–541, 2008.

[100] G. Eder, P. Hierzenberger, and P. Amorim. Pressure effects on polymer crystal nucleation. In *Workshop on polymer crystallization under conditions relevant to processing*, pages –, Genova (Italy), May 2010.

[101] J. Wagner and P.J. Philips. The mechanism of crystallization of linear polyethylene, and its copolymers with octene, over a wide range of supercoolings. *Polymer*, 42:8999–9013, 2001.

[102] W. Schneider, A. Koppl, and J. Berger. Non-isothermal crystallization. System of rate equations. *International Polymer Processing*, 2:151–154, 1988.

[103] P. Jerschow and H. Janeschitz-Kriegl. The role of long molecules and nucleating agents in shear induced crystallization of isotactic polypropylenes. *International Polymer Processing*, 12:72–77, 1997.

[104] F. P. Incropera, D.P. DeWitt, T.L. Bergman, and A. S. Lavine. *Introduction to Heat Transfer*. John Wiley & Sons, New York, 2007.

[105] G. Lamberti. Flow-induced crystallization during isotactic polypropylene film casting. *Polymer Engineering and Science*, 51:851–861, 2011.

[106] M.H.E. van der Beek, G.W.M. Peters, and H.E.H. Meijer. Influence of shear flow on the specific volume and the crystalline morphology of isotactic polypropylene. *Macromolecules*, 39:1805–1814, 2006.

[107] J. He and P. Zoller. Crystallization of polypropylene, nylon-66 and poly(ehtylene terephthalate) at pressurs to 200 MPa: kinetics and characterization of products. *Journal of Polymer Science, Part B: Polymers Physics*, 32:1049–1067, 1994.

[108] J. van Meerveld, G. W. M. Peters, and M. Hütter. Towards a rheological classification of flow induced crystallization experiments of polymer melts. *Rheologica Acta*, 44:119–134, 2004.

[109] J.W. Housmans, G.W.M. Peters, and H.E.H. Meijer. Flow-induced crystallization of propylene/ethylene random copolymers. *Journal of Thermal Analysis and Calorimetry*, 98:693–705, 2009.

[110] P.C. Roozemond, Z. Ma, K. Cui, L. Li, and G.W.M. Peters. Multimorphological crystallization of shish-kebab structures in isotactic polypropylene: Quantitative modeling of parent-daughter crystallization kinetics. *Macromolecules*, 47:5152–5162, 2014.

[111] R.J.A. Steenbakkers and G.W.M. Peters. A stretch-based model for flow-enhanced nucleation of polymer melts. *Journal of Rheology*, 55:401–433, 2011.

[112] W.M.H. Verbeeten, G.W.M. Peters, and F.P.T. Baaijens. Viscoelastic analysis of complex polymer melt flows using the extended pom-pom model. *Journal of Non-Newtonian Fluid Mechanics*, 108:301–326, 2002.

[113] R. Cardinaels, P. van Puyvelde, and P. Moldenaers. Evaluation and comparison of routes to obtain pressure coefficients from high-pressure capillary rheometry data. *Rheologica Acta*, 46:495–505, 2007.

[114] T.B. van Erp, L. Balzano, A.B. Spoelstra, L.E. Govaert, and G.W.M. Peters. Quantification of non-isothermal, multi-phase crystallization of isotactic polypropylene: the influence of shear and pressure. *Polymer*, 53:5896–5908, 2013.

[115] F.J.M.F. Custódio, R.J.A. Steenbakkers, P.D. Anderson, G.W.M. Peters, and H.E.H. Meijer. Model development and validation of crystallization behaviour in injection molding prototype flows. *Macromolecular Theory and Simulations*, 18:469–494, 2009.

[116] P.C. Roozemond, R.J.A. Steenbakkers, and G.W.M. Peters. A model for flow-enhanced nucleation based on fibrillar dormant precursors. *Macromolecular Theory and Simulations*, 20:93–109, 2011.

[117] C.W. Macosko. *Rheology, principles, measurements and application*. Wiley-VCH, New York, 1994.

[118] P. Galli and J.C. Haylock. Advances in Ziegler-Natta polymerization - unique polyolefin copolymers, alloys and blends made directly in the reactor. *Makromolekulare Chemie. Macromolecular Symposia*, 63:19–54, 1992.

[119] G. Cecchin, G. Morini, and A. Pelliconi. Polypropylene product innovation by reactor granule technology. *Macromolecular Symposia*, 173:195–209, 2001.

[120] C. Grein, K. Bernreitner, A. Hauer, M. Gahleitner, and W. Neißl. Impact modified isotactic polypropylene with controlled rubber intrinsic viscosities: Some new aspects about morphology and fracture. *Journal of Applied Polymer Science*, 87:1702–1712, 2003.

[121] F. Coppola, R. Greco, E. Martuscelli, H.W. Kammer, and C. Kummerlowe. Mechanical properties and morphology of isotactic propropylene/ethylene-propylene copolymer blends. *Polymer*, 28:47–56, 1987.

[122] M. Gahleitner, A. Hauer, K. Bernreitner, and E. Ingolic. Polypropylene-based model compounds as tools for the development of high-impact ethylene-propylene copolymers. *International Polymer Processing*, 17:318–324, 2002.

[123] P.L. Li, B. Yi, and M.B. Yang. Morphology prediction and the effect of core-shell structure on the rheological behavior of PP/EPDM/HDPE blends. *Polymer Engineering and Science*, 51:2425–2433, 2011.

[124] Y. Chen and L. Ye. Structure and properties of PP/POE/HDPE blends. *Journal of Applied Polymer Science*, 121:1013–1022, 2011.

[125] C. Kock, M. Gahleitner, A. Schausberger, and E. Ingolic. Polypropylene/polyethylene blends as models for high-impact propylene-ethylene copolymers, Part 1: Interaction between rheology and morphology. *Journal of Applied Polymer Science*, 128:1484–1496, 2012.

[126] S. Bakshi, A. K. Kulshreshtha, B.P. Singh, and J.S. Anand. Stress-whitening of polypropylene block copolymer in impact tests and its measurement. *Polymer Testing*, 8:191–199, 1989.

[127] R. Gensler, C.J.G. Plummer, C. Grein, and H.H. Kausch. Influence of the loading rate on the fracture resistance of isotactic polypropylene and impact modified isotactic polypropylene. *Polymer*, 41:3809–3819, 2000.

[128] T. Koch and D. Machl. Evaluation of scratch resistance in multiphase PP blends. *Polymer Testing*, 26:927–938, 2007.

[129] P. Doshev, R. Lach, G. Lohse, A. Heuvelsland, W. Grellmann, and H.J. Radusch. Fracture characteristics and deformation behavior of heterophasic ethylene-propylene copolymers as a function of the dispersed phase composition. *Polymer*, 46:9411–9422, 2005.

[130] C. Grein, M. Gahleitner, B. Knogler, and S. Nestelberger. Melt viscosity effects in ethylene-propylene copolymers. *Rheologica Acta*, 46:1083–1089, 2007.

[131] J. Karger-Kocsis and I. Csikai. Skin-core morphology and failure of injection-molded specimens of impact modified polypropylene blends. *Polymer Engineering Science*, 27:241–253, 1987.

[132] Y. Marchal, B. Oldenhove, D. Daost, R. Legras, and F. Delannay. Characterization of the fracture toughness of rubber-toughened polypropylene. *Polymer Engineering Science*, 38:2063–2071, 1998.

[133] R. Pantani and G. Titomanlio. Description of PVT behavior of an industrial polypropylene-EPR copolymer in process conditions. *Journal of Applied Polymer Science*, 81:267–278, 2001.

[134] G.J. Zhong and Z.M. Li. Injection molding-induced morphology of thermoplastic polymer blends. *Polymer Engineering Science*, 45:1655–1665, 2005.

[135] R. Pantani, L. Balzano, and G.W.M. Peters. Flow-induced morphology of iPP solidified in a shear device. *Macromolecular Material Engineering*, 296:740–754, 2011.

[136] J.W. Housmans, R.J.A. Steenbakkers, P.C. Roozemond, G.W.M. Peters, and H.E.H. Meijer. Saturation of pointlike nuclei and the transition to oriented structures in flow-induced crystallization of isotactic polypropylene. *Macromolecules*, 42:5728–5740, 2009.

[137] R. Forstner, G.W.M Peters, C. Rendina, J.W. Housmans, and H.E.H. Meijer. Volumetric rheology of polymers: the influence of shear flow, cooling rate, and pressure on the specific volume of iPP and P/E random copolymers. *Journal of Thermal Analysis and Calorimetry*, 98:683–691, 2009.

[138] T.B. van Erp, L.E. Govaert, and G.W.M. Peters. Mechanical performance of injection-molded polypropylene: Characterization and modeling. *Macromolecular Material Engineering*, 298(3):348–358, 2012.

[139] D. Montezinos, B.G. Wells, and J.L. Burns. Use of ruthenium in hypochlorite as a stain for polymeric materials. *Journal of Polymer Science. Polymer Letters Edition*, 23:421–425, 1985.

[140] I.M. Ward. *Mechanical properties of solid polymers*. Wiley & Sons, New York, 1983.

[141] C. Kock, M. Aust, C. Grein, and M. Gahleitner. Polypropylene/polyethylene blends as models for high-impact propylene-ethylene copolymers. 2: Relation between composition and mechanical performance. *Journal of Applied Polymer Science*, 130:287–296, 2013.

[142] M.H.E. van der Beek, G.W.M. Peters, and H.E.H. Meijer. A dilatometer to measure the influence of cooling rate and melt shearing on specific volume. *International Polymer Processing*, 20:111–120, 2005.

[143] F.C. Stehling, T. Huff, and C.S. Speed. Structure and properties of rubber-modified polypropylene impact blends. *Journal of Applied Polymer Science*, 26:2693–2711, 1981.

[144] G.M. Kim and G.H. Michler. Micromechanical deformation processes in toughened and particle-filled semicrystalline polymers: Part 1. Characterization of deformation processes in dependence on phase morphology. *Polymer*, 39:5689–5697, 1998.

[145] R. Zacur, G. Goizueta, and N. Capiati. Dispersed phase morphology of impact PP copolymers. Effects of Blend composition as determined by TREF. *Polymer Engineering and Science*, 40:1921–1930, 2000.

[146] A. Vananroye, R. Cardianels, P. van Puyvelde, and P. Moldenaers. Effect of confinement and viscosity ratio on the dynamics of single droplets during transient shear flow. *Journal of Rheology*, 52:1459–1475, 2008.

[147] J.C. Wittmann and B. Lotz. Epitaxial crystallization of polymers on organic and polymeric substrates. *Progress in Polymer Science*, 15:909–948, 1990.

[148] Y. Nishioa, T. Yamanea, and T. Takahashi. Crystallization behavior of high-density polyethylene in an oriented blend with polypropylene. *Journal of Macromolecular Science, Part B: Physics*, 23:17–27, 1984.

[149] X.M. Zhang and A. Ajji. Oriented structure of PP/LLDPE multilayer and blends films. *Polymer*, 46:3385–3393, 2005.

[150] B. O. Reid, M. Vadlamudi, A. Mamum, H. Janani, H. Gao, W. Hu, and R.G. Alamo. Strong memory effect of crystallization above the equilibrium melting point of random copolymers. *Macromolecules*, 46:6485–6497, 2013.

[151] C.B. Bucknall. *Toughened Plastics*. Applied Science, 1977.

[152] G.M. Kim and G.H. Michler. Micromechanical deformation processes in toughened and particle-filled semicrystalline polymers: Part 2. Merperodel representation for micromechanical deformation processes. *Polymer*, 39:5699–5703, 1998.

[153] G.M. Kim. *Analyse der Schleagzahigkeitsmechanismen in abhengigkeit von der morpholog von modifizierten teilkristallinen polymeren*. PhD thesis, Martin-Luther-University, Halle-Wittenberg University, Germany, 1996.

[154] B.A.G. Schrauwen, L.C.A. van Breemen, A.B. Spoelstra, L.E. Govaert, G.W.M. Peters, and H.E.H. Meijer. Structure, deformation, and failure of flow-oriented semicrystalline polymers. *Macromolecules*, 37:8618–8633, 2004.

[155] T.B. van Erp, D. Cavallo, G.W.M. Peters, and L.E. Govaert. Rate-, temperature-, and structure-dependent yield kinetics of isotactic polypropylene. *Journal of Polymer Science, Part B: Polymer Physics*, 50:1438–1451, 2012.

[156] H. Janeschitz-Kriegl. *Crystallization modalities in polymer melt processing: Fundamental aspects of structure formation*. Springer, New York, 2009.

[157] Z. Bartczak, A. Galeski, A.S. Argon, and R.E. Cohen. On the plastic deformation of the amorphous component in semicrystalline polymers. *Polymer*, 37:2113–2123, 1996.

[158] R.H. Somani, B.S. Hsiao, A. Nogales, S. Srinivas, A.H. Tsou, I. Sics, F.J. Balta-Calleja, and T.A. Ezquerra. Structure development during shear flow induced crystallization of i-PP: In situ small-angle X-ray diffraction study. *Macromolecules*, 33:9385–9394, 2000.

[159] J.M. Schultz. *Polymer Crystallization. The development of crystalline order in thermoplastic polymers.* Oxford University Press, Oxford, 2001.

[160] R.H. Somani, L. Yang, L. Zhu, and B.S. Hsiao. Flow-induced shish-kebab precursor structures in entangled polymer melts. *Polymer*, 46:8587–8623, 2005.

[161] J. Lu, H. Sue, and T.P. Rieker. Morphology and mechanical property relationship in linear low-density polyethylene blown films. *Journal of Materials Science*, 35:5169–5178, 2000.

[162] Z. Horvath, A. Manyhard, P. Doshev, M. Gahleitner, G. Voros, J. Varga, and B. Pukanszky. Effect of the molecular structure of the polymer and nucleation on the optical properties of polypropylene homo- and copolymers. *Applied Materials and Interfaces*, 6:7456–7463, 2014.

[163] A. Keller and M.J. Machin. Oriented crystallization in polymers. *Journal of Macromolecular Science, (Physics)*, B1(1):41–91, 1967.

[164] X.M. Zhang, S. Elkoun, A.A. Ajji, and M.A. Huneault. Oriented structure and anisotropy properties of polymer blown films: HDPE, LLDPE and LDPE. *Polymer*, 45:217–229, 2004.

[165] C. Silvestre, S. Cimmino, M. Raimo, D. Duraccio, B. del Amo Fernandez, P. Lafuente, and V. Leal Sanz. Structure and Morphology Development in Films of mLLDPE/LDPE Blends During Blowing. *Macromolecular Materials and Engineering*, 291:1477–1485, 2006.

[166] A. Keller and H.W.H. Kolnaar. *Flow-induced orientation and structure formation*, chapter 4, pages 189–266. Wiley VCH, 1997.

[167] R.J. Pazur and R.E. Prud'homme. X-ray pole figure and small angle scattering measurements on tubular blown low-density poly(ethylene) films. *Macromolecules*, 29:119–128, 1996.

[168] A. Ajji, X. Zhang, and S. Elkoun. Biaxial orientation in HDPE films: comparison of infrarer spectroscopy, X-ray pole figures and birefringence techniques. *Polymer*, 46:3838–3846, 2005.

[169] A. Ghaneh-Fard. Effects of film blowing conditions on molecular orientation and mechanical properties of polyethylene films. *Journal plastic film & sheeting*, 15:194–218, 1999.

[170] M. van Gurp, B.J. Kip, J.P.C. van Heel, and S. de Boer. On the development of orientation in LDPE blown films. *Journal of Plastic Film & Sheeting*, 10:156–176, 1994.

[171] C.J.S. Petrie. A comparision of theoretical prediction with published experimental measurments on the blown film process. *American Institue of Chemical Engineers Journal*, 21:275–282, 1975.

[172] X-L. Luo and R.I. Tanner. A computer study of film blowing. *Polymer Engineering and Science*, 25:620–629, 1985.

[173] I.A. Muslet and M.R. Kamal. Computer simulation of the film blowing process incorporating crystallization and viscoelasticity. *Journal of Rheology*, 48:525–550, 2004.

[174] S. Sarafrazi and F. Sharif. Non-Isothermal simulation of the film blowing process using multi-mode eXtended pom-pom model. *International Polymer Processing*, 23:30–37, 2008.

[175] J.S. Lee, H.W. Jung, and J.C. Hyun. Transient solutions of nonlinear dynamics in film blowing process accompanied by on-line crystallization. *Journal of Rheology*, 55:257–271, 2011.

[176] A.K. Doufas. A microstructural flow-induced crystallization model for film blowing: validation with experimental data. *Rheologica Acta*, 53:269–293, 2014.

[177] M.D. Bullwinkel, G.A. Campbell, D.H. Rasmussen, J. Krexa, and C.J. Brancewitz. Crystallization studies of LLDPE during tubular blown film processing. *International Polymer Processing*, 16:39–47, 2001.

[178] G. Gururajan and A.A. Ogale. Molecular orientation evolution during low-density polyethylene blown film extrusion using real-time raman spectroscopy. *Journal of Raman Spectroscopy*, 40:212–217, 2009.

[179] A. Ghaneh-Fard, P.J. Carreau, and P.G. Lafleur. On-line birefringence measurement in film blowing of a linear low density polyethylene. *International Polymer Processing*, 12:136–146, 1996.

[180] G. Gururajan, H. Shan, G. Lickfield, and A.A. Ogale. Real-time wide-angle X-ray diffraction during polyethylene blown film extrusion. *Polymer Engineering and Science*, 48:1487–1494, 2008.

[181] G. Gururajan and A.A. Ogale. Real-time crystalline orientation measurements during low-density polyethylene blown film extrusion using wide-angle X-ray diffraction. *Polymer Engineering and Science*, 52:1532–1536, 2012.

[182] W. Bras. An saxs/waxs beamline at the esrf and future experiments. *Journal of Macromolecular Science, Part B: Physics*, 37:557–565, 1998.

[183] M. Sentmanat, B.N. Wang, and G.H. McKinley. Measuring the transient extensional rheology of polyethylene melts using the SER universal testing platform. *Journal of Rheology*, 49:585–606, 2005.

[184] Verband Deutscher Maschinen und Anlagenbau. *Kenndaten für die verarbeitung thermoplastischer kunststoffe, Teil 1, Thermodynamik*. Hansenm München, 1979.

[185] W. Bras, I.P. Dolbnya, D. Detollenare, R. van Tol, M. Malfois, G.N. Greaves, A.J. Ryan, and E. Heeley. Recent experiments on a combined small-angle/wide-angle X-ray scattering beam line at the ESRF. *Journal of Applied Crystallography*, 36:791–794, 2003.

[186] J.J. Hermans, D. Vermaas P.H. Hermans, and A. Weidinger. Quantitative evaluation of orientation in cellulose fibres from the X-ray fibre diagram. *Recueil des Travaux Chimiques des Pays-Bas*, 64:427–427, 1946.

[187] R.S. Stein and F.H. Norris. The X-ray diffraction, birefringence, and infrared dichroism of streched polyethylene. *Journal of Polymer Science*, 21:381–396, 1958.

[188] P.H. Lindenmeyer and S. Lustig. Crystallite orientation in extruded polyethylene film. *Journal of Applied Polymer Science*, 9:227–240, 1965.

[189] S. Rastogi, Y. Yao, S. Ronca, J. Bos, and J. van der Eem. Unprecedented high-modulus high-strength tapes and films of ultrahigh molecular weight polyethylene via solvent-free route. *Macromolecules*, 44:5558–5568, 2011.

[190] Z.W. Wilchinsky. Measurement of orientation in polypropylene film. *Journal of Applied Physics*, 31p:1969–1972, 1960.

[191] H. Zuidema, G.W.M. Peters, and H.E.H. Meijer. Development and validation of a recoverable strain-bases model for flow-induced crystallization of polymers. *Macromolecular Theory and Simulations*, 10:447–460, 2001.

[192] P.P. Tas. *Film blowing: From polymer to product*. PhD thesis, Eindhoven University of Technology, 1994.

[193] W.F. Maddams and J.E. Preedy. X-ray diffraction orientation studies on blown polyethylene films. III. High-stress crystallization orientation. *Journal of Applied Polymer Science*, 22:2751–2759, 1978.

[194] J. Lu and H. Sue. Characterization of crystalline texture of LLDPE blown films using X-ray pole figures. *Macromolecules*, 34:2015–2017, 2001.

[195] X. Guo, A.I. Isayev, and L. Guo. Crystallinity and microstructure in injection moldings of isotactic polypropylenes. Part 1: A new approach to modelling and model parameters. *Polymer Engineering and Science*, 39:2096–2114, 1999.

[196] A.K. Doufas, I.S. Dairanieh, and A.J. McHugh. A continuum model for flow-induced crystallization of polymer melts. *Journal of Rheology*, 43:85–109, 1999.

[197] J.P. Parker and P.H. Lindenmeyer. On the crystal structure of Nylon 6. *Journal of Applied Polymer Science*, 21:821–837, 1977.

[198] J. Gianchandani, J.E. Spruiell, and E.S. Clark. Polymorphism and orientation development in melt spinning, drawing, and annealing of Nylon-6 filaments. *Journal of Applied Polymer Science*, 27:3527–3551, 1982.

[199] N.S. Murthy, R.G. Bray, S.T. Correale, and R.A.F. Moore. Drawing and annealing of Nylon-6 fibres: studies of crystal growth, orientation of amorphous and crystalline domains and their influence on properties. *Polymer*, 36:3863–3873, 1995.

[200] S.M. Aharoni. *n-Nylons; Their synthesis, structure and properties*. Wiley and Sons, 1997.

[201] I. Kolesov, D. Mileva, and R. Androsch. Mechanical behavior and optical transparency of polyamide 6 of different morphology formed by variation of the pathway of crystallization. *Polymer Bulletin*, 71:581–593, 2014.

[202] H. Arimoto, M. Ishibashi, M. Hirai, and Y. Chatani. Crystal structure of the γ for of nylon 6. *Journal of Polymer Science, Part A: Chemistry*, 3:317–326, 1965.

[203] L. Penel-Pierron, C. Depecker, R. Séguéla, and J.-M. Lefebvre. Structural and mechanical behavior of Nylon 6 films part I. Identification and stability of the crystalline phases. *Journal of Polymer Science, Part B: Polymer Physics*, 39:484–495, 2001.

[204] N.S. Murthy, S.M. Aharoni, and A.B. Szollosi. Stability of the γ form and the development of the α form in Nylon 6. *Journal of Polymer Science, Part B: Polymer Physics*, 23:2549–2565, 1985.

[205] R.T. Tol, V.B.F. Mathot, H. Reynaers, B. Goderis, and G. Groeninckx. Confined crystallization phenomena in immiscible polymer blends with dispersed micro-and nanometer sized PA6 droplets part 4: polymophous structure and (meta)-stability of PA6 crystals formed in different temperature regions. *Polymer*, 46:2966–2977, 2005.

[206] G. Rotter and H. Ishida. FTIR separation of Nylon-6 chain confirmations: Clarification of the mesomorphous and γ-crystalline phases. *Journal of Polymer Science, Part B: Polymer Physics*, 30:489–495, 1992.

[207] N.S. Murthy. Metastable crystalline phases in Nylon 6. *Polymer Communications*, 32:301–305, 1991.

[208] V. Brucato, G. Crippa, S. Piccarolo, and G. Titomanlio. Crystallization of polymer melts under fast cooling. I: Nucleated polyamide 6. *Polymer Engineering and Science*, 31:1411–1416, 1991.

[209] G.C. Alfonso and A. Ziabicki. Memory effects in isothermal crystallization II. Isotactic polypropylene. *Colloid and Polymer Science*, 273:317–323, 1995.

[210] J. Kawabata, G. Matsuba, K. Nishida, R. Inoue, and T. Kanaya. Melt memory effects on recrystallization of polyamide 6 revealed by depolarized light scattering and small-angle X-ray scattering. *Journal of Applied Polymer Science*, 122:1913–1920, 2011.

[211] B. Fillon, A. Thierry, J.C. Wittman, and B. Lotz. Self-nucleation and recrystallization of polymers. Isotactic polypropylene, β phase: $\beta - \alpha$ conversion and $\beta - \alpha$ growth transitions. *Journal of Polymer Science, Part B: Polymer Physics*, 31:1407–1424, 1993.

[212] D. Cavallo, L. Gardella, G. Portale, A. Müller, and G.C. Alfonso. Self-nucleation of isotactic poly(1-butene) in the trigonal modification. *Polymer*, 55:137–142, 2014.

[213] A. Ziabicki and G.C. Alfonso. Memory effects in isothermal crystallization I. Theory. *Colloid and Polymer Science*, 272:1027–1042, 1994.

[214] N. Avramova and S. Fakirov. Cumulative erasing effect in the melt memory of Nylon 6. *Journal of Polymer Science, Part B: Polymer Physics*, 24:761–768, 1986.

[215] I. Chocinski-Arnault, V. Gaudefroy, J.L. Gacougnolle, and A. Riviere. Memory effect and crystalline structure in polyamide 11. *Journal of Macromolecular Science*, 41:777–785, 2002.

[216] Y.P. Khanna and A.C. Reimschuessel. Memory effects in polymers. I. Orientational memory in the molten state; its relationship to polymer structure and influence on recrystallization rate and morphology. *Journal of Applied Polymer Science*, 35:2259–2268, 1988.

[217] Y.P. Khanna, A.C. Reimschuessel, A. Banerjie, and C. Altman. Memory effects in polymers. II. Processing history vs. crystallization rate of Nylon 6 - Observation of phenomenon and product behavior. *Polymer Engineering and Science*, 28:1600–1606, 1988.

[218] Y.P. Khanna, R. Kumar, and A.C. Reimschuessel. Memory effects in Polymers. III. Processing history vs. crystallization rate of Nylon 6 - Comments on the origin of memory effect. *Polymer Engineering and Science*, 28:1607–1611, 1988.

[219] Y.P. Khanna, R. Kumar, and A.C. Reimschuessel. Memory effects in Polymers. IV. Processing history vs. crystallization rate - Effect of polymer structure. *Polymer Engineering and Science*, 28:1612–1615, 1988.

[220] S.M. Aharoni. *n-Nylons; Their synthesis, structure and properties*, chapter 2, pages 284–296. Wiley and Sons, 1997.

[221] T.D. Fornes and D.R. Paul. Crystallization behavior of nylon 6 nanocomposites. *Polymer*, 44:3945–3961, 2003.

[222] V. Janssens. *RheoDSC - Development and validation of a combined rheometric and calorimetric measurment technique*. PhD thesis, Katholieke Universiteit Leuven, 2010.

[223] N. Vasenthan. "Orientation induced memory effect" in polyamides and the relationship to hydrogen bonding. *Journal of Applied Polymer Science*, 90:772–775, 2003.

[224] N.S. Murthy, S.A. Curran, S.M. Aharoni, and H. Minor. Premelting crystalline relaxation and phase transitions in Nylon 6 and 6,6. *Macromolecules*, 24:3215–3220, 1991.

[225] G.M. Kim, G.H. Michler, F. Ania, and F.J. Balta Calleja. Temperature dependence of polymorphism in electrospun nanofibres of PA6 and PA6/clay nanocomposite. *Polymer*, 48:4814–4823, 2007.

[226] Y. Zhang, Y. Zhang, S. Liu, A. Huang, Z. Chi, J. Xu, and J. Economy. Phase stability and melting behavior of the α and γ phases of Nylon 6. *Journal of Applied Polymer Science*, 120:1885–1897, 2011.

[227] R. Androsch, M. Stolp, and H.-J. Radusch. Crystallization of amorphous polyamides from the glassy state. *Acta Rheologica*, 47:99–104, 1996.

[228] M. Rothe and W. Dunkel. Synthesis of monodisperse oligomers of ϵ-aminocaproic acid up to a degree of polymerization of 25 by the Merrifield method (1). *Journal of Polymer Science, Part B: Polymer Letters*, 5:589–593, 1967.

[229] T. Arakawa and F. Nagatoshi. Melting of paracrystals. *Journal of Polymer Science, Part B: Polymer Letters*, 8:41–45, 1970.

[230] J.H. Magill. Melting behaviour and spherulitic crystallization of polycaproamide (Nylon 6). *Polymer*, 3:43–51, 1962.

[231] B. Wunderlich. *Macromolecular Physics, Vol. 3, Crystal Melting*. Academic Press, New York, 1980.

[232] R. Brill. Über das verhalten vond polyamiden beim erhitzen. *Journal für praktische Chemie*, 61:49–64, 1942.

[233] K. Miyasaka and K. Makishima. Transition of Nylon 6 γ-phase crystals by stretching in the chain direction. *Journal of Polymer Science, Part A-1: Polymer Chemistry*, 5:3017–3027, 1967.

[234] K-H. Su, J-H. Lin, and C-C. Lin. Influence of reprocessing on the mechanical properties and structure of polyamide 6. *Journal of Materials Processing Technology*, 192-193:532–538, 2007.

[235] D.J. Skrovanek, S.E. Howe, P.C. Painter, and M.M. Coleman. Hydrogen bonding in polymers: Infrared temperature studies of an amorphous polyamide. *Macromolecules*, 18:1676–1683, 1985.

[236] H.K. Reimschuessel. Relationships on the effects of water on glass transition temperature and Young's modulus of Nylon 6. *Journal of Polymer Science, Part A: Polymer Chemistry*, 16:1229–1236, 1978.

[237] N.S. Murthy, M. Stamm, J.P. Sibilia, and S. Krimm. Structural changes accompanying hydration in Nylon 6. *Macromolecules*, 22:1261–1267, 1989.

[238] D. Baeten, V.B.F. Mathot, T.F.J. Pijpers, O. Verkinderen, G. Portale, P. van Puyvelde, and B. Goderis. Simultaneous synchrotron WAXD and fast scanning (chip) calorimetry: On the (isothermal) crystallization of HDPE and PA11 at high supercoolings and cooling rates up to 200 °C/s. *Macromolecular Rapid Communications*, -:–, 2015.

[239] P.C. Roozemond, M. van Drongelen, Z. Ma, M.A. Hulsen, and G.W.M. Peters. Modeling flow-induced crystallization in isotactic polypropylene at high shear rates. *Journal of Rheology*, 59:613–642, 2015.

Samenvatting

Polymeren producten worden massaal gebruikt vanwege hun relatief hoge kwaliteit tegen een lage prijs. Bij het vervaardigen van deze producten wordt meestal het materiaal eerst gesmolten om vervolgens in de gewenste vorm te worden gebracht en afgekoeld. Een groot deel van de hiervoor gebruikte kunststoffen bestaat uit semi-kristallijne polymeren, zoals polyetheen (PE), polypropeen (PP) en polyamide (PA), welke zijn opgebouwd uit kleine amorfe (zonder ordening) en kristallijne (geordende) domeinen. Het aantal, de grootte, het type en de isotropie van deze kristallen zijn grotendeels afhankelijk van de condities tijdens het vormproces. Tegelijkertijd wordt hierdoor een groot deel van de uiteindelijke mechanische en optische eigenschappen van het product bepaald. De samenhang tussen het verwerkingsproces, de microstructuur en de resulterende eigenschappen moet worden begrepen om zodoende het productieproces zodanig te kunnen aanpassen dat de gewenste eindeigenschappen worden verkregen. Dit proefschrift richt zich op het meten, begrijpen, modelleren en kunnen voorspellen van de invloed van industriële procescondities op structuurontwikkeling in verschillende polyolefines en polyamide-6. Om de invloed van hoge koelsnelheden, druk en stromingsvelden te onderzoeken, zijn verschillende geavanceerde meetmethodes gebruikt. Hiertoe behoren ook enkele unieke combinaties van meetmethodes die speciaal gerealiseerd zijn voor dit werk.

Fast scanning calorimetry (FSC) is een recent ontwikkelde techniek die wordt gebruikt om de warmtekarakteristiek ten gevolge van kristallisatie, smelten en reorganisatie van polymeren te bestuderen onder hoge afkoel- en opwarmsnelheden. Voor de eerste maal is aangetoond dat een combinatie van FSC-sensoren en microfocus röntgenanalyse gebruikt kan worden om de kristallijne structuur van proefstukken op een FSC chip vast te stellen.

Lineair lagedichtheids polyetheen (LLDPE) wordt veelvuldig gebruikt voor de productie van polymeren film. Door de moleculaire opbouw vindt kristallisatie plaats in meerdere stappen: een primair proces, de groei van sferulieten, en een tweevoudig secundair proces, namelijk invoeging van lamellen gevolgd door bundeling op lage temperatuur van ketens van een deel van de resterende amorfe fase. Voor één metalloceen LLDPE is een volledige karakterisering van het kristallisatiegedrag uitgevoerd. Primaire kristallisatie is beschreven met een model voor temperatuurafhankelijke kiemformatie en groei, gemeten door middel van small-angle light scattering (SALS). De beschrijving van beide secundaire processen is, met behulp van een convolutie-integraal, gekoppeld aan dit primaire kristallisatiemodel. Het volledige

kristallisatiegedrag tijdens koelen, gemeten met koelsnelheden tussen 0.07-2000 °C/s met behulp van differential scanning calorimetry (DSC) en FSC, kan op deze manier nauwkeurig worden beschreven. Dilatometrie metingen tonen aan dat een combinatie van stroming en druk primaire kristallisatie versterkt en secundaire kristallisatie onderdrukt. Tot slot is een bestaand fenomenologisch model gebruikt om, met succes, stromingsgeïnduceerde primaire kristallisatie te kunnen beschrijven.

Heterogene polypropyleen impact co-polymeren zijn samengesteld uit een semi-kristallijne matrix en amorfe, rubberachtige domeinen. Door hun uitzonderlijk gunstige balans tussen soortelijk gewicht, stijfheid en slagvastheid, wordt dit type materiaal in toenemende mate gebruikt in de autoindustrie. De relatie tussen verwerking, structuur en eindeigenschappen is onderzocht voor drie verschillende materiaalsamenstellingen. Met behulp van dilatometrie zijn experimenten uitgevoerd bij meerdere koelsnelheden en verschillende stromingscondities. Met transmissie-electronenmicroscopie (TEM) is aangetoond dat structuurvorming plaatsvindt binnen drie regimes. Als functie van de sterkte van het stromingsveld is er allereerst sprake van het ontbreken van oriëntatie, vervolgens van stromingsgeïnduceerde kristallisatie en oriëntatie van de matrix en, in de laatste fase, vind er bovendien oriëntatie van het vulmateriaal plaats. Tevens zijn deze regimes te onderscheiden in kristallisatiekinetiek en wanneer deze proefstukken mechanisch worden belast in een trekproef.

Structuurontwikkeling tijdens het filmblaasproces is onderzocht met behulp van in-situ röntgendiffractie door een complete filmblaasopstelling voor een synchrotron röntgenbundel te plaatsen. De kristallisatiekinetiek en de ontwikkeling van kristal-oriëntatie zijn onderzocht voor drie verschillende lagedichtheids polyethenen (LDPE′s) als functie van afstand en tijd vanaf de blaaskop. De invloed van combinaties van hoge en lage verstrek- en opblaasratio′s zijn onderzocht. Zoals verwacht toont het materiaal met het hoogste molgewicht ook de hoogste oriëntatie in de verstrekrichting, terwijl het materiaal met gemiddeld molgewicht en een relatief lage fractie van de hoogmoleculaire staart het snelste kristalliseert. Door de complexiteit van het filmblaasproces kan geen duidelijke trend worden waargenomen tussen de moleculaire eigenschappen van de verschillende materialen en het verloop van de verschillende kristalrichtingen. De vrieslijn, een kenmerkende afstand voor de overgang tussen polymeren smelt en vaste stof, wordt onafhankelijk van het materiaal en de gebruikte condities waargenomen op 20% kristalliniteit, ongeveer halverwege de uiteindelijke waarde. Tegelijkertijd bereikt de c-as oriëntatie van de kristallen wel een maximum op de vrieslijn. De toegepaste meetmethode is goed bruikbaar om het complexe filmblaasproces beter te begrijpen. Tevens kunnen de data uitstekend gebruikt worden voor validatie of uitbreiding van huidige en nieuwe numerieke modellen.

Onverwerkt polyamide-6 (PA-6) vertoont een opmerkelijk en irreversibel verschijnsel; voor een gegeven koelsnelheid versnelt het kristallisatiegedrag naarmate de polymeren smelt meer wordt gedeformeerd. Dit 'geheugen-effect' is stap voor stap onderzocht door gebruik

te maken van röntgendiffractie. Hiervoor zijn unieke proefstukken gebruikt, welke zijn vervaardigd door onverwerkt granulaat net onder de gemiddelde smelttemperatuur samen te voegen tot ronde plaatjes. Uit de meetdata blijkt dat enkel de totale deformatie invloed heeft op het kristallisatiegedrag. Bovendien is voor het niet gedeformeerde materiaal een tot op heden onbekend kristallisatiegedrag waargenomen. Op basis van de metingen worden de tot op heden in de literatuur voorgestelde oorzaken van het geheugeneffect besproken.

Dankwoord

Dit proefschrift was er nooit gekomen zonder de unieke samenwerking en gezelligheid binnen de Polymer Technology groep. Experimenteel onderzoek is teamwork, nu ik de kans krijg wil ik dan ook graag een aantal mensen bedanken.

Als eerste natuurlijk Gerrit. Regelmatig bestond een groot deel van onze meetings uit het bestuderen van de aanbouw van Flux of het online opzoeken van allerlei steden of (voor mij onbekende) gezegdes. Juist deze afwisseling met een kritische discussie over de resultaten en het plan van aanpak ben ik enorm gaan waarderen. Bedankt voor het gestelde vertrouwen om mij geregeld mijn eigen plan te laten trekken. Leon, toen ik in mijn derde studiejaar voor het eerst het polymerenlab binnenwandelde, wist ik door de gezellig sfeer meteen dat ik mijn plek had gevonden. Ondanks dat ik destijds je lab heb weten te besmeuren met zwarte bitumen, ben jij nog altijd 'blij met kunststof'. Tim, als mijn afstudeermentor en latere collega ben jij degene geweest die me een groot deel van 'het vak' hebt bijgebracht. Niet te vergeten de belangrijke lessen over het meenemen van voldoende Autodrop en muziek tijdens een lange rit naar Frankrijk.

Het grootste deel van mijn promotie heb ik toch wel doorgebracht in Kantoor-café 4.22. Zonder alle namen te noemen wil ik dan ook alle (oud-)kantoorgenoten en stamgasten bedanken voor de samenwerking, discussies, leuke humor, slechte humor, fruit- of taartmomentjes en het gezelschap tijdens allerlei congressen en reisjes. Hierbij zijn ook de collega's van de Scheikundige 'overkant' inbegrepen, en laten we eerlijk zijn, zonder jullie had ik RPK-A natuurlijk nooit gehaald.

A special thanks to the people from Genova. Dario, for radiating your endless passion on crystallizing polymers, which brought me many insights and got me involved in a bunch of interesting projects. Giancarlo, thanks for your kindness and consideration, and for teaching me how to properly cook pasta during my first visit to the ESRF canteen. Lili, I sincerely enjoyed our collaboration during your visits to the office. Hopefully, we can soon enjoy some real Chinese 'not-too-much-spicy-food' in suburban Shanghai.

The many trips to Grenoble would not have provided GB's of data without the support of the DUBBLE staff. Next time, I will try to bring a setup that fits through the doors normally.

De heren van IME, bedankt voor de fijne samenwerking omtrend de Pirouette. Ik hoop jullie over een aantal jaar terug te vinden in opnieuw een groter pand gevuld met zoemende electrospinners.
Door het feit dat standaard meetopstellingen vaak maar saai zijn, waren er soms vele technische aanpassingen nodig om tot een leuk resultaat te komen. Hiertoe ben ik dank verschuldigd aan het uitstekende timmermansoog van de heren in de werkplaats, Lucien en Sjef in het bijzonder.
Verder wil ik ook mijn vrienden in Eindhoven en daarbuiten noemen die zich wat minder bezighouden met polymeren, wat afleiding en gezelligheid buiten het werk is tenslotte ook belangrijk. Hierbij horen mijn Zeeuwsche kameraden Alex, Merijn, Peter en Eddy. Al vele jaren weten we elkaar te vinden voor allerlei festivals, feestjes en reizen, ik hoop dat we dit nog lang mogen voortzetten.
Sportief gezien heb ik erg veel lol gehad met het gelegenheidsteam 'de Polymeerfietsers'. Als we nu voor de verandering eens wat beter kop-over-kop gaan rijden, zullen er nog vele Strava segmenten sneuvelen!
Stefan & Nicole, Alwin & Laurette, het doet altijd goed jullie te zien. Als oom zal ik mijn best doen om de snelle groei van jullie kleintjes bij te houden. Wat onze broederlijke interesse in het onderzoek betreft, goed voorbeeld doet volgen zullen we maar zeggen! Annouk & Siebe, al vanaf mijn eerste week in Eindhoven ben ik altijd welkom voor een 'hapje eten' of een 'lekker biertje'. Hoewel ik de laatste jaren misschien wat minder over de vloer kom, wordt dit nog altijd enorm gewaardeerd. Pap & Mam, welke plannen voor reizen of werk ik ook heb, op jullie steun en interesse kan ik altijd rekenen. Ondanks dat dit proefschrift weinig te maken heeft met mijn vroegere plan om timmerman of meubelmaker te worden, hoop ik dat jullie trots kunnen zijn. En als laatste natuurlijk Martine, op naar ons eerstvolgende avontuur in Denemarken!

Martin

Eindhoven, April 2015

Resume

Martin van Drongelen was born in Axel, Zeeuws-Vlaanderen, the Netherlands, on September 29th, 1987. After finishing pre-university education at the Zeldenrust-Steelant College in Terneuzen in 2005, he studied Mechanical Engineering at Eindhoven University of Technology. His master thesis was completed in March 2011 in the Polymer Technology group of Prof. H.E.H. Meijer, under supervision of Prof. G.W.M. Peters on the development and experimental validation of a multi-phase crystallization model for polypropylene. As a part of his master track he performed an international internship at McGill University, Montreal, Canada, under supervision of Prof. M.R. Kamal.

In April 2011, he took the opportunity to pursue a PhD-degree under the guidance of Prof. G.W.M. Peters. The results are presented in this thesis.

During his PhD the author succesfully completed the postgraduate course Register Polymer Sciene of the National Dutch Research School PTN (Polymeer Technologie Nederland) and was awarded the title of Registered Polymer Scientist in October 2013.

Martin recently joined a post-doctoral research project in the group of Prof. O. Hassager at the Danish Technical University (DTU) in Copenhagen.

List of publications

This thesis has resulted in the following publications:

- M. van Drongelen, A.M.J.T. Meijer-Vissers, D. Cavallo, G. Portale, G. Vanden Poel and R. Androsch. Microfocus wide-angle X-ray scattering of polymers crystallized in a fast scanning chip calorimeter, *Thermochimica Acta*, 563:33-37, 2013.

- M. van Drongelen, P.C. Roozemond, E.M. Troisi, A.K. Doufas and G.W.M. Peters. Characterization of the primary and secondary crystallization kinetics of a linear low-density polyethylene in quiescent- and flow conditions, *submitted*

- M. van Drongelen, M. Gahleitner, A.B. Spoelstra, L.E. Govaert and G.W.M. Peters. Flow-induced solidification of high-impact polypropylene copolymer compositions: Morphological and mechanical effects, *Journal of Applied Polymer Science*, 132:42040, 2015

- M. van Drongelen, D. Cavallo, L. Balzano, G. Portale, I. Vittorias, W. Bras, G.C. Alfonso and G.W.M. Peters. Structure development of low-density polyethylenes during film blowing: A real-time wide-angle X-ray diffraction study, *Macromolecular Materials & Engineering*, 299:1494-1512, 2014

- M. van Drongelen and G.W.M. Peters. Kinetics of the deformation induced memory effect in polyamide-6, *in preparation*

Additionally, the author contributed to a number of publications outside this thesis:

- L. Zhang, M. van Drongelen, G.C. Alfonso and G.W.M. Peters. The effect of pressure pulses on isotactic polypropylene crystallization, *submitted*

- J.E.K. Schawe, P.A. Vermeulen and M. van Drongelen. A new crystallization process in polypropylene highly filled with calcium carbonate, *Colloid and Polymer Science, accepted or in press*

- E.M. Troisi, G. Portale, Z. Ma, M. van Drongelen, D. Hermida Merino and G.W.M. Peters. Unusual melting behavior in flow induced crystallization of LLDPE: the effect of pressure, *Macromolecules*, 48:2551-2560, 2015

- P.C. Roozemond, M. van Drongelen, Z. Ma, M.A. Hulsen and G.W.M. Peters. Modeling flow-induced crystallization in isotactic polypropylene at high shear rates, *Journal of Rheology*, 59:613-642, 2015

- B.J. Luijsterburg, G.W. de Kort, M. van Drongelen, L.E. Govaert and J.G.P. Goossens. Fast cooling of (non)-nucleated virgin and recycled poly(propylenes): effect of processing conditions on structural and mechanical properties, *Thermochimica Acta*, 603:94-102, 2015

- P.C. Roozemond, M. van Drongelen, Z. Ma, A.B. Spoelstra, D. Hermida-Merino and G.W.M. Peters. Self-regulation in flow-induced structure formation of polypropylene, *Macromolecular Rapid Communications*, 36:385-390, 2015

- P.C. Roozemond, M. van Drongelen, L. Verbeelen, P.C.J. van Puyvelde and G.W.M. Peters. Flow-induced crystallization studied in the RheoDSC device: quantifying the importance of edge effect, *Rheologica Acta*, 54:1-8, 2014

- I. Stolte, D. Cavallo, G.C. Alfonso, G. Portale, M. van Drongelen and R. Androsch. Form I' crystal formation in random butene-1/propylene copolymers as revealed by real-time X-ray scattering using synchrotron radiation and fast scanning chip calorimetry, *European Polymer Journal*, 60:22-32, 2014

- G. Portale, D. Cavallo, G.C. Alfonso, D. Hermida-Merino, L. Balzano, M. van Drongelen, G.W.M. Peters, J.G.P. Goossens and W. Bras. Crystallization studies under processing-relevant conditions at the SAXS/WAXS DUBBLE beamline at the ESRF, *Journal of Applied Crystallography*, 46:1681-1689, 2013

- M. van Drongelen, T.B. van Erp and G.W.M. Peters. Quantification of non-isothermal, multi-phase crystallization of isotactic polypropylene: the influence of cooling rate and pressure, *Polymer*, 53:4758-4769, 2012.

- C.D. Descour, A.M.J.T. Meijer-Vissers, T. Macko, M. Parkinson, D. Cavallo, M. van Drongelen, G. Hubner, J.G.P. Goossens and R. Duchateau. Random and block copolymers based on 4-methyl-1-pentene and 1-pentene, *Polymer*, 53:3096-3106, 2012.

Furthermore, the following publications are in preparation, and soon to be submitted:

- E.M. Troisi, M. van Drongelen, H.J.M. Caelers and G.W.M. Peters. "Filmblowing of linear low-density polyethylene with in-situ SAXS."

- M. van Drongelen, P.C. Roozemond and G.W.M. Peters. Advances in Polymer Science Vol. "Polymer Crystallization: From chain microstructure to processing", Chapter: "Non-isothermal crystallization of semi-crystalline polymers: The influence of cooling rate and pressure."

- P.C. Roozemond, M. van Drongelen and G.W.M. Peters. Advances in Polymer Science Vol. "Polymer Crystallization: From chain microstructure to processing", Chapter: "Modeling flow-induced crystallization."